UNIVERSITY OF OKLAHOMA

GRADUATE COLLEGE

BIOMATERIAL AND COMPUTATIONAL BASED STRATEGIES FOR THE IN VITRO DEVELOPMENT OF BONE TISSUE AND TUMOR ENGINEERED CONSTRUCTS

A DISSERTATION

SUBMITTED TO THE GRADUATE FACULTY

in partial fulfillment of the requirements for the

Degree of

DOCTOR OF PHILOSOPHY

By

CORTES WILLIAMS III
Norman, Oklahoma
2017

BIOMATERIAL AND COMPUTATIONAL BASED STRATEGIES FOR THE IN VITRO DEVELOPMENT OF BONE TISSUE AND TUMOR ENGINEERED CONSTRUCTS

A DISSERTATION APPROVED FOR THE STEPHENSON SCHOOL OF BIOMEDICAL ENGINEERING

BY

Dr. Vassilios Sikavitsas, Chair

Dr. Susan Walden

Dr. Rong Gan

Dr. Roger Harrison

Dr. Dimitrios Papavassiliou

DEDICATION

to

My wife,

Alisha Janii Williams

and my daughter,

Valerie Lynn Williams

Acknowledgements

I would first like to express my gratitude to my advisor, Dr. Vassilios Sikavitsas, for all of his help and guidance, not only in the lab, but in life. I would not have made it this far without him. Another special thanks to Dr. Susan Walden, who's timely advice kept me sane throughout graduate school. I would also like to thank Dr. Rong Gan, Dr. Roger Harrison, and Dr. Dimitrios Papavassiliou for having patience with me both as a student and as a researcher.

Furthermore, I would like to thank the staff and professors of both the SBME and CBME departments. In particular, thanks to Dr. Edgar O'Rear, Dr. Matthias Nollert, and Dr. Robert Shambaugh for pushing me to be a better student, and PJ Meek, Terri Colliver, Wanda Gress, Madena McGinnis, and Donna King for all of their assistance. A special thanks to Lisa Morales for always being available to talk and motivating me to keep pushing forward.

I would also like to thank the other graduate students for their help and friendship: Zach Mussett, Aaron Simmons, Patrick McKernan, Needa Virani, Chase Brown, James Buerck, Julien Arrizabalaga, Jin Liu, Ghani Muhammad, Nathan Richbourg, Montana Minnis, and Chelsea Coffey. Additional thanks to Dr. Brandon Engebretson, Dr. Samuel VanGordon, and Dr. Roman Voronov

for training me in the lab back when I was an undergraduate.

No words can properly express my gratitude to my parents, Cortes and Deloris Williams, and my sister, Courtney Williams, for all of their love and support. Their unwavering, and sometimes irrational, confidence in me helped pull me through the difficult times. Most importantly, I would like to thank my wife, Alisha, for basically everything. She supported me through all of the classes, the late night lab experiments, and the endless writing. I definitely would not have made it this far without her. Lastly, thank you to my beautiful daughter, Valerie, for giving all of this meaning, and for showing me what I really want from life.

Table of Contents

List of Tables

List of Figures

Abstract

Every year in the United States, more than 500,000 bone graft surgeries are required. In most cases, bone will regenerate after fracture with minimal complications; however, when there is a critical-sized defect or fracture healing is impaired, bone grafts must be used in order to regain proper bone function. Additionally, bone diseases such as osteoporosis, infection, skeletal defects, and bone cancer may also cause a need for bone grafts. Bone tissue engineering offers a possible solution to the supply problem plaguing current bone graft therapies by providing a near limitless supply of bone for reimplantation. Furthermore, because tissue engineered bone would be made using the patient's own cells, risk of immune rejection would be eliminated. Unfortunately, current bone culture techniques suffer from one or more of the following: 1) inadequate cell adhesion to the underlying scaffold; 2) poor or lack of proper quality control and repeatability; or 3) requiring destructive methods to judge construct quality.

During the last decade, the number and effectiveness of *in vitro* cancer models has increased dramatically. Utilizing a variety of techniques for 3D culture, researchers have created models that more closely resemble and predict *in vivo* tumor drug responses; however, the same hindrances faced in bone

tissue engineering occur with some *in vitro* cancer models. In particular, these *in vitro* models consistently exhibit poor cell proliferation and distribution, which severely limits their predictive capabilities. The number one hurdle that must be overcome is the poor adhesion that cancer cells have to non hydrogel scaffolds, which severely limits the development of tumor models that contain fully developed tissue.

These aforementioned issues highlight three major questions that will be investigated in this manuscript: 1) How can we improve both mesenchymal stem cell and cancer cell adherence to the scaffolds? 2) In terms of flow-induced stresses, what is the viability of 3D printing for manufacturing repeatable scaffold architectures? 3) Do the shear stresses within a bone tissue engineered construct change over the culture period? These questions will be answered using a combination of both biomimetic scaffold functionalization and computational fluid dynamic simulations. For the former, a physical entrapment technique which introduces free amine groups to the surface of the scaffolds was developed, allowing for the subsequent attachment of RGD and n-cadherin to aid in mesenchymal stem cell and tumor cell attachment, respectively. For the latter, constructs were imaged using micro-computed tomography, reconstructed, and imported into the computational fluid dynamic program FLUENT (ANSYS, Inc), allowing for the evaluation of the flow profiles and shear stress distributions therein. The following chapters of this manuscript will focus on each of this questions in succession, outlining the motivations and methods used to tackle each problem, and the results of our findings.

Chapter 1

Background & Significance

Tissue engineering is a developing field that links biologics with engineering to promote tissue regeneration. Key components for successful tissue engineering are: an appropriate cell or stem cell source typically derived from the patient via a cell biopsy; a scaffold that is biocompatible and bioabsorbable; and mechanical or chemical stimuli that differentiate the cells on the construct into the accurate cell lineage. When implanted in a patient, the tissue construct is expected to influence extracellular matrix organization and construct degradation, limit any immune reactions, all while the native tissue remodels and regenerates. Tissue engineering has become a very popular method when combined with bioreactors for treating disorders of the musculoskeletal system.

Current Strategies

Currently there are four main types of bone grafts: autografts, allografts, xenografts, and bone cement. Autografts, where healthy tissue is taken from

the patients own body, are overall the best type of bone grafts, due to the fact immune rejection is not a serious factor. In this type of procedure, healthy tissue is taken from another site on the patients body and is then transplanted to the desired area. However, these grafts suffer from a limited supply and also donor site morbidity, pain in the harvesting site. In addition, these grafts may fail due to many cells not surviving the transplantation process[17, 19].

Allografts, tissue taken from a donor of the same species, are another frequently used bone replacement. They have become more common in the past decade through the introduction of immunosuppressant drugs that help ease the immune response from foreign tissue entering the body. Even still, they may cause immune rejection and have limited osteoinductive abilities when compared to autologous grafts [17].

Another graft source are xenografts, which are grafts taken from animals. The common animals used for transplants are pigs, sheep, and goats. Unfortunately they carry with them a high rate of infection and host rejection. Due to this, xenogeneic grafts are not highly desired [19].

Synthetic Alternatives

Because natural tissue sources are difficult to obtain, many people choose to get mechanical replacements. Table 1.1, shown below, gives an overview on the differences between bone grafts and common bone graft substitutes. One of the common grafts shown in the table, hydroxyapatite, is a synthetic bone substitute that has been frequently used. It is a brittle material that slowly undergoes bone resorption. Due to this, it is more often than not combined with other materials to increase the speed of resorption. Another common

Osteoconductive Scaffolds					
Type	Graft	Osteoconduction	Osteoinduction	Osteogenesis	Advantages
Bone	Autograft	+++	++	++	Gold Standard
	Allograft	+++	+	0	Availabile in many forms
Biomaterials	DBM	+	++	0	Supplies osteoinductive BMPs, bone graft extender
	Collagen	++	0	0	Good as delivery system
Ceramics	TCP, hydroxyapatite	+	0	0	Biocompatible
	CPC	+	0	0	Some initial structural support
Composite	β-TCP/ BMA cement composite	+++	++	++	Ample supply
	BMP/ synthetic composite	-	+++	-	Potentially limitless supply

Table 1.1: Comparison of common scaffolds. Score: 0 (none) to +++ (excellent). A (-) indicates information that is either unknown or not provided. DBM: demineralized bone matrix, TCP: tricalcium phosphate, CPC: calcium phosphate cement, BMA: bone marrow aspirate, BMP: bone morphogenetic protein. Table is adapted from the following publication [19].

material is ceramics. They are usually made from tricalcium phosphate and have been shown to have osteogenic capabilities when they are attached to healthy bone [31, 47]. Compared to hydroxyapatite, they have faster bone resorption, but must also be surgically removed as the new bone grows [19].

When the whole bone is not damaged, bone cements are used. Polymethyl methacrylate, PMMA, is a popular bone cement that works by acting as an anchor, connecting bone to bone or bone to joint, and absorbing force in the same fashion natural bone would. The use of bone cement is very popular due to its widespread availability and effectiveness. The negatives of bone cement are that it is non-biodegradable and permanent. Also PMMA bone cement

works by exothermic free-radical polymerization. The heat it gives off during this reaction is harmful to the neighboring tissue at the implantation site and local cells and tissue are often damaged. Furthermore it has been shown to bind poorly to bone surfaces [34].

1.1 Bone Tissue Engineering

Every year in the United States, there are more than 500,000 bone graft surgeries, with the most common needed for regenerating bone in fractural healing [17, 19]. In most cases, bone will regenerate after fracture with minimal complications; however, when there is a critical-sized defect or fracture healing is impaired, bone grafts must be used to regain proper bone function. Furthermore, bone diseases such as osteoporosis, infection, skeletal defects, and bone cancer may also cause a need for bone grafts. Also of great importance, are the bone problems facing astronauts during space exploration. Due to the biology of bone, astronauts lose bone mass while they are in zero gravity. This is caused by a decrease in movement and mechanical force, and in some cases correlated to bone mineral density loss of up to 40% [73]. Given these problems, it is ideal that we look for new bone healing methods or bone replacements.

Bone tissue engineering is a possible solution to the problems plaguing the current bone graft therapies. Because tissue engineered bone would be made of the patient's own cells, immune rejection would be eliminated as well as low availability. For this to work, four components are needed for tissue growth: cells that can be differentiated into bone cells, osteoconductive scaffolds for acting as a matrix while the tissue grows, growth factors and other chemical

stimulation, and mechanical stimulation to encourage osteogenic differentiation. Mechanical stimulation is implemented through the use of bioreactors.

1.1.1 Bone Biology

Bone is a specialized connective tissue mainly used as support and structure for the vertebrate body. Its mechanical role is to not only protect the vulnerable tissues of the body, but to also serve as an anchor for the muscles in the body, so they gain leverage for movement [10]. Furthermore, the bones are used by the body to maintain a steady concentration of phosphate and calcium ions that will be used in various homeostatic processes [23]. Bone is made up of two different subcomponents: cortical and spongy bone. Cortical bone, also called compact bone, is more dense than its counterpart with a porosity of 5-30% [64]. It is made of tightly packed collagen fibrils, which together form the lamellae. These collagen fibrils are what give compact bone its strength. By weight, compact bone contains approximately 30% matrix and 70% salt deposit. The organic matrix consists of over 90% collagen fibrils and the rest is ground substance, which is formed from the non-fibrous portions of extracellular matrix. Ground substance, for the most part, does not contain collagen, but it is made up of glycosaminoglycans, glycoproteins, and proteoglycans[10]. Due to the orientation of the collagen fibers, along the direction of the force acting on the bones, the bone has a very high tensile strength compared to the other tissues in the body. The bone salts contained in compact bone are primarily calcium and phosphates. During calcification these two molecules form a crystalline salt known as hydroxyapatite. Spongy bone, or cancellous bone, is more loosely packed and has an average porosity of 30-90% [64]. Another

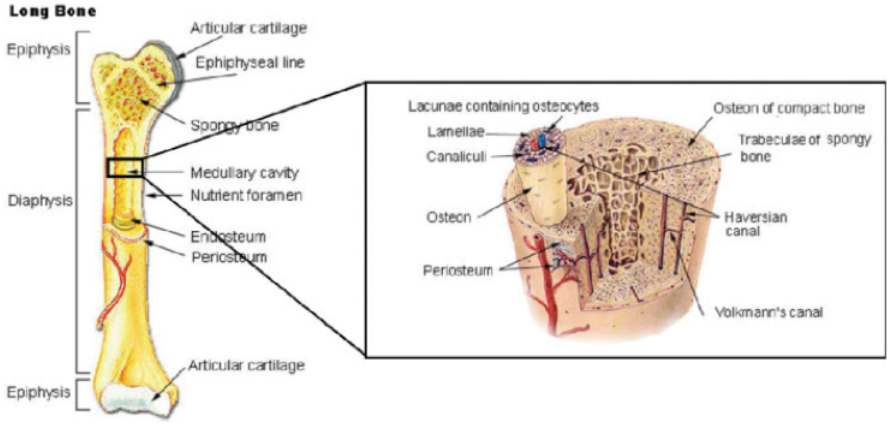

Figure 1.1: Schematic of long bone showing its anatomy and the orientation of compact and spongy bone. Figure used with permission from the following publication [10].

major difference between cortical and spongy bone is their function. Compact bone, being more rigid, provides the structural strength, while the spongy bone provides the components for metabolic maintenance.

The shape of long bone (shown in Figure 1.1) is such that it can withstand the greatest amount of force. The inner section, diaphysis, contains a higher amount of compact bone meaning that it is made of tightly packed collagen fibrils. The epiphysis, ends of the bone, is wider than the diaphysis and contains a higher amount of spongy bone [10].

1.1.2 Bone Calcification and Renewal

Knowing that we are growing bone, it is important to gain an understanding on the mechanism for bone calcification. When cells are being cultured for use in bone tissue engineering, the marker for differentiation into bone cells is calcification. The first step consists of both collagen monomers and ground substance being secreted by osteoblasts [31]. These collagen monomers form

collagen fibers that, in this early state, are called osteoids. Osteoids are similar to cartilage however the rate at which calcium precipitates in it is significantly higher [23]. During the formation of osteoid, many osteoblasts become entrapped, and are from then on known as osteoclasts. Over the next few months, calcium salts form on the collagen fibers of the osteoid, and in time they undergo substitution becoming complete hydroxyapatite crystals. The calcium salts that are not converted into hydroxyapatite stay on the fibers as amorphous salts that can easily be released into the extracellular fluid [23].

Another important feature of bone is how it is continually being renewed. There are two process involved in this: deposition and absorption. Deposition is the act of osteoblasts continually calcifying bone, and absorption is the process of osteoclasts removing bone. The process through which this occurs is still somewhat unknown. However, researchers have found that deposition occurs through the mineralization of bone matrix and also the growth of mineral crystal [10]. The differences between theories come from whether this is accomplished through the use of vesicles or specific binding by calcium. Under normal conditions, vescicle mediation or calcium binding happen at approximately the same rate so that bone is both always in a full state and continuously being remodeled. The rate at which these processes occur is proportional to the stress put on the bones. Therefore an athlete that is constantly moving will have a higher rate of bone remolding than a person who sits at a desk all day.

There are two mechanisms for bone formation: intramembranous ossification and endochondral ossification, with most of our bones following the latter pathway. In intramembranous, or direct, ossification, masses of mes-

enchymal stem cells differentiate into osteoblasts through the use of vascularization. These osteoblasts then form osteoids, and the osteoblasts that are inside become osteocytes. The bones that form by this process are the clavicle, mandible, face bones, and bones in the cranial vault [31, 10].

Bones that have a constant stress from weight or movement are formed through endochondral ossification. These bones take an intermediate step where the initial stem cells form chondrocytes before forming the bone matrix. Chondrocytes build soft tissue that serves as a scaffold for the eventual growth of bone matrix. The templates of chondrocytes, which have formed a vascular tissue called a growth plate, are vascularized. Then osteoblasts differentiate around the central area of the bone. While this is happening, the local chondrocytes turn hypertrophic and induce further vascular penetration [31, 10, 47]. After this, osteoblasts are recruited into the forming bone and began calcification.

1.1.3 Bone Cell Types and Sources

Native bone contains three cell types relevant to tissue engineering: osteoblasts, osteoclasts, and osteocytes. Another important bone cell type involved in bone tissue engineering is the osteoprogenitor cell. For tissue engineering applications, osteoprogenitor cells mainly differentiate from mesenchymal stem cells. These osteoprogenitor cells are the precursors for osteoblasts, osteocytes, and the bone lining cells; whereas the osteoclasts are formed through the fusion of mononuclear precursors, such as those from hemopoietic tissue [31].

Osteoblasts are the major cell type responsible for bone deposition, the growing of bone. Their main function is the development of mineralized tis-

sue, which contains several proteins, such as osteocalcin and osteopontin, and collagenases that aid in osteoclast activation [31, 10]. Osteocalcin is a noncollagenous protein, created solely by osteoblasts, that is involved in controlling the rate of bone formation and bone mineral maturation [10]. Since it is only secreted by osteoblasts, osteocalcin is a prime candidate for identifying if a stem cell culture is turning osteogenic, and is commonly used as a biochemical marker for bone formation [58, 71]. Osteopontin is a noncollagenous glycoprotein that is responsible for osteoclast attachment and resorption [71].

Osteocytes are formed from osteoblasts that have been entrapped in the bone matrix, and take care of the maintenance of the bone [31]. Each osteocyte resides in its own space in the bone matrix, named lacunae and canaliculi, and are interconnected through channels. These channels, also known as gap junctions, serve as the passageway through which nutrients can be exchanged with between osteocytes, blood vessels, and other places throughout the bone [66, 10].

Osteoclasts main function is the resorption of bone. On their membrane, they have both a smooth surface that serves as a connective area for attaching to the bone matrix using integrins and, as previously mentioned, the aid of matrix proteins such as osteopontin. They also have a rough surface where bone resorption takes place. Proteolytic enzymes and acids released from this rough border break down the bone by breaking down the organic matrix and bone mineral [66, 10].

Like in all tissue engineering fields, the osteoblastic cell source is a very vital part of the equation. The ideal cells for use *in vitro* will have a high proliferation rate, an ability to differentiate into the cells necessary for the tissue

to operate, and also the ability to deposit organic tissue matrix. The most popular cells that are considered for bone tissue engineering are mesenchymal stem cells (MSCs), adipose derived stem cells, osteoblastic progenitor cells, osteoblasts, and osteocytes. For the most part, osteoclasts have not been utilized since they are not required for the formation of mineralized tissue. MSCs are the most widely used cells for bone tissue engineering. MSCs have been found to have increased osteoblastic differentiation when exposed to fluid shear, and also have exhibited clear osteoinductive capabilities [15, 56, 37]. Furthermore it is widely known that MSCs have a higher proliferation rate when compared to osteoblasts and osteocytes [37].

1.1.4 Scaffolds for Bone Tissue Engineering

As with all tissue engineering fields, scaffolds are a necessity for *in vitro* applications. For bone tissue engineering, the scaffold must allow the cells to not only attach and proliferate, but must also allow for mechanical stimulation, encourage bone cell migration, act as a substrate for osteoid deposition, and deliver bioactive molecules [52]. Another aspect that is desired is biodegradability. If a tissue engineered construct is put into the body, the scaffold must degrade over time leaving only organic material that will retain natural levels of mechanical strength [7, 28, 5]. The common scaffold types used for bone growth are natural polymers (fibrin and collagen), synthetic polymers (polycarbonates, polyanhidrides, poly(ethylene oxide), polyfumarates, and polyphosphazene), metals and ceramics [39, 11]. Due to their controlled biodegradability, published mechanical properties, and widespread use in polymer and tissue engineering research, synthetic scaffolds, in par-

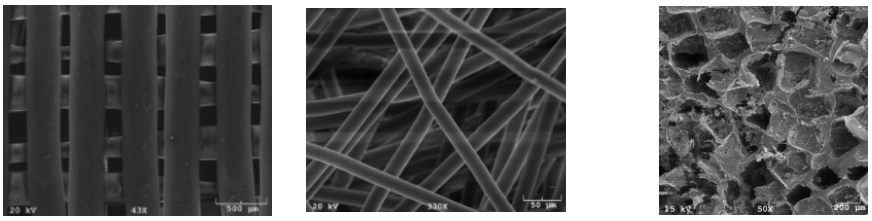

Figure 1.2: Common sythentic polymeric scaffolds used for tissue engineering. (left): 3D printed. (middle): spunbonded (right): solvent-cast porogen-leached. Images were taken using scanning electron microscopy.

ticular poly(lactic acid)(PLA), poly(glycolic acid)(PGA), and poly(lactic-co-glycolic acid)(PLGA) are the most popular candidates [39].

Currently, there are two major types of scaffolds: injectable and prefabricated [19, 30]. Injectable scaffolds are desirable due to their ability to take the shape of highly irregular bone defect sites; however, the big problem currently facing these scaffolds is their inability to generate controllable porous networks that can be infiltrated by host osteoprogenitors and vascular network. The latter means that if any cells do reside in the center of the construct, they will not be able to obtain optimal oxygen and other nutrient supplies. In addition, very carefully designed crosslinking strategies are required to avoid the release undesirable chemicals or heat that may harm the host neighboring host tissue. Prefabricated scaffolds, on the other hand, have highly controllable porosity that will allow enhanced levels of nutrient delivery throughout the construct, and also the possibility for higher mechanical strength. Common types of scaffolds include those made from rapid prototyping such as 3D printing, fiber meshes (woven and nonwoven), and porous foams (salt leached or gas foamed), each of which is shown in Figure 1.2 [12, 29, 42, 43, 30, 13, 28].

1.1.5 Cell Culture

The culture of cells for bone tissue engineering is very similar to that for other tissue engineering fields. It is necessary to have a culture media, commonly alpha-minimal essential media, dubelco's-minimal essential media, or Roswell Park Memorial Institute medium 1640, which contains the proper nutrients for cell growth. These media often include d-glucose, l-glutamine, HEPES (a buffer for maintaining physiological pH), phenol red indicator (for easily identifying pH). The differences between culture media are usually in their concentration of glucose, growth factors, and other nutrients. Another commonly used and essential part of media is fetal bovine serum (FBS), newborn calf serum (NCS), or some other similar animal blood serum. The purpose of these is to provide the cells with the proper growth factors to facilitate cell growth. It is important to note, however, that serums must always be screened to insure that they will differentiate cells properly; due to the fact protein concentrations are not consistent between batches.

When bone cells are desired, osteogenic media is used. Osteogenic media differs from regular culture media in that it contains dexamethasone, beta-glycerophosphate, and ascorbic acid. Dexamethasone is a glucocorticoid that has been found to facilitate bone differentiation and mineralization in cultures [61]. Beta-glycerophosphate and ascorbic acid roles are to provide phosphate and increase collagen fibril production, respectively [61]. Growth factors may also be added to aid in osteogenic differentiation. BMP-2 (bone morphogenetic protein), as well as BMP-7, are osteoinductive growth factors that are commonly used to enhance mesenchymal stem cell differentiation into osteoblasts. BMP-2 is an important growth factor as it is involved in the TGF

beta-signaling pathway, and aids in osteogenesis, cell growth, and differentiation [50, 17]. Once the cells are ready to be used for experiment, they must be seeded onto the scaffolds. Although the procedure may vary, static and dynamic seeding are the two most commonly used seeding methods. Static seeding consists of injecting cells on to scaffolds that are sitting in a culture well plate. Dynamic seeding is where the cells suspended in media are allowed to flow through the scaffold. In theory, dynamic seeding allows for a greater level of cell penetration.

Mechanical forces have a strong effect on the deposition and resorption of bone. As force is applied to the bone, a pressure change occurs which leads to fluid flow inside the lacunae and canaliculi. This of course means that bone cells in the body are constantly being subjected flow. Studies have shown that cell growth is stimulated by flow induced shear *in vitro* [49]. Shear stresses under 25 dynes/cm^2 corresponded to an increase in cell proliferation and osteoblastic differentiation. On the other hand, shear above 25 dynes/cm^2 can cause cells to detach from the scaffold matrix [72]. Therefore, research is needed to optimize shear stresses for inducing osteoblastic cell differentiation, and also determine the shear pattern in various porous scaffold matrices.

1.2 Bioreactors for Bone Tissue Engineering

Before one begins to culture cells for bone tissue engineering, it is of utmost importance to pick the proper bioreactor. *in vitro* bone development benefits from fluid flow that provides mechanical stimulation, all while improving oxygen and nutrient delivery throughout the scaffold and removing cell waste. For most bioreactors in bone tissue engineering, the parameter that is impor-

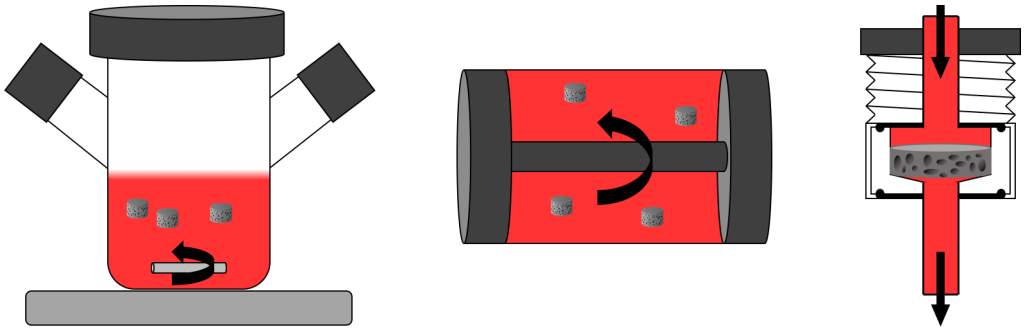

Figure 1.3: Common dynamic bioreactors used for bone tissue engineering: (left) spinner flask, (middle) rotating wall vessel, (right) perfusion flow.

tant is the shear stress associated with this fluid flow. It has been widely seen that mechanical stimulation can affect ECM production, cell proliferation, extracellular matrix (ECM) calcification, and osteogenic gene expression [81, 53, 32, 44, 20, 83, 64]. In order to properly accomplish this, three different bioreactors, shown in Figure 1.3, are commonly used: spinner flask, rotating wall vessel, and flow perfusion [81]. The following are descriptions of common bioreactors used for bone tissue engineering.

1.2.1 Static Culture Flask

The simplest and most widely used culturing system for tissue engineering is the static culture flask [64, 21, 3, 81]. In static cultures, cells are seeded on a scaffold, usually by pipetting a cell suspension on the top surface, and the construct is placed in a flask. This flask is then filled with cell culture media and stored in an incubator, with media changes occurring intermittently. Due to its simplicity, static 3D cultures are often used as experimental controls along with a static 2D culture [81, 62, 64, 65]; however, static 3D cultures suffer from severe limitations due to the fact there is no fluid flow through the scaffold porosity, or even around it. Therefore concentration gradients of

nutrients develop with potentially harmful results. Additionally, the absence of shear limits osteoblastic differentiation. Studies have shown that using 3D static culture for bone tissue engineering results in low seeding efficiency, nonhomogeneous cell distribution, unfavorable nutrient gradients, and slow ECM mineralization [81, 20, 83].

1.2.2 Spinner Flask

Spinner flask bioreactors consist of cell-seeded scaffolds suspended in media in a cylindrical vessel. The goal of this setup is to create convective flow around the scaffold, through the use of a mechanical drive or a magnetic stir bar. The stirring motion creates localized shear around the scaffolds. Unlike other dynamic culture systems, the flow environment at the surface of the scaffolds can be turbulent and may contain eddies with potentially harmful results to cells residing at the exterior surface of the scaffolds. These bioreactors have been shown to be an improvement over static cultures for seeding efficiency, cell proliferation, and differentiation, all of which are to be expected, since the presence of continuous mixing allows for the mitigation of nutrient concentration gradients [64, 69]. Unfortunately, spinner flasks are unable to efficiently deliver any siginificant amount of nutrients throughout the 3D scaffold [20, 69]. This leads to cell death near the center of the scaffold. Another problem is lack of exposure to shear stresses for cells that are located in the interior porosity of the scaffold. Even the cells on the surface get exposed to inhomogeneous shear stress distributions. Given that shear stress is a vital part of differentiation, the aforementioned inadequacies make this system inferior to perfusion systems, as will be demonstrated in later sections

[83, 64, 21].

1.2.3 Rotating Wall Vessel

Rotating wall bioreactors consist of a rotating outer cylinder, a stationary inner cylinder, and an area for the culture between them. The inner wall is gas permeable through which oxygen is supplied to the system, while the outer cylinder is impermeable to gases and induces the dynamic field [81]. Because of the nature of the system, there is a velocity gradient in the culture chamber, and under certain conditions a microgravity environment may be generated [35]. Sikavitsas et. al studied rotating wall, spinner flask, and static flask cultures over extended culture periods to compare their ability to promote osteoblastic differentiation of mesenchymal stem cells seeded on poly (lactic-co-glycolic acid) scaffolds [64]. When compared to perfusion and spinner flask types, rotating wall bioreactors offered lower overall increases for osteogenesis, ALP activity, osteocalcin secretion, mineral deposition, and scaffold cellularity; however, these values remain higher than static 3D cultures [80, 82]. A great advantage of the rotating wall vessels is their ability to generate highly controllable fluid flow environments without the generation of eddies near the scaffold surfaces. As such, rotating wall vessels are ideal for studies where tight control of surface stresses is required, but as with the spinner flask, the inability to provide any significant convection to the interior porosity limits their usefulness in bone tissue engineering studies.

1.2.4 Perfusion Flow

Perfusion bioreactors have been shown to be the most effective systems for bone tissue engineering, and it has been found that they deliver a wide range of easily manipulated shear stresses to stimulate differentiation into bone cells [81, 65, 3, 14, 62]. They usually consist of a pump, media reservoirs, scaffold chambers, and connecting tubes. There are two main types of perfusion bioreactors: scaffold perfusion and perfusion column. Perfusion columns have space surrounding the scaffolds, through which the media can flow. By doing this, media is not required to flow throughout the scaffold and therefore the shear stresses are not as easily controlled, and nutrient delivery is lowered through the interior porosity of the scaffolds. Scaffold perfusion bioreactors give better control of shear stresses by flowing media directly through the scaffolds [6, 83, 41]. This is accomplished by press-fitting the scaffold in a cassette that restricts fluid flow only through the pores of the scaffold, as shown in Figure 1.4. Assuming pore interconnectivity throughout the scaffold, fluid flow provides enhanced nutrient delivery to cells residing in all locations of the construct, and allows for better waste removal as well.

1.3 Benefits of Dynamic Bioreactor Culture

1.3.1 Mass Transfer

The main benefit for utilizing dynamic bioreactor culture is the mitigation of mass transport limitations. During extended culture, it is necessary to continually supply the cells with nutrients, such as oxygen and glucose, for them to continue to proliferate and differentiate. In static culture without

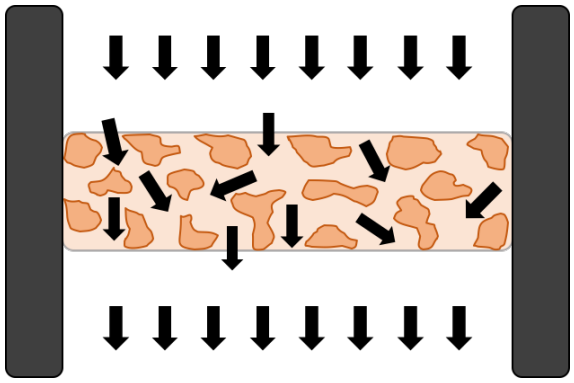

Figure 1.4: Demonstration of the benefits of a press-fit scaffold perfusion chamber. Fluid is forced to flow through the pores of the scaffold and not in the space between the scaffold and the chamber wall.

media flow, nutrients are transported to the cells in the interior of the scaffold mainly by passive diffusion. Previous studies have shown that tissues above 600 μm suffer from large hypoxic areas [67]. Therefore, only cells located near the periphery of the scaffold will have the nutrients required to proliferate. In order to culture constructs of clinically relevant size, it is necessary for bone tissue engineers to develop culture techniques that improve these undesirable nutrient gradients by adding convective mass transfer.

For the spinner flask bioreactor, the continuous mixing by the drive or stir bar generate a more homogeneous distribution of nutrients within the culture system when compared to 3D static culture [81, 64]. While this remains true for small constructs, this design type struggles to provide nutrients to the interior of larger scaffolds. As such, diffusion remains the main force for nutrient transfer in complicated architectures. A study conducted by Shea et al showed that MC3T3s were not able to penetrate beyond 200 μm into the scaffold, even after extended culture. Similar to the spinner flask, rotating wall vessels allow for increased mass transport by exhibiting a laminar flow

environment, but offer lower overall mass transport benefits for the interior porosity of the scaffold [64, 35, 80].

In comparison to the previous bioreactor types, perfusion bioreactors provide enhanced mass transport benefits. Due to the press fit cassettes, media is not only continuously supplied to the scaffold, but it also forced exclusively through the interior of the scaffold. By doing this, the nutrient gradient is mitigated, thus allowing cells to proliferate without experiencing severe hypoxic conditions [21, 67, 81, 14]. Furthermore, the unidirectional flow allows for continual waste removal from the scaffold, unlike the previous two designs.

1.3.2 Shear Stress

In the body, fluid flow induced shear forces give signals to mesenchymal stem cells to differentiate. As a force is applied to the bone, a pressure change occurs which leads to fluid flow inside the lacunae and canaliculi, leading to a signal transduction pathway resulting in these stem cells to differentiate into osteoblasts [21]. In *in vitro* environments, previous research has shown shear stresses below 15 dynes/cm^2 to have a stimulatory effect promoting osteoblastic differentiation, matrix deposition and calcification, cell proliferation, and osteogenic gene expression in 3D constructs [21, 76, 74, 66, 65].

In the literature, rotating wall vessels have been shown to provide shear induced differentiation to cells seeded near the exterior surface at a higher rate than their spinner flask counterpart [64]. This was evident by an overall higher expression of alkaline phosphatase and calcium deposition, both common markers for osteoblastic differentiation. In rotating wall bioreactors, it is also possible to use numerical models to predict the average stress experienced

by the scaffold, giving engineers more control [35].

Osteoblastic differentiation is more pronounced in perfusion systems [21, 27, 64]. Again, due to media being forced through the interior of the scaffold, the average flow induced shear forces are more controllable and more evenly distributed throughout the scaffold. Bancroft and Sikavitsas investigated the effects of varying flow rates on osteoblasts in perfusion system [63]. They found that not only did calcium deposition increase for all perfusion flow conditions in comparison to static culture, but they also found that it increased with increasing flow rate. Increasing levels of shear stress can be associated with increasing flow rate.

As with the rotating wall bioreactor, it is possible to use computational modeling to predict the localized shear forces within the scaffold. In a series of studies conducted by Voronov and VanGordon, they not only developed methods to evaluate the localized fluid shear distributions in scaffolds cultured in perfusion bioreactor systems, but they provided the framework to predict those values [76, 74, 77, 49, 75]. Most importantly, they found that constructs with a similar surface area to volume ratio will exhibit similar localized wall shear stress distributions regardless of the fabrication technique. From knowing both this and a target stimulatory shear stress, it is possible to fabricate scaffolds to express, on average, a desired shear value.

1.3.3 Cell Seeding

Cell seeding on a 3D scaffold is the first step in the development of *in vitro* bone tissue engineered constructs. Before a tissue can be grown, it is necessary to adhere cells to the surfaces, both exterior and interior, of the scaffolds, so that

they may proliferate throughout the construct. In most cases, it is preferable to have a homogeneous seeding distribution so that the tissue can grow evenly across the entirety of the scaffold surface area. This is especially true in bone tissue engineering, where the cells must not only proliferate, but also deposit mineralized tissue. Cellular adherence is measured by seeding efficiency, which is the number of cells adhered at the end of a seeding protocol in comparison to the number of cells that were initially placed on the construct.

Static seeding, or seeding that is not mediated by flow, is largely unsuitable in terms of seeding efficiency and cell distribtution. In static seeding, cells are suspended in media and either pipetted onto the surface of the scaffold or the scaffold is placed into the suspension. There are many techniques employed, such as vacuum evacuation or shaker plates, to induce cellular migration to the interior of the scaffold; however, these techniques still lead to nonhomogeneous tissue development [3, 28, 4, 79], and a higher density of cells on the outside of the scaffold during extended cultures, which is supported by the literature [79, 28]. In any case, it is necessary to find alternative methods for effectively seeding cells.

Dynamic seeding consists of adding the cells in the media, and utilizing the fluid flow environment available in the bioreactor system to help the cells navigate to the scaffold surface and potentially to the interior. The addition of flow produces higher seeding efficiency and a more homogenous cell distribution [79]. Each of the bioreactor designs presented in this chapter have been utilized to produce more homogeneous cell distributions with higher initial seeding efficiencies. Although each of the dynamic bioreactor designs may be used to accomplish this, the perfusion bioreactor is once again more efficient at

completing this task [79, 3, 28]. Alvarez et. al. investigating the effectiveness of oscillatory dynamic seeding in comparison to static seeding for bone tissue engineering applications [3, 4]. Oscillatory seeded consists of adding the cells to the media and then using a flow perfusion system to alternate the flow direction making sure that the residence time is adequate to permit cells to fully travel through the scaffold before flow direction is changed. By doing this, cells are forced back and forth, through the interior of the scaffold many times over. They found that by using this method, seeding efficiencies are increased even more so than with unidirectional flow.

1.4 Analysis Techniques

1.4.1 Imaging Analysis

During bone tissue engineering studies, there are many standardized analyzation techniques in place for evaluating constructs. These break into three categories: imaging, chemical, and mechanical. Imaging techniques look for growth, morphology, and distribution. Micro computed tomography (μCT) and scanning electron microscopy (SEM) are used to evaluate scaffolding, tissue organization, and cell morphology. A comparison of the two methods is shown in Figure 1.6. μCT is often coupled with mathematical techniques to evaluate the shear stresses throughout the scaffold [74, 51]. SEM, light microscopy, and fluorescent microscopy are the most common imaging techniques used for evaluating tissue. In order to obtain proper images, histology is first run on the tissue to get viewable cross-sections. It must also be taken into account that these microscopy-imaging techniques are all destructive.

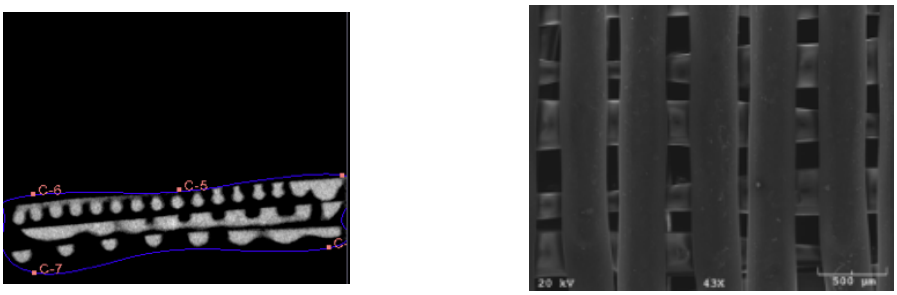

Figure 1.5: Micro-computed tomography (left) and SEM (right) images of a 3D printed scaffold. The image on the left was taken during the reconstruction process using 3D Slicer.

1.4.2 Mechanical and Chemical Analysis

Mechanical evaluation usually consists of testing the mechanical properties of constructs. This is accomplished by measuring the constructs response to different levels of stress, strain, and compression. Chemical techniques used mostly consist of microplate assays. Assays are an easy, but destructive, way to evaluate cell number, alkaline phosphatase (ALP) activity, calcium production for matrix mineralization, and biomolecule markers. Common tests include DNA, ALP, and calcium assays. If a certain gene is being looked for, usually for pathway activation, reverse-transcription polymerase chain reaction (RT-PCR) is used. Listed are four expressed genes that may be used to identify osteoblastic differentiation: Sox9, Runx2, Dlx5, and Twist1. Sox9 is more commonly associated with chondrocyte development, and regulates the development of collagen type II. Runx2 has a more direct role in osteoblastic differentiation. It not only moves cells into becoming osteoblasts, but it also impedes cells from differentiating into adipocytes or chondrocytes and stops osteoblastic maturation [10, 36, 23, 1]. Dlx5 is an important gene for axial and appendicular skeletal formation, and is necessary for chondrocytes turn-

ing hypertrophic during endochondral ossification [10, 55]. Twist1 increases the levels of Runx9 expression and studies have also shown that Twist1 suppression leads to abnormal osteoblast activity [10, 22].

1.4.3 Computational Analysis

In order to evaluate the fluid shear fields within scaffolds, previous models, such as those used by Botchwey et al and Raimondi et al, have used commercial computational fluid dynamics (CFD) programs to run the simulations using the finite element model. These processes work well for simple scaffolds; however, when examining the complex scaffolds used currently and factoring in matrix growth, these methods have not previously worked well [8, 2]. They mainly suffer from long computational time and are difficult to parallelize making them unfit for use in a supercomputer. Advances in distributed computed, however, has enabled these commercial packages to handle more computationally intensive tasks. Another approach gaining traction involves the use of the lattice Boltzmann method. This process is inherently parallelizable, deals well with sophisticated boundaries, and is computationally faster than previous methods [80].

1.5 Tumor Engineering

During the last decade, the number and effectiveness of *in vitro* cancer models have increased dramatically. Utilizing a variety of techniques for 3D culture, researchers have created models that more closely resemble and predict *in vivo* tumor drug responses; however, there is still more room for improvement. In

particular, these *in vitro* models consistently exhibit poor cell proliferation and distribution, which severely limits their predictive capabilities [33]. The number one hurdle that must be overcome is the development of tumor models that contain functional vascularization to not only delivery drugs, but also to deliver nutrients and reduce hypoxia.

During the initial synthesis process, new drugs are usually first tested in 2D cultures before moving on to *in vivo* animal models; however, these drugs do not perform the same on 3D cultures as they do in 2D. This is mainly due to how differently cancer cells behave in 3D, where they express different surface receptors, proliferation rates, and metabolic functions [33]. Due to this, 3D *in vitro* models are an important step between 2D and *in vivo* cultures [16, 68, 48, 9, 40]. By first testing drugs in a 3D *in vitro* model, researchers can gain better insight as to how the drug will affect 3D tumors before moving on to more costly and lengthy animal models. Although the funding for cancer research leads to many new drug therapy studies, the methods for testing these *in vitro* lags behind. In particular, a major problem that faces the industry is the creation of *in vitro* models that can closely align with *in vivo* conditions, and also the ability to grow large tumors that contain functional vasculature.

Above all else, the phenomena of hypoxia is the major obstacle facing the growth of functional tissues larger than a few millimeters *in vitro*. In situ tumors characteristically exhibit hypoxic centers of mass, more dense around the outer edges. These hypoxic centers induce angiogenesis and the growth of the tissue [45, 24, 38]. Engineered tumors, however, suffer from a lack of vascular growth during hypoxia [46]. Due to this, the creation of proper vascularization in engineered tissues is of utmost importance to researchers.

Significant progress has been made to alleviate this problem over the past five years with various methods being developed for testing. However the scalability of these methods is limited, negating their use in the creation of larger models. Additionally, they do not allow for intravenous drug testing; the main method of treating tumors *in vivo*. The development of constructs that can support this is necessary for more accurate *in vitro* drug response tests.

1.5.1 Importance of 3D Models

The ability to test drugs *in vitro* is a vital part of new cancer drug therapy development. It allows for a greater throughput than *in vivo* testing and is more cost effective. Though many systems have been proposed, there a few that are more widely utilized than others. Perhaps the most widely used in *in vitro* testing system is the use of multicellular cancer spheroids [38, 25]. These spheroids are large aggregates of cells and usually have diameters of around 250 μm. They have been widely used due to each individual spheroid representing a section of tissue that must be penetrated during drug delivery. The main problems with this method are that the spheroids are not capable of representing intravenous drug delivery, and each individual spheroid can only be made at a maximum of 600 μm as an increase leads to necrosis of the interior.

Another method gaining traction is the development of vascularized tumor models by using multicell sheet constructs [54]. These consist of creating many cell monolayers and stacking them on top of a resected vascular network. This method creates a perfusable system in where the cell sheets are able to receive

nutrients solely from the vessel network. The downside of the situation is that the cell sheets are immensely thin, sometimes only a single cell thick, and stacking takes a considerable amount of time. Currently, only constructs that are a maximum of 12 sheets thick have been created, only a fraction of the *in vivo* equivalents.

A promising technique is to culture tumor cells in 3D polymer scaffolds in bioreactors [26]. This method is directly analogous to tissue engineering studies, where stem cells are seeded on the scaffolds and cultured over a period of time allowing the cells to migrate, and proliferate throughout the construct. Perfusion bioreactors have proven to be the ideal method for growing these tumors due to the continuous introduction of nutrients into the system and subsequent removal of waste products. Of course with this method comes the basic limitations of growing large tissues *in vitro*. Once the tumor gains in size, nutrients are no longer able to penetrate to the interior of the mass due to the newly formed tissue decreasing the construct porosity and a lack of vasculature to transport it into the interior. In the absence of oxygen, the interior of the mass dies from hypoxia, not unlike actual tumors. However in the case of tumors, this induces vessel formation and the eventual growth in size. Therefore, these perfusion constructs be forced to create vascular networks, or we must create the vessels for them.

1.5.2 Current Fabrication Methods

Additive manufacturing, commonly referred to as rapid prototyping or 3D printing, is a class of material fabrication characterized by the process it creates 3D models: building up layer by layer. The converse is subtractive manu-

facturing, which consists of starting with a large block material and removing, or milling, pieces bit by bit. Common forms of additive manufacturing include stereolithography, bioprinting, and fused deposition modeling (FDM). In the interest of scaffold fabrication, the majority of these technologies have been utilized, but bioprinting and FDM have emerged as the top prospects [12, 70]. Bioprinting, described in the previous section, enables the creation of various scaffold architectures that are pre seeded with cells, growth factors, or other additives which has been proven to be of great use for tissue culture. In terms of vascularization, however, current technologies only allow for either smaller scale microfluidic chambers to be created, or vessels that exhibit diameters and pore sizes much larger than in tumors.

FDM has been extensively as a fabrication tool in biomedical research mainly due to the ease of which it creates complicated 3D structures, including scaffolds, with PLLA. Various cell types have successfully been cultured on PLLA scaffolds created by FDM, some of them for extended periods of time. These scaffolds exhibit better mechanical integrity than those made with bioprinting, making it a better candidate for development of vascular tree networks that can deliver media throughout 3D constructs. It is important to note that these same properties make it difficult for cells to rearrange the fibers, which is an integral step in tissue growth and angiogenesis. Therefore a coupling of techniques, spunbonded fibers in addition to FDM fibers, will be used in this proposal. Current fabricated vessels tend to have vessel diameters of up to 500 μm and pore sizes as low as 10 μm [12, 59, 60, 57, 45]. Though these have shown good results, the vessel dimensions are far cries from actual tumor vasculature. For prostate cancer, tumors have been shown

to have vessel diameters of 20-30 μm, and pore cutoff sizes for general tumors are typically below 2 μm and average around 700 nm [18, 78]. However, recent advances in FDM such as better drivers and more accurate microstepping, will allow us to create vessels with greater resolution.

1.5.3 Current Models

As previously stated, the vascularization of *in vitro* tissues is of utmost importance. To tackle this problem, Okano created vascularized cardiac tissue by overlaying cellular sheets on top of a perfusable vascular bed [60]. The vascular networks were resected from rat femoral muscles, decellularized, and then fixed in a custom-made one pass perfusion bioreactor. The bioreactor was created so that media was able to be fed into one side of the femoral vessel and out the other side. The cell sheets were made by co-culturing endothelial cells (EC) with cardiac cells in temperature responsive culture plates, which allowed for removal once full confluency was reached.

In order to gain a visual representation of the constructs interior, scanning fluorescent images were taken of 2D slices. The images presented here show the locations of the GFP expressing EC and also the locations of additional vascular networks which have been established after the start of culture. By perfusing red fluorescent dextran through the vascular bed, researchers were able to see the growth of vessels throughout the entire construct. An important finding was that the development, and subsequent full sheet infiltration, of blood vessels was intensified when the cell-sheet was cocultured with endothelial cells and/or treated with FGF-2. These induced vessels also resembled *in vivo* capillaries which is of great importance for further studies. Unfortunately,

this method was unable to create tissues of a thickness greater than 12 sheets thick. Additionally, the vascular network was unable to support the full 12 sheets resulting in a decrease in construct thickness and tissue viability. This fact leads to the proposed study that will add a more intricate design of the network in three dimensions.

Spagnoli conducted a study in which they cultured colorectal cancer cell lines in various environments including perfusion bioreactors [33]. A large number of cell lines were chosen to provide the community with the knowledge on how various cancer cell types will perform in perfusion culture. The goal of the study was to create a tissue like structures that more closely behaved like their *in vivo* counterparts when exposed to anti-cancer therapies.

The groups investigated were cells cultured in both static and perfusion bioreactors, 2D culture, and *in vivo*. *in vivo* tumors were induced by injecting 400,000 cells within Matrigel into NMRI-mice. Once the tumor volume reached 6 mm^3, the animal was sacrificed and the tumor was removed. After 7 days of culture, the constructs were evaluated for cell number, cell proliferation, tissue organization through histological staining, and tumor abundance through histomorphometric analysis. The constructs cultured in perfusion bioreactors most closely resemble the native tissue. This conclusion is also supported by both proliferation and apoptotic quantifications. In both cases, the perfusion constructs exhibited cell numbers directly comparable to the xenografts.

Following tissue culture, chemotherapeutic drugs were administered to each group in order to compare their drug sensitivity. Since colorectal cancer was the focus, five agents were used in known effective concentrations. DNA content was analyzed for each group following 48 or 96 hour incubation periods in

96 or 12 well plates. Across the board, perfusion constructs exhibited drug sensitivity better than 2D and static 3D cultures, and more similar to xenografts. They saw limited cytotoxicity, but gene expression showed elevated levels of cell stress. This study, as a whole, illustrates the ability to culture cells on 3D polymeric scaffolds using flow perfusion bioreactors, and the similarity of the tissues to native tumors before and after drug delivery. Due to this, we hypothesize that the development of prevascularized constructs will result in tissues that exhibit organization and drug response even closer to that of native tumors.

1.6 Research Objectives

As previously stated, there are three major questions this manuscript aims to answer: 1) How can we improve both mesenchymal stem cell and cancer cell adherence to the scaffolds? 2) In terms of flow-induced stresses, what is the viability of 3D printing for manufacturing repeatable scaffold architectures? 3) Do the shear stresses within a bone tissue engineered construct change over the culture period? The research objectives listed below give an overview of each of the studies presented in this manuscript, and are directly coorelated to one of the above listed questions.

1.6.1 Objective 1

The first objective (Chapter 2) was to develop a functionally flexible surface modification scheme, and test its effectiveness in increasing MSC attachment to PLLA scaffolds. The effectiveness of this technique was quantified by ex-

aming increases in cell spreading and seeding efficiency.

1.6.2 Objective 2

The second objective (Chapter 3) was to leverage the modification scheme developed in objective 1 to improve cancer cell attachment to PLLA scaffolds. Like the preceding aim, the effectiveness of this aim was measured by comparing levels of cell spreading and seeding efficiency on the modified scaffolds to those on nonmodified PLLA scaffolds.

1.6.3 Objective 3

The third objective (Chaoter 4) was to investigate the role of rapid prototyped scaffold architectures on flow-induced shear stress distributions on the walls of the scaffold. In particular, we sought to examine 1) the relationship between the shear distributions in the designed CAD models in comparison to printed scaffold reconstructions; and 2) the repeatability of shear distributions in successive printed scaffold reconstructions.

1.6.4 Objective 4

The fourth, and final objective (Chapter 5) was to monitor changes in flow-induced shear stress distributions on the walls of the scaffold over time in extended bone culture. This was accomplished using the techniques set in Objective 3, consisting of μ-CT imaging and FLUENT CFD simulations.

References

[1] R. I. Abousleiman and V. I. Sikavitsas. Bioreactors for tissues of the musculoskeletal system. *Tissue Engineering*, pages 243–259, 2006.

[2] C. K. Aidun and J. R. Clausen. Lattice-boltzmann method for complex flows. *Annual Reviews Fluid Mechanics*, 42:439–472, 2010.

[3] J. F. Alvarez-Barreto, S. M. Linehan, R. L. Shambaugh, and V. I. Sikavitsas. Flow Perfusion Improves Seeding of Tissue Engineering Scaffolds with Different Architectures. *Annals of Biomedical Engineering*, 35(3):429–442, Feb. 2007.

[4] J. F. Alvarez-Barreto and V. I. Sikavitsas. Improved Mesenchymal Stem Cell Seeding on RGD-Modified Poly(L-lactic acid) Scaffolds using Flow Perfusion. *Macromolecular Bioscience*, 7(5):579–588, May 2007.

[5] R. Auras, editor. *Poly(lactic acid): synthesis, structures, properties, processing, and applications*. Wiley series on polymer engineering and technology. Wiley, Hoboken, N.J, 2010.

[6] G. N. Bancroft, V. I. Sikavitsas, J. Van Den Dolder, T. L. Sheffield, C. G. Ambrose, J. A. Jansen, and A. G. Mikos. Fluid flow increases mineralized matrix deposition in 3d perfusion culture of marrow stromal osteoblasts in a dose-dependent manner. *Proceedings of the National Academy of Sciences*, 99(20):12600–12605, 2002.

[7] S. Bose, M. Roy, and A. Bandyopadhyay. Recent advances in bone tissue engineering scaffolds. *Trends in Biotechnology*, 30(10):546–554, Oct. 2012.

[8] Botchwey, E. A., Pollack, S. R., Levine, E. M. & Laurencin, C. T. Bone tissue engineering in a rotating bioreactor using a microcarrier matrix system. *Biomed. Mater.*, 55.2:242–253, 2001.

[9] L. J. Bray and C. Werner. Evaluation of Three-Dimensional *in Vitro* Models to Study Tumor Angiogenesis. *ACS Biomaterials Science & Engineering*, May 2017.

[10] F. Bronner and M. C. Farach-Carson. *Bone Formation*. Springer London, London, 2004. DOI: 10.1007/978-1-4471-3777-1.

[11] K. J. Burg, S. Porter, and J. F. Kellam. Biomaterial developments for bone tissue engineering. *Biomaterials*, 21(23):2347–2359, 2000.

[12] H. N. Chia and B. M. Wu. Recent advances in 3d printing of biomaterials. *Journal of Biological Engineering*, 9(1):4, Dec. 2015.

[13] E. P. Childers, M. O. Wang, M. L. Becker, J. P. Fisher, and D. Dean. 3d printing of resorbable poly(propylene fumarate) tissue engineering scaffolds. *MRS Bulletin*, 40(02):119–126, Feb. 2015.

[14] C. Chung, C. Chen, C. Chen, and C. Tseng. Enhancement of cell growth in tissue-engineering constructs under direct perfusion: Modeling and simulation. *Biotechnology and Bioengineering*, 97(6):1603–1616, Aug. 2007.

[15] C. Colnot. Cell Sources for Bone Tissue Engineering: Insights from Basic Science. *Tissue Engineering Part B: Reviews*, 17(6):449–457, Dec. 2011.

[16] B. Delalat, F. Harding, B. Gundsambuu, E. M. De-Juan-Pardo, F. M. Wunner, M.-L. Wille, M. Jasieniak, K. A. Malatesta, H. J. Griesser, A. Simula, D. W. Hutmacher, N. H. Voelcker, and S. C. Barry. 3d printed lattices as an activation and expansion platform for T cell therapy. *Biomaterials*, 140:58–68, Sept. 2017.

[17] R. Dimitriou, E. Jones, D. McGonagle, and P. V. Giannoudis. Bone regeneration: current concepts and future directions. *BMC Medicine*, 9(1):66, 2011.

[18] L. Eklund, M. Bry, and K. Alitalo. Mouse models for studying angiogenesis and lymphangiogenesis in cancer. *Molecular Oncology*, 7(2):259–282, Apr. 2013.

[19] P. V. Giannoudis, H. Dinopoulos, and E. Tsiridis. Bone substitutes: An update. *Injury*, 36(3):S20–S27, Nov. 2005.

[20] A. S. Goldstein, T. M. Juarez, C. D. Helmke, M. C. Gustin, and A. G. Mikos. Effect of convection on osteoblastic cell growth and function in biodegradable polymer foam scaffolds. *Biomaterials*, 22(11):1279–1288, 2001.

[21] M. E. Gomes, V. I. Sikavitsas, E. Behravesh, R. L. Reis, and A. G. Mikos. Effect of flow perfusion on the osteogenic differentiation of bone marrow stromal cells cultured on starch-based three-dimensional scaffolds. *Journal of Biomedical Materials Research Part A*, 67(1):87–95, 2003.

[22] Guenou, H., Kaabeche, K., Me, S. L. & Marie, P. J. . A role for fibroblast growth factor receptor-2 in the altered osteoblast phenotype induced by twist haploinsufficiency in the saethrechotzen syndrome. *Human Molecular Genetics*, 14.11:1429–1439, 2005.

[23] J. E. Hall. *Guyton and Hall Textbook of Medical Physiology: Enhanced E-book*. Elsevier Health Sciences, 2010.

[24] A. L. Harris. Hypoxia? a key regulatory factor in tumour growth. *Nature Reviews Cancer*, 2(1):38–47, Jan. 2002.

[25] F. Hirschhaeuser, H. Menne, C. Dittfeld, J. West, W. Mueller-Klieser, and L. A. Kunz-Schughart. Multicellular tumor spheroids: An underestimated tool is catching up again. *Journal of Biotechnology*, 148(1):3–15, July 2010.

[26] C. Hirt, A. Papadimitropoulos, M. G. Muraro, V. Mele, E. Panopoulos, E. Cremonesi, R. Ivanek, E. Schultz-Thater, R. A. Droeser, C. Mengus, M. Heberer, D. Oertli, G. Iezzi, P. Zajac, S. Eppenberger-Castori, L. Tornillo, L. Terracciano, I. Martin, and G. C. Spagnoli. Bioreactor-engineered cancer tissue-like structures mimic phenotypes, gene expression profiles and drug resistance patterns observed in vivo. *Biomaterials*, 62:138–146, Sept. 2015.

[27] H. L. Holtorf, J. A. Jansen, and A. G. Mikos. Flow perfusion culture induces the osteoblastic differentiation of marrow stromal cell-scaffold constructs in the absence of dexamethasone. *Journal of Biomedical Materials Research Part A*, 72A(3):326–334, Mar. 2005.

[28] C. E. Holy, M. S. Shoichet, J. E. Davies, and others. Engineering three-dimensional bone tissue in vitro using biodegradable scaffolds: investigating initial cell-seeding density and culture period. *Journal of Biomedical Materials Research*, 51(3):376–382, 2000.

[29] F. J. Hua, G. E. Kim, J. D. Lee, Y. K. Son, and D. S. Lee. Macroporous poly (L-lactide) scaffold 1. Preparation of a macroporous scaffold by liquidliquid phase separation of a PLLAdioxanewater system. *Journal of Biomedical Materials Research*, 63(2):161–167, 2002.

[30] D. W. Hutmacher. Scaffolds in tissue engineering bone and cartilage. *Biomaterials*, 21(24):2529–2543, 2000.

[31] J. P. Bilezikian and L. G. Raisz. *Principles of Bone Biology, Two-Volume Set*. Academic Press, 2008.

[32] D. Kaspar, W. Seidl, C. Neidlinger-Wilke, A. Ignatius, and L. Claes. Dynamic cell stretching increases human osteoblast proliferation and CICP synthesis but decreases osteocalcin synthesis and alkaline phosphatase activity. *Journal of Biomechanics*, 33(1):45–51, 2000.

[33] J. B. Kim. Three-dimensional tissue culture models in cancer biology. *Seminars in Cancer Biology*, 15(5):365–377, Oct. 2005.

[34] K. Kim, D. Dean, J. Wallace, R. Breithaupt, A. G. Mikos, and J. P. Fisher. The influence of stereolithographic scaffold architecture and composition on osteogenic signal expression with rat bone marrow stromal cells. *Biomaterials*, 32(15):3750–3763, May 2011.

[35] C. M. B. Kleis, S. J. The Fluid Dynamic and Shear Environment in the NASA/JSC Rotating-Wall Perfused-Vessel Bioreactor. *Biotechnology and Bioengineering*, 70(1):137, Oct. 2000.

[36] Komori, T. Regulation of osteoblast differentiation by transcription factors. *Journal Cellular Biochemicals*, 99.5:1233–1239, 2006.

[37] M. Krampera, G. Pizzolo, G. Aprili, and M. Franchini. Mesenchymal stem cells for bone, cartilage, tendon and skeletal muscle repair. *Bone*, 39(4):678–683, Oct. 2006.

[38] R.-Z. Lin and H.-Y. Chang. Recent advances in three-dimensional multicellular spheroid culture for biomedical research. *Biotechnology Journal*, 3(9-10):1172–1184, Oct. 2008.

[39] X. Liu and P. X. Ma. Polymeric scaffolds for bone tissue engineering. *Annals of Biomedical Engineering*, 32(3):477–486, 2004.

[40] A. Malandrino, R. D. Kamm, and E. Moeendarbary. In Vitro Modeling of Mechanics in Cancer Metastasis. *ACS Biomaterials Science & Engineering*, June 2017.

[41] L. Meinel, V. Karageorgiou, R. Fajardo, B. Snyder, V. Shinde-Patil, L. Zichner, D. Kaplan, R. Langer, and G. Vunjak-Novakovic. Bone tissue engineering using human mesenchymal stem cells: effects of scaffold material and medium flow. *Annals of Biomedical Engineering*, 32(1):112–122, 2004.

[42] Y. S. Nam and T. G. Park. Porous biodegradable polymeric scaffolds prepared by thermally induced phase separation. *Journal of Biomedical Materials Research*, 47(1):8–17, 1999.

[43] Y. S. Nam, J. J. Yoon, and T. G. Park. A novel fabrication method of macroporous biodegradable polymer scaffolds using gas foaming salt as a porogen additive. *Journal of Biomedical Materials Research*, 53(1):1–7, 2000.

[44] C. Neidlinger-Wilke, H.-J. Wilke, and L. Claes. Cyclic stretching of human osteoblasts affects proliferation and metabolism: a new experimental method and its application. *Journal of Orthopaedic Research*, 12(1):70–78, 1994.

[45] E. C. Novosel, C. Kleinhans, and P. J. Kluger. Vascularization is the key challenge in tissue engineering. *Advanced Drug Delivery Reviews*, 63(4-5):300–311, Apr. 2011.

[46] A. Nyga, U. Cheema, and M. Loizidou. 3d tumour models: novel in vitro approaches to cancer studies. *Journal of Cell Communication and Signaling*, 5(3):239–248, Aug. 2011.

[47] B. D. J. Ortega, N. and Z. Werb. Matrix remodeling during endochondral ossification. *Trends Cell Biology*, 14:86–93, 1997.

[48] N. Peela, D. Truong, H. Saini, H. Chu, S. Mashaghi, S. L. Ham, S. Singh, H. Tavana, B. Mosadegh, and M. Nikkhah. Advanced biomaterials and microengineering technologies to recapitulate the stepwise process of cancer metastasis. *Biomaterials*, 133:176–207, July 2017.

[49] N. H. Pham, R. S. Voronov, S. B. VanGordon, V. I. Sikavitsas, and D. V. Papavassiliou. Predicting the stress distribution within scaffolds with ordered architecture. *Biorheology*, 49(4):235–247, 2012.

[50] B. Porter, R. Zauel, H. Stockman, R. Guldberg, and D. Fyhrie. 3-D computational modeling of media flow through scaffolds in a perfusion bioreactor. *Journal of Biomechanics*, 38(3):543–549, Mar. 2005.

[51] B. Porter, R. Zauel, H. Stockman, R. Guldberg, and D. Fyhrie. 3-D computational modeling of media flow through scaffolds in a perfusion bioreactor. *Journal of Biomechanics*, 38(3):543–549, Mar. 2005.

[52] J. R. Porter, T. T. Ruckh, and K. C. Popat. Bone tissue engineering: A review in bone biomimetics and drug delivery strategies. *Biotechnology Progress*, pages NA–NA, 2009.

[53] B. Rath, J. Nam, T. J. Knobloch, J. J. Lannutti, and S. Agarwal. Compressive forces induce osteogenic gene expression in calvarial osteoblasts. *Journal of Biomechanics*, 41(5):1095–1103, 2008.

[54] G. Rijal and W. Li. 3d scaffolds in breast cancer research. *Biomaterials*, 81:135–156, Mar. 2016.

[55] Robledo, R. F., Rajan, L., Li, X. & Lufkin, T. The dlx5 and dlx6 homeobox genes are essential for craniofacial, axial, and appendicular skeletal development. *Genes Development*, 2002.

[56] A. J. Rosenbaum, D. A. Grande, and J. S. Dines. The use of mesenchymal stem cells in tissue engineering. *Organogenesis*, 4(1):23–27, Mar. 2008.

[57] J. Rouwkema, N. C. Rivron, and C. A. van Blitterswijk. Vascularization in tissue engineering. *Trends in Biotechnology*, 26(8):434–441, Aug. 2008.

[58] J. B. Safran, W. T. Butler, and M. C. Farach-Carson. Modulation of Osteopontin Post-translational State by 1,25-(OH)2-Vitamin D3: DEPENDENCE ON Ca2+ INFLUX. *Journal of Biological Chemistry*, 273(45):29935–29941, Nov. 1998.

[59] K. Sakaguchi, T. Shimizu, S. Horaguchi, H. Sekine, M. Yamato, M. Umezu, and T. Okano. In Vitro Engineering of Vascularized Tissue Surrogates. *Scientific Reports*, 3(1), Dec. 2013.

[60] T. Sasagawa, T. Shimizu, S. Sekiya, Y. Haraguchi, M. Yamato, Y. Sawa, and T. Okano. Design of prevascularized three-dimensional cell-dense tissues using a cell sheet stacking manipulation technology. *Biomaterials*, 31(7):1646–1654, Mar. 2010.

[61] Sekiya, I. Dexamethasone enhances sox9 expression in chondrocytes. *J. Endocrinol.*, 2001.

[62] V. I. Sikavitsas, G. N. Bancroft, H. L. Holtorf, J. A. Jansen, and A. G. Mikos. Mineralized matrix deposition by marrow stromal osteoblasts in 3d perfusion culture increases with increasing fluid shear forces. *Proceedings of the National Academy of Sciences*, 100(25):14683–14688, 2003.

[63] V. I. Sikavitsas, G. N. Bancroft, and A. G. Mikos. Formation of three-dimensional cell/polymer constructs for bone tissue engineering in a spinner flask and a rotating wall vessel bioreactor. *Journal of Biomedical Materials Research*, 62(1):136–148, 2002.

[64] V. I. Sikavitsas, G. N. Bancroft, J. Van Den Dolder, T. L. Sheffield, J. A. Jansen, C. G. Ambrose, and A. G. Mikos. Fluid flow increases mineralized matrix deposition in three-dimensional perfusion culture of marrow stromal osteoblasts in a dose-dependent manner. In *Engineering in Medicine and Biology, 2002. 24th Annual Conference and the Annual Fall Meeting of the Biomedical Engineering Society EMBS/BMES Conference, 2002. Proceedings of the Second Joint*, volume 1, pages 884–885. IEEE, 2002.

[65] V. I. Sikavitsas, J. v. d. Dolder, G. N. Bancroft, J. A. Jansen, and A. G. Mikos. Influence of the in vitro culture period on the in vivo performance of cell/titanium bone tissue-engineered constructs using a rat cranial critical size defect model. *Journal of Biomedical Materials Research Part A*, 67(3):944–951, 2003.

[66] V. I. Sikavitsas, J. S. Temenoff, and A. G. Mikos. Biomaterials and bone mechanotransduction. *Biomaterials*, 22:2581–2593, 2001.

[67] A. D. Simmons, C. Williams, A. Degoix, and V. I. Sikavitsas. Sensing metabolites for the monitoring of tissue engineered construct cellularity in perfusion bioreactors. *Biosensors and Bioelectronics*, 90:443–449, Apr. 2017.

[68] A. M. Sitarski, H. Fairfield, C. Falank, and M. R. Reagan. 3d Tissue Engineered in Vitro Models of Cancer in Bone. *ACS Biomaterials Science & Engineering*, July 2017.

[69] P. Sucosky, D. F. Osorio, J. B. Brown, and G. P. Neitzel. Fluid mechanics of a spinner-flask bioreactor. *Biotechnology and Bioengineering*, 85(1):34–46, Jan. 2004.

[70] J. E. Trachtenberg, P. M. Mountziaris, J. S. Miller, M. Wettergreen, F. K. Kasper, and A. G. Mikos. Open-source three-dimensional printing of biodegradable polymer scaffolds for tissue engineering: Open-source 3dp of biodegradable polymer scaffolds. *Journal of Biomedical Materials Research Part A*, pages n/a–n/a, Feb. 2014.

[71] J. P. T. M. van Leeuwen, M. van Driel, G. J. C. M. van den Bemd, and H. A. P. Pols. Vitamin D control of osteoblast function and bone extracellular matrix mineralization. *Critical Reviews in Eukaryotic Gene Expression*, 11(1-3):199–226, 2001.

[72] S. B. VanGordon. Three-dimensional bone tissue engineering strategies using polymeric scaffolds. *The University of Oklahoma. Dissertation*, 2012.

[73] L. Vico, P. Collet, A. Guignandon, M.-H. Lafage-Proust, T. Thomas, M. Rehailia, and C. Alexandre. Effects of long-term microgravity exposure on cancellous and cortical weight-bearing bones of cosmonauts. *The Lancet*, 355(9215):1607–1611, 2000.

[74] R. Voronov, S. VanGordon, V. I. Sikavitsas, and D. V. Papavassiliou. Computational modeling of flow-induced shear stresses within 3d salt-leached porous scaffolds imaged via micro-CT. *Journal of Biomechanics*, 43(7):1279–1286, May 2010.

[75] R. S. Voronov, S. B. VanGordon, R. L. Shambaugh, D. V. Papavassiliou, and V. I. Sikavitsas. 3d Tissue-Engineered Construct Analysis via Conventional High-Resolution Microcomputed Tomography Without X-Ray Contrast. *Tissue Engineering Part C: Methods*, 19(5):327–335, May 2013.

[76] R. S. Voronov, S. B. VanGordon, V. I. Sikavitsas, and D. V. Papavassiliou. Distribution of flow-induced stresses in highly porous media. *Applied Physics Letters*, 97(2):024101, 2010.

[77] R. S. Voronov, S. B. VanGordon, V. I. Sikavitsas, and D. V. Papavassiliou. Efficient Lagrangian scalar tracking method for reactive local mass transport simulation through porous media. *International Journal for Numerical Methods in Fluids*, 67(4):501–517, Oct. 2011.

[78] R. Wang, J. Xu, L. Juliette, A. Castilleja, J. Love, S.-Y. Sung, H. E. Zhau, T. J. Goodwin, and L. W. Chung. Three-dimensional co-culture models to study prostate cancer growth, progression, and metastasis to bone. *Seminars in Cancer Biology*, 15(5):353–364, Oct. 2005.

[79] D. Wendt, A. Marsano, M. Jakob, M. Heberer, and I. Martin. Oscillating perfusion of cell suspensions through three-dimensional scaffolds enhances cell seeding efficiency and uniformity. *Biotechnology and Bioengineering*, 84(2):205–214, Oct. 2003.

[80] K. Williams, S. Saini, and T. Wick. Computational Fluid Dynamics Modeling of Steady-State Momentum and Mass Transport in a Bioreactor for Cartilage Tissue Engineering. *Biotechnology Progress*, 18(5):951–963, Oct. 2002.

[81] A. B. Yeatts and J. P. Fisher. Bone tissue engineering bioreactors: Dynamic culture and the influence of shear stress. *Bone*, 48(2):171–181, Feb. 2011.

[82] T. Yoshioka, H. Mishima, Y. Ohyabu, S. Sakai, H. Akaogi, T. Ishii, H. Kojima, J. Tanaka, N. Ochiai, and T. Uemura. Repair of large osteochondral defects with allogeneic cartilaginous aggregates formed from bone marrow-derived cells using RWV bioreactor. *Journal of Orthopaedic Research*, 25(10):1291–1298, June 2007.

[83] F. Zhao, R. Chella, and T. Ma. Effects of shear stress on 3-D human mesenchymal stem cell construct development in a perfusion bioreactor system: Experiments and hydrodynamic modeling. *Biotechnology and Bioengineering*, 96(3):584–595, Feb. 2007.

Chapter 2

Biomimetic Surface Modification Platform for Bone Tissue Engineering

Abstract

Tissue engineering utilizes biomaterials, growth factors, and cells (often adult stem cells) aiming to regenerate damaged tissue or tissue that has been removed. The ability to seed and culture *in vitro* adult mesenchymal stem cells (MSC) presents unique challenges due to the inert nature of commonly used polymeric biomaterials. Mimicking the natural microenvironment of the target tissue can contribute to improving seeding efficiency and the differentiation of adult stem cells. The choice of scaffold used to support cells in culture plays a significant role in cell viability and tissue development. Scaffold properties, such as rate of degradation, hardness, and bioactivity must be

manipulated to match desirable tissue properties and the rate of tissue growth to scaffold degradation. Unmodified poly(L-lactic acid) (PLLA) scaffolds allow consistent cellular proliferation for both 2D and 3D MSC cultures, but low initial cell attachment rates result in excessive cell loss. Surface modification primarily addresses the interface that the cells directly interact with, coating underlying material that have less desirable properties. Currently, many varying modificiation techniques exist; however, these suffer from high cost and low biocomptibility. In this study, we outline a functionally flexible, biocompatible surface modification scheme for PLLA scaffolds. As a proof of concept, we modified 2D PLLA films and 3D scaffolds by linking RGD to an amine-modified surface, then confirmed the extent and longevity of the surface modification using fluorescent and spectrophotometric chemical markers. The peptide chain Arg-Gly-Asp (RGD) is known to facilitate cell adhesion. Therefore, grafting RGD to the surface of a 3D PLLA scaffold should significantly increase MSC seeding efficiency and potentially improve cell physiology without compromising the mechanical and degradation properties of the underlying PLLA.

2.1 Introduction

The field of tissue engineering primarily addresses shortcomings in tissue damage repair and organ transplants [13, 20]. By developing techniques for *in vitro* tissue culture and development, tissue engineering presents solutions to tissue

This study was completed thanks to the collaborations listed in the acknowledgments. Listed here are the author contributions: CW performed scaffold fabrication; scaffold functionalization; cell culture; fluorescent staining and imaging; image analysis. NR and MM assisted in scaffold fabrication, functionalization, and imaging.

damage-related problems which are unavailable to purely *in vivo* treatments [7, 21]. In many cases, treatment for tissue damage involves direct autologous transplant of a similar tissue from another region within the body. This approach repairs critically damaged tissue at the cost of tissue strength and integrity from the donor site. The tissue engineering approach instead extracts adult stem cells from the host nondestructively. These cells are then cultured *in vitro* with scaffolding, media, and flow stresses which mimic an *in vivo* environment, allowing the stem cells to proliferate and then differentiate into cell types which effect the desired tissue. Once properly developed, the tissue matrix is reinserted at the location requiring tissue repair, providing both material to provide support and cells optimized to mend the damaged tissue.

Bone tissue engineering utilizes mesenchymal stem cells (MSC) derived from bone marrow extract to produce osteoblasts, a key component in bone development and maintenance [4]. Osteoblastic tissue constructs developed *in vitro* will be used as grafts for delayed union or nonunion bone fractures. Currently, about 1 million delayed union or nonunion fractures occur in the U.S. each year. Standard treatment for these conditions involve an autologous bone graft, usually bone material removed from the hip. This method creates significant risk of morbidity and infection at the donor site as well as reducing the mechanical integrity of the hip bone. Development of a similar graft from MSCs would circumvent these complications [5].

The properties of the scaffold that supports the stem cells play a significant role in cell growth and differentiation and tissue development [9, 17, 19, 8, 23, 24, 11, 14]. As the supporting structure, the scaffold needs an appropriate

degree of rigidity for the target tissue. Bone tissue in particular requires rigid scaffolding. Additionally, scaffolding requires porosity or maximal surface area for nutrient transfer and cell expansion. Scaffolds must also promote cell adhesion or they would not be viable surfaces for cell culture. When exposed to the tissues native conditions, the scaffold must degrade at a rate similar to tissue development into a non-toxic product. These and other necessary and optimizable constraints place scaffold design as a central aspect of tissue engineering.

In bone tissue engineering, inoculation of MSCs onto poly (L-lactic acid) (PLLA) scaffolds results in well-documented setbacks in cellularity and cell development [9, 19, 23]. Static seeding efficiencies average about 10% cell adherence. Methods of flow perfusion of cells suspended in media through 3-D scaffolds increase efficiencies to 30-40%. Though a significant improvement over static seeding, this approach requires extensive seeding periods and complex bioreactor design. The majority of cells are still flushed away without adhering. Secondarily, due to an adjustment period known as the lag phase, cell number drops over the first 24 hours as pioneer cells dedicate more energy to developing extracellular matrix (ECM). While the establishment of ECM allows surviving cells to grow more easily with recognizable morphologies, the energy cost of producing the ECM upon adhering to a novel surface extends the timeline between marrow extraction and fracture treatment.

Modification of the scaffold to create a surface that enhances cellular adherence and extracellular matrix generation directly addresses these limitations [12, 1, 2, 24, 10, 15, 14, 16, 25]. These modified surfaces contain ECM molecules and derivatives that have been found to improve cell recognition

of the surface and present a hydrophilic interface for cells. Although several methods for surface modification have been tested, plasma treatment has been the primary method. However, this method has some difficulty in modifying internal surfaces in a 3D scaffold, and plasma exposure may alter mechanical properties of the underlying PLLA [6, 20]. The former limitation renders the plasma treatment method incompatible with 3D-scaffold flow perfusion bioreactors that subject the scaffold and cells to shear stresses similar to those present in bone structures, because cells in the interior of the scaffold will be detached. If a method for surface modification could attach biomolecules via surface interactions with a liquid solution rather than plasma exposure, then the surfaces could be biomolecule-functionalized without mechanical alteration of the interior PLLA structure.

As an alternative to polyK, in this study, small MW amine-terminated PLLA polymer were introduced to semi-permeabilized 2D and 3D PLLA scaffolds (Figure 2.1) [2]. Briefly, amine-terminated PLLA was physically entrapped on the surface of the scaffolds. Amine-modified surfaces were then crosslinked to arginine-glycine-aspartic acid (RGD) peptides using N-succinimidyl 3-(2-pyridyldithio) propionate (SPDP). Amine surface-coverage and RGD-binding were analyzed to validate the completeness and longevity of the surface modification process.

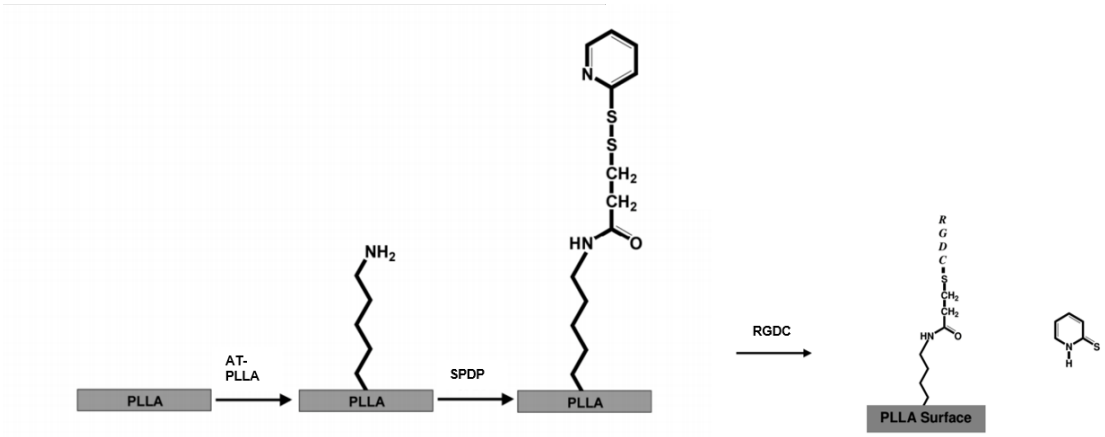

Figure 2.1: Basic amine entrapment reaction scheme. The scheme consists of the following steps: (1) physical entrapment of amine terminated PLLA on the scaffold surface, (2) crosslinking using SPDP through amine coupling, (2) RGDC functionalization using sulfur-sulfur bonding. Verification of each step shown in Figures 2.2, 2.4, and 2.7, respectively.

2.2 Materials & Methods

2.2.1 Film Preparation

2D polymer films were prepared by dissolving poly(L-lactic acid) (PLLA) (Natureworks; average MW of 100000) pellets in chloroform (Sigma-Aldrich). PLLA pellets were dissolved in chloroform at a concentration of 0.1 g/mL and then poured into either 35 mm or 75 mm dishes to form a thick or thin liquid film, respectively. These liquid films were then allowed to dry over 24 hours. Once dry, films were removed from the dishes and stored under vacuum until needed.

2.2.2 Scaffold Manufacturing

Poly(L-lactic acid) (PLLA; grade 6251D; 1.4% D enantiomer; 108,500 MW; 1.87 PDI; NatureWorks LLC) nonwoven fiber mesh scaffolds were produced

via spunbonding, as previously indicated from previous studies [23]. Scaffolds were cut from an 8mm thick PLLA mat, resulting in scaffolds of 88% porosity. A Nikon HFX-II microscope was used to evaluate fiber diameter, found to be 24.5 μm, and was confirmed by scanning electron microscopy. The pore size was determined in previous studies to be around 250 μm (120), and was confirmed by scanning electron microscopy.

3D printed scaffolds were designed custom to provide maximum nutrient penetration. 8 mm diameter cylinders were designed (SolidWorks, Waltham, MA), and sliced to produce a 65% porous fiber network (Simplify3D). Following slicing, scaffolds were printed at the following conditions: extruder temperature (215^{o}C), print head speed (150 mm/s), and a layer height (0.10 mm) on a Makerbot 5^{th} Generation Replicator (Makerbot, Inc). Scaffolds were printed on Kapton tape (McMaster-Carr) to allow adhesion to the build plate during printing and easy removal after post-curing. Pore size and fiber diameter were measured using the technique listed in the following section.

2.2.3 Porosity Measurements

Porosity was quantified (n = 12 per group) using gravimetric analysis following previous methods [18]. Briefly, sample dimensions (length, L; width, W; thickness, T) and weight ($w_{scaffold}$) were measured and used to calculate the porosity (ϵ) according to Equation 1, where $\rho_{scaffold}$ is the scaffold density and material is the density of the material.

$$\epsilon = 1 - \frac{\rho_{scaffold}}{\rho_{material}} = 1 - \frac{w_{scaffold}}{LWT\rho_{material}} \tag{2.1}$$

2.2.4 Modification Process

Bulk modification of the films began with dissolving both amine-terminated poly (L-lactic acid) (Sigma Aldrich; average MW 2500) and PLLA into chloroform at concentrations of 0.01 g/mL and 0.09 g/mL respectively. Then films were made in either 35 mm or 75 mm dishes as outlined above. Surface modification of the films began with pure PLLA films. Films were rinsed with phosphate-buffered saline (PBS) then incubated in 1 mL of 70% acetone in water for 1 h with moderate shaking, while scaffolds were modified in 2 mL. The acetone mixture was then aspirated and films were incubated in 1 mL of DMSO with 0.2 mg/mL small MW amine-terminated PLLA for 12 h again with moderate shaking, with scaffolds again being incubated in 2 mL. After that, films and scaffolds were rinsed with DI H_2O and left to vacuum dry for 24 h. The water rinse insures the short chain amine terminated PLLA is caught in the surface of the long chain PLLA.

Following bulk or surface small MW amine-terminated PLLA modification, functionalization was completed through the chemical linking of N-succinimidyl 3-(2-pyridyldithio) propionate (SPDP) (Thermo Scientific) and Arg-Gly-Asp-Cys peptide (RGDC) (Bachem) to the surface, shown in Figure 1. Films were rinsed with PBS then incubated at 25 ^oC on a shaker in 1 mL of 0.04 mmol/mL SPDP in DMSO diluted with PBS to 0.01 mmol/mL SPDP with a pH of 7.4 for 30 min. SPDP solution was aspirated and films were incubated at 40^oC in 1 mL of 0.045 mg/mL RGDC in HEPES solution with a pH of 8.3 for 90 min. Films were then rinsed with PBS and left to vacuum dry for 24 hours before chemical sterilization.

2.2.5 Fluorescent Surface Amine Analysis

NHS rhodamine was used to determine the surface concentration of primary amine groups following initial small MW amine-terminated PLLA surface or bulk modification. Films were incubated at 25 ^{o}C on a shaker plate in 1 mL of 0.2 mg/mL NHS rhodamine in PBDS for 30 minutes, while scaffolds underwent the same rinses in 2 mL of solution. They were then rinsed with 15 min periods on the shaker plate in 1% PBST followed by two DI H_2O rinses. Each sample was imaged on a Nikon Eclipse E800 microscope. Fluorescent intensity was quantified using ImageJ image analysis software. Surface modified films were compared to bulk modified films as a control for surface presence and distribution of small MW amine-terminated PLLA.

2.2.6 Spectrophotometric RGDC Binding Analysis

The SPDP linkage with RGDC was confirmed using spectrophotometry of the HEPES media following the RGDC incubation period. As the reaction proceeds, pyridine 2-thione is released from the SPDP molecule.

2.2.7 Cell Expansion and Seeding

Adult mesenchymal stem cells were extracted from the tibias and femurs of male Wistar rats (Harlan Laboratories) using methods identified in previous publications [22, 1]). Cells were cultured at 37 ^{o}C, and 5% CO_2 in standard α-MEM (Invitrogen) supplemented with 10% fetal bovine serum (Atlanta Biologicals) and 1% antibiotic-antimycotic (Invitrogen). Passage 2 cells were used for this study at a density of 2 million cells/mL for scaffold seeding.

We prepped the scaffolds for cell seeding using an established pre-wetting

technique [2]. Vacuum air removal of scaffolds was conducted in 75% ethanol. Pre-wet scaffolds were placed in cassettes within a flow perfusion bioreactor for one hour in α-MEM at a flow rate of 0.15 mL/min to remove any remaining ethanol [18, 3]. Following the flush, 2 million MSCs/150 μL of α-MEM were pipetted in each each scaffold chamber. After seeding, the bioreactor was allowed to rest for two hours, without flow, to facilitate cell attachment.

2.2.8 Construct Cellularity

The number of cells present in each construct was evaluated using fluorescent PicoGreen dsDNA assay (Invitrogen). At each sacrificial time point, the construct was removed from the cassette and dunked in PBS to remove any cells not adhered to the scaffold. Subsequently, the scaffolds were chopped into eight pieces, placed in 1 mL of DI H_2O, and stored at -20^{o}C. Each construct underwent three freeze/thaw cycles to lyse the cells. After following supplier protocols, solutions were run on a Synergy HT Multi-Mode Microplate Reader (Bio-Tek) at an excitation wavelength of 480 nm and an emission wavelength of 520 nm. All samples and standards were run in triplicate.

2.2.9 Fluorescent Nucleus and Actin Staining

Three scaffolds at each time point were subjected to hoechst and phallacidin staining. This was done to confirm the cellularity result from the above ds-DNA assay as well as to provide information on cell distribution within the scaffold in addition to matrix deposition. Scaffolds were resected from culture, rinsed with PBS, and fixed in solution of 4% formalin in PBS for 15 minutes at 25 ^{o}C. Following this, samples were rinsed in three consecutive PBS washes.

They were then permeabilized in a solution of 0.5% PBST (PBS and Triton X-100) for 15 minutes at 25 ^{o}C. Fixed and permeabilized samples were stained using hoechst 33342 and phalloidin (ReadyProbes NucBlue and ActinGreen 488; Thermofisher Scientific) using manufacturer protocols. After incubation, scaffolds were rinsed thoroughly with PBS before imaging on a Nikon Epi-fluorescence microscope. Image analysis was performed with MetaMorph 6.2 (Universal Imaging Corporation) and Image J software packages.

2.2.10 SEM Preperation and Imaging

Samples were prepared for SEM imaging by rinsing them in PBS after removing from culture. These samples were then fixed overnight in 4% formalin at 25 ^{o}C. Following fixation, samples were rinsed in ethanol concentrations ranging from 70% to 100%. Samples were then removed from solution and allowed to dry for 48 hours under vacuum. After mounting to SEM mounts, the samples were sputter-coated in gold palladium using a Hummer VI Triode Sputter Coater (Anatech Ltd.). SEM images were produced using a Zeiss 960 scanning electron microscope (SEM, Carl Zeiss SMT Inc) at 15kV. Digital images were captured using EDS 2006 and EDS 2008 digital imaging software (IXRF Systems).

2.2.11 Statistical Analysis

A one-way analysis of variance (ANOVA) was used to compare mean $\pm$ standard deviation of pore and fiber measurements, in which Tukeys Honestly Significant Difference (HSD) test was performed to identify significant differences (p-value < 0.05). One-way ANOVA and Tukeys HSD were used to

compare the rest of the data. All statistical analysis was performed using a custom python code utilizing the open source Numpy, matplotlib, and SciPy libraries.

2.3 Results

2.3.1 Surface Activity

Validation of the physical entrapment of the small MW amine-terminated PLLA on the surface was performed initially using the NHS rhodamine fluorescent probe for primary amine groups. Films modified with 0.2 mg/mL small MW amine-terminated PLLA in DMSO and unmodified PLLA films were imaged with and without NHS rhodamine treatment following 7 days of vacuum storage. Bulk modified films are shown in Figure 2.2, and surface modified films are shown in Figure 2.3. Unmodified films showed a statistically negligble amount of fluorescence. The modified film displayed pervasive fluorescence while the control film displayed mild dispersed fluorescence indicative of low-level physisorption of the NHS rhodamine probe. No untreated samples demonstrated fluorescence. Modification of 3D scaffolds was also observed using 3D-printed PLLA scaffolds. Images indicate similar surface coverage of the modified scaffold and minor physisorption on the unmodified scaffold (Figure 2.3). A bright field image of the unmodified scaffold was taken as reference for the structure of the 3D-printed scaffold.

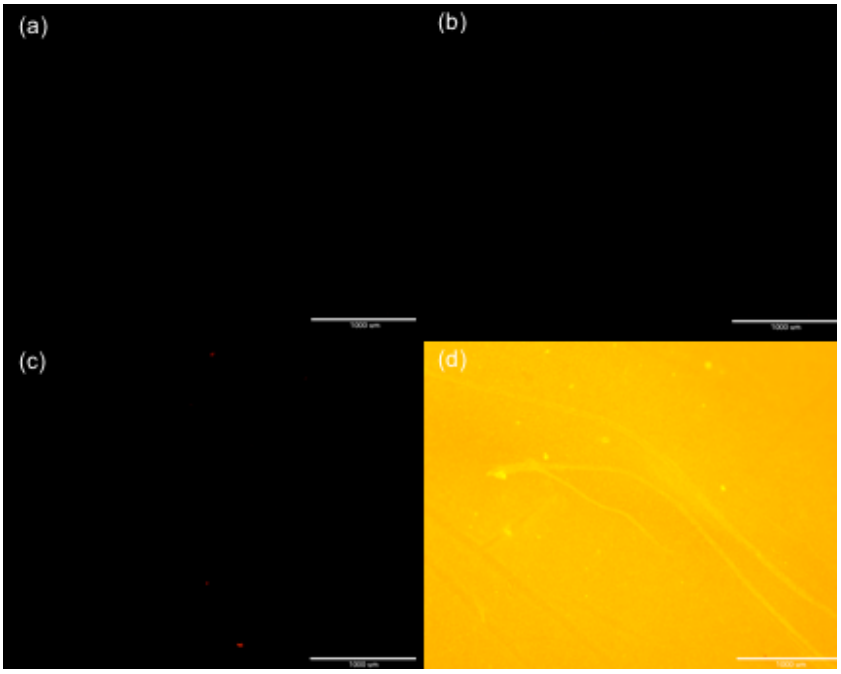

Figure 2.2: Fluorescent micrographs of surface verification treated with NHS rhodamine demonstrating the presense of amine groups on 2D PLLA films. (A): unmodified. (B): acetone soak without amine-terminated PLLA (C): full modification (D): acetone soak with amine-terminated PLLA with H_2O. Scale bar is 1000 μm.

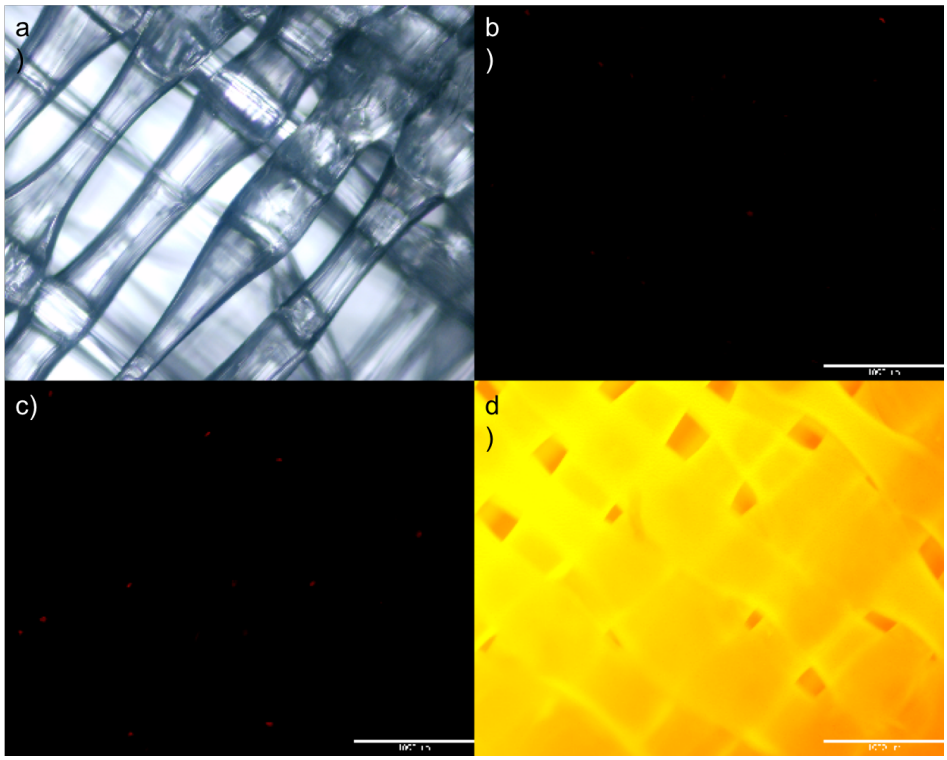

Figure 2.3: Fluorescent micrographs of surface verification treated with NHS rhodamine demonstrating the presense of amine groups on 3D printed scaffolds. (A): unmodified. (B): acetone soak without amine-terminated PLLA (C): full modification (D): acetone soak with amine-terminated PLLA with H_2O. Scale bar is 1000 μm.

2.3.2 Surface Modification Validation

Completion of the surface modification process was confirmed using spectrophotometric analysis of the solutions used in the reactions, shown in Figure 2.4. For each solution, six samples were taken (n = 6). The first solution was a 1 ml PBS rinse of a small MW amine-terminated PLLA modified film. The second solution was 1 ml of RGDC in HEPES solution exposed to an small MW amine-terminated PLLA modified film. The third solution was 1 mL of the SPDP solution exposed to a small MW amine-terminated PLLA modified film. The fourth solution was 1 mL of RGDC in HEPES solution exposed to an small MW amine-terminated PLLA+SPDP modified film. This solution displayed a significant increase in absorbance ($p < 0.01$) due to the release of pyridine 2-thione when SPDP reacts with the sulfhydryl in RGDC.

2.3.3 Surface Modification Longevity

With vacuum preservation, the initial physical entrapment of small MW amine-terminated PLLA will maintain consistent surface coverage for a period of over a week. For 7 days following small MW amine-terminated PLLA surface modification, scaffold samples were analyzed for fluorescent intensity to determine the longevity of the physical entrapment (Figure 2.5). Samples displayed fluorescent intensity within 20-25 units with no significant decrease as time progressed.

2.3.4 Surface Concentration Control

Figure 2.6 shows the fluorescent dual staining of cell seeded 2D films and Figure 2.7 compares the surface area per cell with varying surface concentrations of

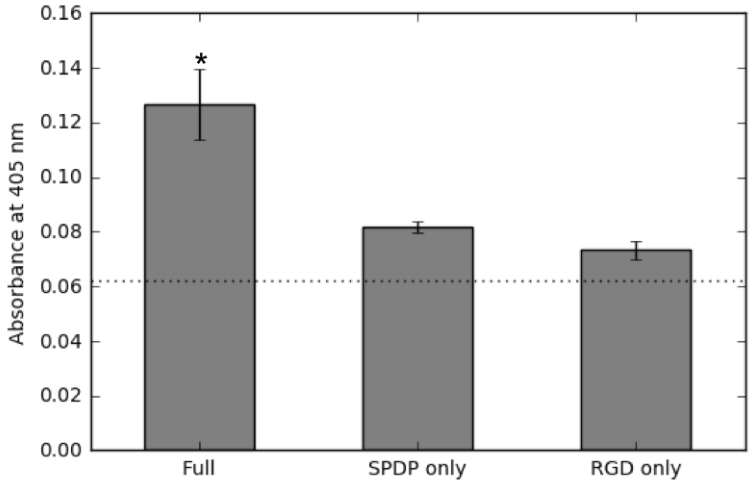

Figure 2.4: Detection of pyridine-2-thione released during the modification process with different techniques. When SPDP linked to the aminated surfaces is reacted with a secondary peptide it releases pyridine-2-thione, developing a green color whose absorbance can be read at 405 nm. The dotted line represents the baseline absorbance of PLLA. Values are given as the mean ± standard error of the mean (n = 3). Significance is indicated by $*$ ($p < 0.01$).

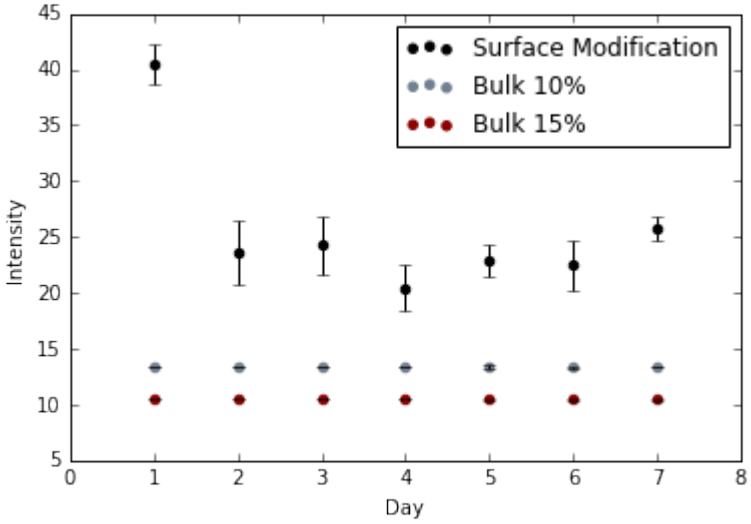

Figure 2.5: Surface activity of aminated surfaces over one week for surface modified versus bulk modified methods. When NHS rhodamine is reacted with each construct prior to fluorescent imaging, it attaches to free amine groups, which can be quantified using fluorescent imaging. Values are given as the mean ± standard error of the mean (n = 3).

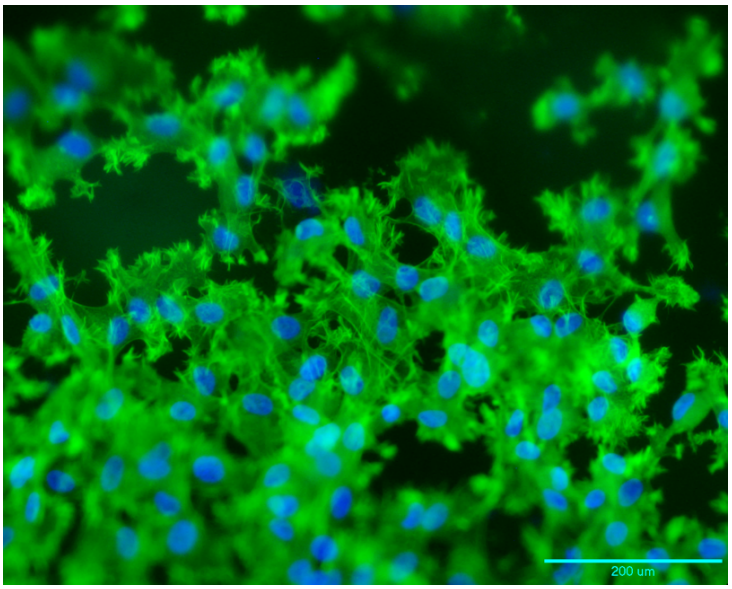

Figure 2.6: Fluorescent dual staining of fixed MSCs. Stains were completed using hoechst and phallacidin to stain the cell nucleus and actin, respectively.

RGD. Error bars are shown, but are so small they are difficult to see. It is evident that there is a continual increase in cell surface area with surface area. The drop at a concentration of 10^{-1} can be attributed to cell death due to over stimulation by RGD, which has been discussed in the literature [2].

2.4 Discussion

In order to validate the functionalization process, films and scaffolds were prepared that contained the free terminal amine groups. The samples were incubated with NHS rhodamine, a fluorescent amine coupling tag. Figure 2.2 and Figure 2.3 show the results of this process. The control groups (A-C) express little to physisorption indicating no free amine groups are expressed; while the amine functionalized group (D) shows a clear fluoresence indicating free amine groups are expressed on the surface. This result shows a successful

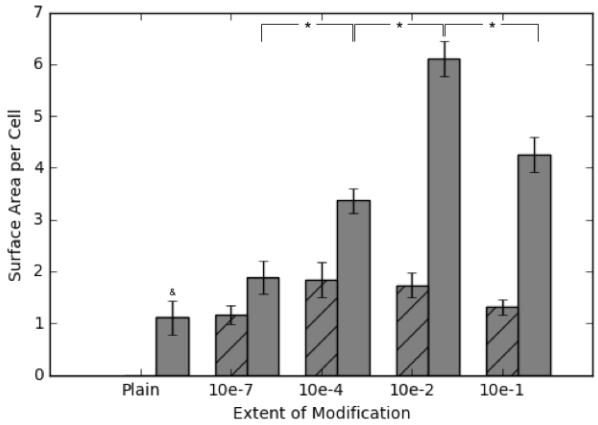

Figure 2.7: Effect of the extent of amine-terminated entrapment on mesenchymal stem cell surface area after linkage of argininеglycineaspartic acidcysteine (RGDC) peptides to amine groups entrapped in poly(L-lactic acid) discs. The concentrations listed are amount of RGD in solution that were available for reaction. Controls (striped lines) indicate scaffolds that were amine-modified only. The dotted line represents the baseline absorbance of PLLA. Values are given as the mean ± standard error of the mean (n = 3). & signifies the significantly lowest value. Significance calculated via ANOVA with Tukey HSD Post-hoc analysis.

amine termination scheme.

To test the viability of the second modification stage, levels of pyridine-2-thione were measured. This fluorescent moiety is released following complete SPDP conjugation. Samples were modified using the complete process: including amine termination, SPDP crosslinking, and RGD functionalization, with the samples being measured from the reaction solution. As shown in Figure 2.4, there is a stasticially signigicant elevation of pyridine-2-thione released following RGD functionalization. This same elevation is not seen in following the intermediate steps, equating to no activiation of pyridine-2-thione release. Again, this result indicates the successful binding of RGDC to those aforementioned free amines.

Additionally, surface longevity of free amine expression was measured. Films and scaffolds were modified to express free amines. Those samples were then stored under vacuum for up to 7 days to allow for amine release. One week was chosen for testing due to this being the minimal time necessary for an off the shelf material to be adopted for clinical use according to our market research. Before testing, samples were rinsed in DI H2O and dried under vacuum. Following this, samples were incubated in NHS rhodamine and imaged by fluorescent microscopy, where Figure 2.5 shows the results of this process. It is evident from the results, that surface modification expresses higher amounts of amine termination over the tested time frame in comparison to bulk modification. A large drop off between Days 1 and 2 is seen before intesity levels off. We believe this decrease is due to shallow amine group penetration during the modification process, which quickly falls off. This is supported by the bulk results, which to do exhibit the same initial drop off. In fact, bulk modification

amine intensity levels remain constant throughout the 7 days indicating very strong binding.

Finally, the surface area per cell, or cell stretching, was investigated for varying levels of RGD modficiation. The surface area per cell is a measure of the actin and nucleus surface area normalized for the number of cells on the surface. This measurement is a common method of quantifying the strength of cellular binding to a surface. Figure 2.7 shows an increase of cell spreading as the amount of RGD modification is increased. This fact shows that by using our modification process, we are able to tightly control the extent of RGD modification, and, by extension, the strength of cell adhesion. We attribute the decrease in cell spreading at 10^{-1} to be associated with over stimulation of the cells resulting in cell death and detachment, which has been previously reported as a negative effect of RGD [2].

2.5 Conclusion

In this study we aimed to develop a physical entrapment surface amination technique for PLLA scaffolds that took advantage of PLLAs partial solubilization in acetone. We improved upon past work by using amine-terminated PLLA, a simple molecule with a single functional primary amine attached to a short chain of PLLA as opposed to previously employed Poly-ϵ-Cbz-L-lysine which does not meet FDA clinical standards. By introducing small MW amine-terminated PLLA during the acetone soak, we also removed the DMSO soak which may have resulted in physical entrapment of DMSO molecules and supported further undesirable surface modifications. DMSO has also been effectively removed from the subsequent covalent modifications by the use of an

acetone + SPDP crosslinker soak. The physical entrapment method of surface modification of PLLA scaffolds results in thorough coverage on both 2D films and 3D scaffolds. In vacuum conditions, this modification resists degradation up to 7 days. Significant binding of the desired protein takes place on this surface. Lastly, we are able to tightly control the strength of cell adhesion to the modified surface by varying the extent of RGD functionalization.

Future work will quantify surface concentrations of the modifications and degradation over a greater period of time. The amination technique will be applied to 3D PLLA scaffolds to determine penetration into the inner surfaces, and cells will be cultured under shear stresses from flow perfusion of media, replicating blood flow through bone tissue. Cell morphology, migration, and differentiation will be considered in response to the modifications. Finally, cells will be cultured on modified films for longer periods of time to analyze the transition from designed biomimetic surfaces to deposited ECM.

2.6 Acknowledgements

I acknowledge the following collaborators: Nathan Richbourg and Montana Minnis. I acknowledge support from the Oklahoma Center for the Advancement of Science and Technology (HR13-214). I gratefully acknowledge fellowship funding from the Oklahoma Louis Stokes Alliance for Minority Participation (OK-LSAMP) Bridge to the Doctorate, Cohort 6 (EHR/HRD #1249206). Any opinions, findings and conclusions or recommendations expressed in this material are those of the authors and do not necessarily reflect the views of the National Science Foundation.

Supplemental Figures

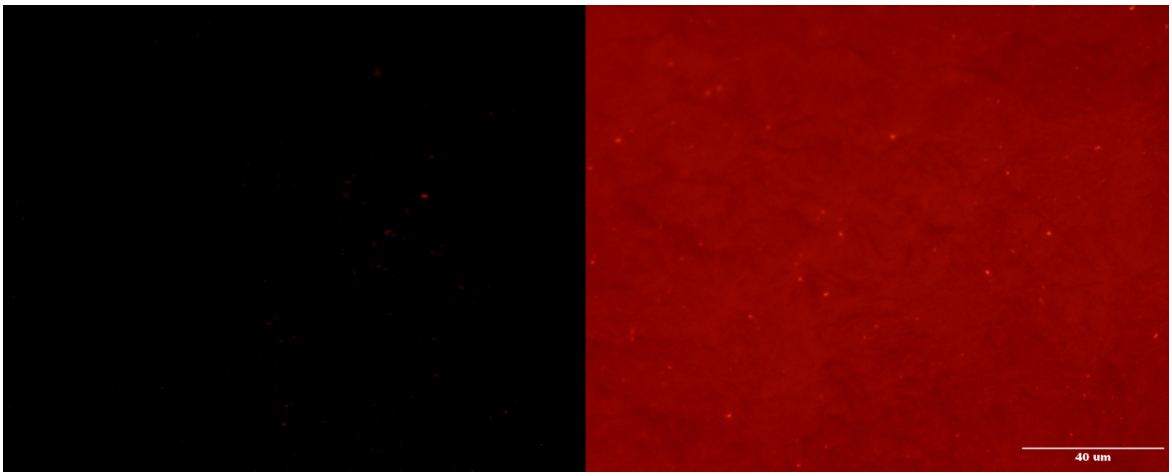

Figure 2.8: Fluorescent micrographs of bulk modified films using NHS rhodamine. (A): unmodified. (B): modified. Unmodified indicates plain PLLA. Modified indicates films that have been functionalized to express free amine groups.

References

[1] J. F. Alvarez-Barreto, S. M. Linehan, R. L. Shambaugh, and V. I. Sikavitsas. Flow Perfusion Improves Seeding of Tissue Engineering Scaffolds with Different Architectures. *Annals of Biomedical Engineering*, 35(3):429–442, Feb. 2007.

[2] J. F. Alvarez-Barreto and V. I. Sikavitsas. Improved Mesenchymal Stem Cell Seeding on RGD-Modified Poly(L-lactic acid) Scaffolds using Flow Perfusion. *Macromolecular Bioscience*, 7(5):579–588, May 2007.

[3] G. N. Bancroft, V. I. Sikavitsas, J. Van Den Dolder, T. L. Sheffield, C. G. Ambrose, J. A. Jansen, and A. G. Mikos. Fluid flow increases mineralized matrix deposition in 3d perfusion culture of marrow stromal osteoblasts in a dose-dependent manner. *Proceedings of the National Academy of Sciences*, 99(20):12600–12605, 2002.

[4] F. Bronner and M. C. Farach-Carson. *Bone Formation*. Springer London, London, 2004. DOI: 10.1007/978-1-4471-3777-1.

[5] A. Civantos, E. Martnez-Campos, V. Ramos, C. Elvira, A. Gallardo, and A. Abarrategi. Titanium Coatings and Surface Modifications: Toward Clinically Useful Bioactive Implants. *ACS Biomaterials Science & Engineering*, 3(7):1245–1261, July 2017.

[6] C. Colnot. Cell Sources for Bone Tissue Engineering: Insights from Basic Science. *Tissue Engineering Part B: Reviews*, 17(6):449–457, Dec. 2011.

[7] R. Dimitriou, E. Jones, D. McGonagle, and P. V. Giannoudis. Bone regeneration: current concepts and future directions. *BMC Medicine*, 9(1):66, 2011.

[8] A. Henslee, P. Spicer, D. Yoon, M. Nair, V. Meretoja, K. Witherel, J. Jansen, A. Mikos, and F. Kasper. Biodegradable composite scaffolds incorporating an intramedullary rod and delivering bone morphogenetic protein-2 for stabilization and bone regeneration in segmental long bone defects. *Acta Biomaterialia*, 7(10):3627–3637, Oct. 2011.

[9] D. W. Hutmacher. Scaffolds in tissue engineering bone and cartilage. *Biomaterials*, 21(24):2529–2543, 2000.

[10] W. Jiang, Q. Tian, T. Vuong, M. Shashaty, C. Gopez, T. Sanders, and H. Liu. Comparison Study on Four Biodegradable Polymer Coatings for Controlling Magnesium Degradation and Human Endothelial Cell Adhesion and Spreading. *ACS Biomaterials Science & Engineering*, 3(6):936–950, June 2017.

[11] P. Kerativitayanan, M. Tatullo, M. Khariton, P. Joshi, B. Perniconi, and A. K. Gaharwar. Nanoengineered Osteoinductive and Elastomeric Scaffolds for Bone Tissue Engineering. *ACS Biomaterials Science & Engineering*, 3(4):590–600, Apr. 2017.

[12] Komori, T. Regulation of osteoblast differentiation by transcription factors. *Journal Cellular Biochemicals*, 99.5:1233–1239, 2006.

[13] K. Y. . E.-A. S. F. Laurencin, C. Bone graft substitutes. *Exp. Rev. Medical Dev.*, pages 49–57, 2006.

[14] J. K. Leach and J. Whitehead. Materials-Directed Differentiation of Mesenchymal Stem Cells for Tissue Engineering and Regeneration. *ACS Biomaterials Science & Engineering*, Mar. 2017.

[15] J. Lee, S. K. M. Perikamana, T. Ahmad, M. S. Lee, H. S. Yang, D.-G. Kim, K. Kim, B. Kwon, and H. Shin. Controlled Retention of BMP-2-Derived Peptide on Nanofibers Based on Mussel-Inspired Adhesion for Bone Formation. *Tissue Engineering Part A*, 23(7-8):323–334, Apr. 2017.

[16] S. Li, Y. Xu, J. Yu, and M. L. Becker. Enhanced osteogenic activity of poly(ester urea) scaffolds using facile post-3d printing peptide functionalization strategies. *Biomaterials*, 141:176–187, Oct. 2017.

[17] X. Liu and P. X. Ma. Polymeric scaffolds for bone tissue engineering. *Annals of Biomedical Engineering*, 32(3):477–486, 2004.

[18] Mikos. Flow perfusion culture of mesenchymal stem cells for bone tissue engineering. *StemBook*, 2008.

[19] B. D. J. Ortega, N. and Z. Werb. Matrix remodeling during endochondral ossification. *Trends Cell Biology*, 14:86–93, 1997.

[20] J. R. Porter, T. T. Ruckh, and K. C. Popat. Bone tissue engineering: A review in bone biomimetics and drug delivery strategies. *Biotechnology Progress*, pages NA–NA, 2009.

[21] V. I. Sikavitsas, G. N. Bancroft, H. L. Holtorf, J. A. Jansen, and A. G. Mikos. Mineralized matrix deposition by marrow stromal osteoblasts in 3d perfusion culture increases with increasing fluid shear forces. *Proceedings of the National Academy of Sciences*, 100(25):14683–14688, 2003.

[22] S. B. VanGordon. Three-dimensional bone tissue engineering strategies using polymeric scaffolds. *The University of Oklahoma. Dissertation*, 2012.

[23] S. B. VanGordon, R. S. Voronov, T. B. Blue, R. L. Shambaugh, D. V. Papavassiliou, and V. I. Sikavitsas. Effects of Scaffold Architecture on Preosteoblastic Cultures under Continuous Fluid Shear. *Industrial & Engineering Chemistry Research*, 50(2):620–629, Jan. 2011.

[24] E. R. Wagner, J. Parry, M. Dadsetan, D. Bravo, S. M. Riester, A. J. van Wijnen, M. J. Yaszemski, and S. Kakar. Chondrocyte Attachment, Proliferation, and Differentiation on Three-Dimensional Polycaprolactone Fumarate Scaffolds. *Tissue Engineering Part A*, Mar. 2017.

[25] T.-T. Yu, F.-Z. Cui, Q.-Y. Meng, J. Wang, D.-C. Wu, J. Zhang, X.-X. Kou, R.-L. Yang, Y. Liu, Y. S. Zhang, F. Yang, and Y.-H. Zhou. Influence of Surface Chemistry on Adhesion and Osteo/Odontogenic Differentiation of Dental Pulp Stem Cells. *ACS Biomaterials Science & Engineering*, 3(6):1119–1128, June 2017.

Chapter 3

N-Cadherin Mediated Enhancement of Cancer Cell Adhesion on Poly(l-lactic acid) Scaffolds under Flow Perfusion for the Development of *in vitro* Tumor Models

Abstract

During the last decade, the number and effectiveness of *in vitro* cancer models have increased dramatically. Utilizing a variety of techniques for 3D culture, researchers have created models that more closely resemble and predict *in*

vivo tumor drug responses; however, there is still more room for improvement. In particular, these *in vitro* models consistently exhibit poor cell proliferation and distribution, which severely limits their predictive capabilities. The number one hurdle that must be overcome is the poor adhesion that cancer cells have to non hydrogel scaffolds, which severely limits the development of tumor models that contain fully developed tissue. To combat this, we have successfully seeded various cancer cell lines (PC3, MDA, and B16) on three dimensional poly (l-lactic) acid scaffolds, and cultured them for up to three weeks in perfusion bioreactors with samples taken intermittently. By using oscillatory seeding and surface modifications, we are able to increase seeding efficiency and, subsequently, the distribution of cells throughout the construct. Through the use of biochemical assays, fluorescent imaging, and μCT we are able to identify that these constructs behave more closely to native cancer tissue.

3.1 Introduction

During the initial synthesis process, new drugs are usually first tested in 2D cultures before moving on to *in vivo* animal models; however, these drugs do not perform the same on 3D cultures as they do in 2D. This is mainly due to how differently cancer cells behave in 3D, where they express different surface receptors, proliferation rates, and metabolic functions [11]. Due to this, 3D *in vitro* models are an important step between 2D and *in vivo* cultures. By

This study was completed thanks to the collaborations listed in the acknowledgments. Listed here are the author contributions: CW performed scaffold fabrication; scaffold functionalization; cell culture; fluorescent staining and imaging; image analysis. PM performed fluorescent staining and imaging. and MM assisted in scaffold fabrication, functionalization, and imaging.

first testing drugs in a 3D *in vitro* model, researchers can gain better insight as to how the drug will affect 3D tumors before moving on to more costly and lengthy animal models. Although the funding for cancer research leads to many new drug therapy studies, the methods for testing these *in vitro* lags behind. In particular, a major problem that faces the industry is the creation of *in vitro* models that can closely align with *in vivo* conditions, and also the ability to grow large tumors.

Above all else, the phenomena of hypoxia is the major obstacle facing the growth of functional tissues larger than a few millimeters *in vitro*. In situ tumors characteristically exhibit hypoxic centers of mass, more dense around the outer edges. These hypoxic centers induce angiogenesis and the growth of the tissue [7]. Engineered tumors, however, suffer from a lack of vascular growth during hypoxia [8]. Due to this, the creation of proper vascularization in engineered tissues or utilizing flow systems that maximize nutrient deliver. Significant progress has been made to alleviate this problem over the past five years with various methods being developed for testing [6, 14, 13, 5, 9]. However the scalability of these methods is limited, negating their use in the creation of larger models.

A promising technique is to culture tumor cells in 3D polymer scaffolds in bioreactors [7, 8, 11]. This method is directly analogous to tissue engineering studies, where stem cells are seeded on the scaffolds and cultured over a period of time allowing the cells to migrate, and proliferate throughout the construct. Perfusion bioreactors have proven to be the ideal method for growing these tumors due to the continuous introduction of nutrients into the system and subsequent removal of waste products. The limiting factor for this method is

initial cellular adhesion. When compared to mesenchymal stem cells, cancer cells exhibit significantly lower adhesion rates. This fact means that it will take significantly longer to culture a dense tissue.

To combat this major issue, we have leveraged our patented biomimetic surface modification platform for tumor engineering applications. In particular, we have identified various moieties specific to certain tumors that are integral to cellular adhesion, and have used these to modify our scaffolds and trick the cancer cells into exhibiting higher rates of adhesion. For instance, in terms of prostate cancer, poly(L-lactic acid) (PLLA) scaffolds were modified to express n-cadherin, which is a highly upregulated protein used for cellular adhesion. N-cadherin has been shown to be very important in tumors with metastatic potential by contributing to both cell-to-cell adhesion (Figure 3.1), and osteoblastic differentiation in stem cells (Figure 3.2). Most importantly for tumor cell adhesion, its role is the activation of β-catenin, a major player in Wnt signaling. This activation will allow for α-catenin to attach to the non dominant binding site on β-catenin's ARM domain. The role of α-catenin is to attach directly to actin filaments, increasing cell adhesion. For the study as a whole, we will be seeding various cancer cell lines (PC3, MDA, and B16) on both 2D and 3D PLLA scaffolds, and culturing them under increasing shear levels in perfusion bioreactors with samples taken intermittently. Through the use of various biochemical assays, fluorescent microscopy, and μCT we identified that these constructs behave more closely to native cancer tissue in comparison to those grown using non-functionalized scaffolds. After cell seeding, we were able to significantly increase seeding efficiency and potentially improve cell physiology without compromising the mechanical and degrada-

tion properties of the underlying PLLA.

3.2 Materials & Methods

3.2.1 Film Preparation

Poly(L-lactic acid) (Natureworks; average MW 100,000) films were prepared by dissolution of PLLA pellets in chloroform followed by evaporative deposition. PLLA pellets were dissolved in chloroform at a concentration of 0.1 g/mL and then poured into 35 mm dishes to form a liquid film and dry over 24 hours. Once dry, films were removed from the dishes and kept in a pressurized chamber until use.

3.2.2 Scaffold Manufacturing

Poly(L-lactic acid) (PLLA; grade 6251D; 1.4% D enantiomer; 108,500 MW; 1.87 PDI; NatureWorks LLC) nonwoven fiber mesh scaffolds were produced via spunbonding, as previously indicated from previous studies [16]. Scaffolds were cut from an 8mm thick PLLA mat, resulting in scaffolds of 88% porosity. A Nikon HFX-II microscope was used to evaluate fiber diameter, found to be 24.5 μm, and was confirmed by scanning electron microscopy.

3D foam scaffolds were made using solvent-cast porogen-leaching [3, 12]. Breifly, PLLA pellets were dissolved in chloroform at a concentration of 0.1 mg/mL. NaCl was sieved to obtain grains between 250-350 μm (Sigma-Aldrich). Following this, up to 5 g of NaCl was poured in 35 μm or 75 μm glass petri dishes. After making an even bed of salt grains, the PLLA solution was poured over the bed, and the dishes were allowed to dry for 24 hours.

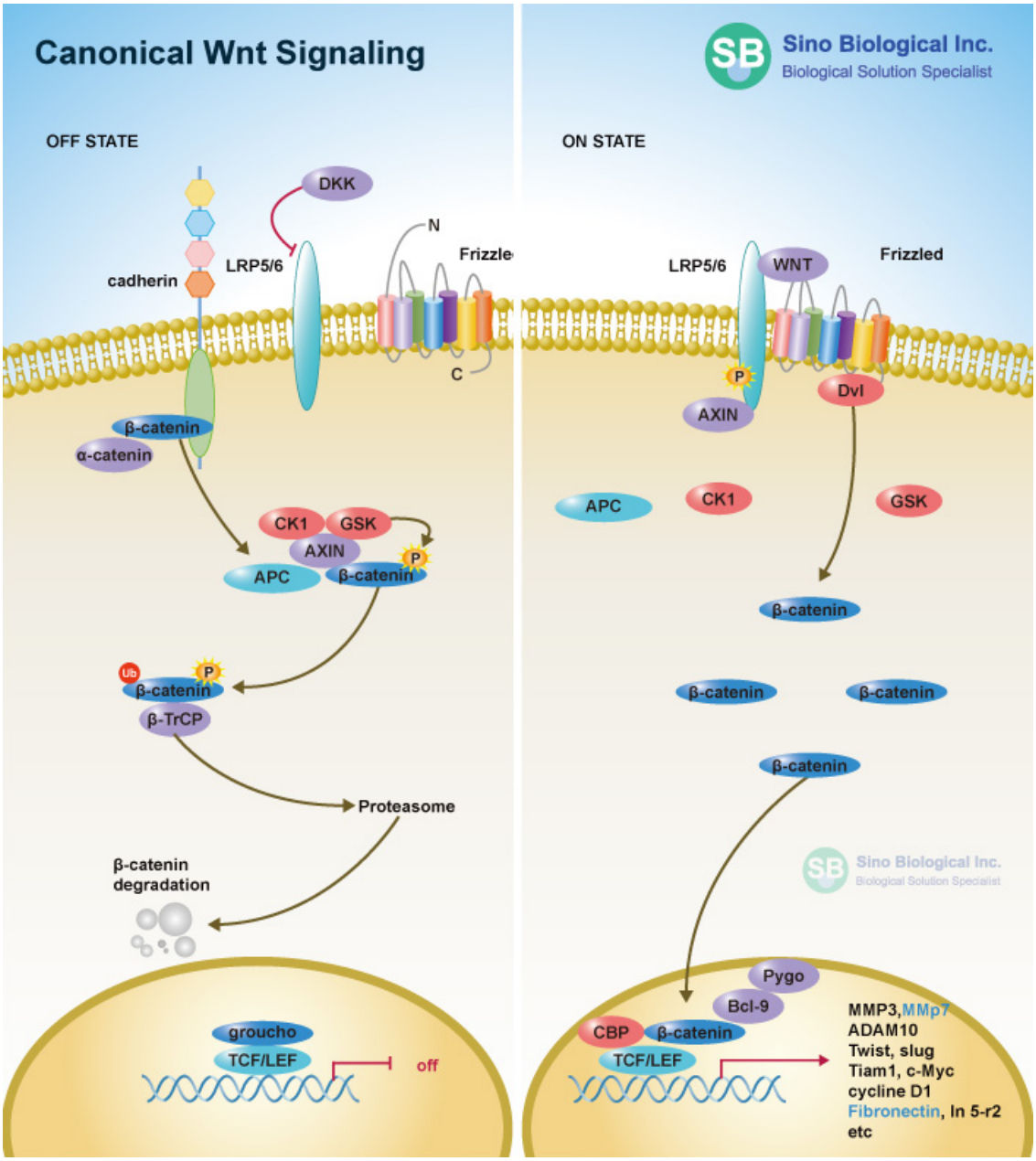

Figure 3.1: N-Cadherin signaling pathway, through the canonical WNT signaling pathway [Sino Biological, Inc.].

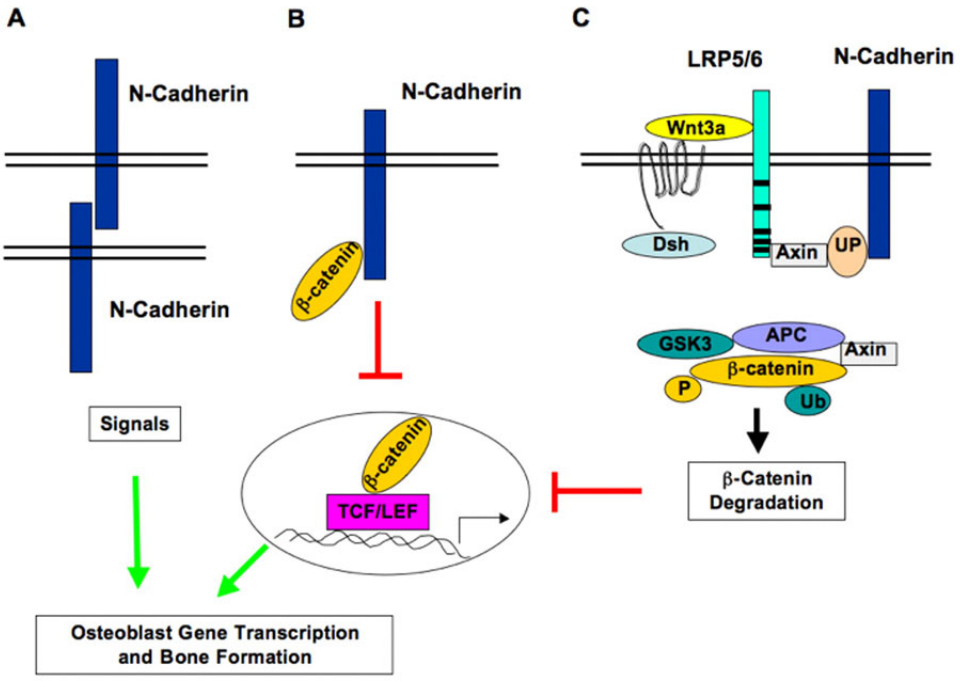

Figure 3.2: N-Cadherin osteoblastic differentiation signaling pathway. [Marie 2009]

Following drying, the beds were divided into 2.5 g aliquots. These aliquots were placed in custom milled 8 mm mold and compressed at 500 psi. During compression, the molds were heated to 130 ^{0}C, and held at constant pressure and temperature for 30 minutes. Following this process, the compressed PLLA was punched from the mold. Using a diamond saw (Model 650, South Bay Technology, Inc.), the rods were cut into 2.3 mm thick disks. The disks were placed in deionized water under agitation for 48 hours to leach out the NaCl, with DI water replaced twice daily. Following the leaching process, scaffolds were placed under vacuum to dry for 24 hours. The resulting scaffolds were 2.3 mm thick, 8 mm diameter, and ∼85% porous.

3.2.3 N-Cadherin Functionalization

Surface modification of the films began with pure PLLA films. Films were rinsed with phosphate-buffered saline (PBS) then incubated in 1 mL of 70% acetone in water for 1 h with moderate shaking, with scaffolds being incubated in 2 mL. The acetone mixture was then aspirated and films were incubated in 1 mL of DMSO with 0.2 mg/mL small MW amine-terminated PLLA for 12 h again with moderate shaking, and scaffolds in 2 mL. After that, films and scaffolds were again rinsed with PBS and left to vacuum dry for 24 h.

Following surface amine termination modification, amine-amine mediated functionalization was completed through the chemical linking of N-succinimidyl 3-(2-pyridyldithio) propionate (SPDP) (Thermo Scientific) and human n-cadherin (Sino Biological) to the surface. Films were rinsed with PBS then incubated at 25 ^{o}C on a shaker in 1 mL of 0.04 mmol/mL SPDP in DMSO diluted with PBS to 0.01 mmol/mL SPDP with a pH of 7.4 for 30 min, and scaffolds were

incubated in 2 mL. SPDP solution was aspirated and scaffolds were incubated at 25^{o}C in 2 mL of 2.5 mg/mL n-cadherin in PBS with a pH of 7.4 for 30 min, with films being incubated in 600 600 μL. Scaffolds and films were then rinsed with PBS and left to vacuum dry for 24 hours before chemical sterilization.

Carboxyl-amine mediated functionalization was completed through EDC carbodiimide crosslinker (Thermofisher Scientific) and human n-cadherin (Sino Biological) to the surface. Briely, n-cadherin was incubated in an activation buffer at a concentration of 1 mg/mL at 25 ^{o}C. Activation buffer consists of 0.1M MES and 0.5M NaCl in PBS at a pH of 6.0. Following this, 0.4 mg EDC ($\sim$2mM) and 0.6mg of NHS were added to the solution and allowed to react for 15 minutes at 25 ^{o}C. Finally scaffolds were incubated in 2 mL of this solution (films in 600 μL) for 2 hours at 25 ^{o}C to facilitate complete reaction. Scaffolds and films were then rinsed with PBS and left to vacuum dry for 24 hours before chemical sterilization.

3.2.4 Cell Expansion and Seeding

Adult mesenchymal stem cells were extracted from the tibias and femurs of male Wistar rats (Harlan Laboratories) using methods identified in previous publications [15, 1]). Cells were cultured at 37 ^{o}C, and 5% CO_2 in standard α-MEM (Invitrogen) supplemented with 10% fetal bovine serum (Atlanta Biologicals) and 1% antibiotic-antimycotic (Invitrogen). Passage 2 cells were used for this study at a density of 2 million cells/mL for scaffold seeding.

PC3 prostate cells, B16 melanoma cells, and MDA breast cancer cells (ATCC) were cultured in T75 culture flasks using manufacturer recommended culture medium. PC3 and B16 cells were cultured in RPMI and MDA cells

were cultured in L-15. Cells were cultured until reaching 70% confluency, and then were lifted and suspended at a density of 1 million cells/mL for scaffold seeding.

We prepped the scaffolds for cell seeding using an established pre-wetting technique [2]. Vacuum air removal of scaffolds was conducted in 75% ethanol. Pre-wet scaffolds were placed in cassettes within a flow perfusion bioreactor for a one hour in α-MEM to remove any remaining ethanol [10, 4]. Following the flush, 1 million MSCs, PC3s, B16s, or MDAs in 150 μL of media were pipetted in each each scaffold chamber. The seeding mixture was dynamically perfused at 0.15 mL/min, forwards and backwards, in five minute intervals for two hours. After oscillatory seeding, the bioreactor was allowed to rest for two hours, without flow, to facilitate cell attachment. Finally, the appropriate media was continuously perfused at a rate of 0.5 mL/min/scaffold.

3.2.5 Construct Cellularity

The number of cells present in each construct was evaluated using fluorescent PicoGreen dsDNA assay (Invitrogen). At each sacrificial time point, the construct was removed from the cassette and dunked in PBS to remove any cells not adhered to the scaffold. Subsequently, the scaffolds were chopped into eight pieces, placed in 1 mL of DI H_2O, and stored at -20^{o}C. Each construct underwent three freeze/thaw cycles to lyse the cells. After following supplier protocols, solutions were run on a Synergy HT Multi-Mode Microplate Reader (Bio-Tek) at an excitation wavelength of 480 nm and an emission wavelength of 520 nm. All samples and standards were run in triplicate.

3.2.6 Fluorescent Nucleus and Actin Staining

Three scaffolds at each time point were subjected to hoechst and phallacidin staining. This was done to confirm the cellularity result from the above ds-DNA assay as well as to provide information on cell distribution within the scaffold in addition to matrix deposition. Scaffolds were resected from culture, rinsed with PBS, and fixed in solution of 4% formalin in PBS for 15 minutes at 25 ^{o}C. Following this, samples were rinsed in three consecutive PBS washes. They were then permeabilized in a solution of 0.5% PBST (PBS and Triton X-100) for 15 minutes at 25 ^{o}C. Fixed and permeabilized samples were stained using hoechst 33342 and phalloidin (ReadyProbes NucBlue and ActinGreen 488; Thermofisher Scientific) using manufacturer protocols. After incubation, scaffolds were rinsed thoroughly with PBS before imaging on a Nikon Epi-fluorescence microscope. Image analysis was performed with MetaMorph 6.2 (Universal Imaging Corporation) and Image J software packages.

3.2.7 Statistical Analysis

A one-way analysis of variance (ANOVA) was used to compare mean $\pm$ standard deviation of pore and fiber measurements, in which Tukeys Honestly Significant Difference (HSD) test was performed to identify significant differences (p-value < 0.05). One-way ANOVA and Tukeys HSD were used to compare the rest of the results. All statistical analysis was performed using a custom python code utilizing the open source Numpy, matplotlib, and SciPy libraries.

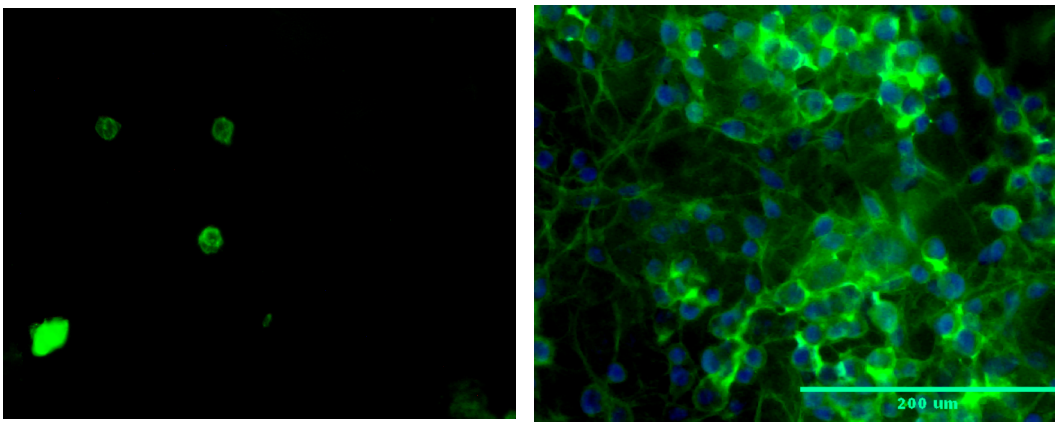

Figure 3.3: Dual staining of fixed B16 cells seeded on PLLA scaffolds with cell nuclei show in blue and actin shown in green. The left image features unmodified PLLA; the right, modified. Stains were completed using hoechst and phallacidin to stain the cell nucleus and actin, respectively.

3.3 Results

3.3.1 Surface Activity

Validation of cell seeding following modification was evaluated on 2D films. Figure 3.3 shows B16 cells seeded on unmodified and modified PLLA films. Clearly, cells seeded on modified surfaces express a higher degree of cell attachment.

3.3.2 Surface Modification Validation

Completion of the modification process was confirmed using through the comparison of cell spreading for plain, a negative control, and a positice control (Figure 3.4). Cell spreading is a measure of the surface area of actin normalized for the number of cells, and is a measure of the strength of cell adhesion. More information for these calculations may be found in the Appendix. For each sample type, six samples were taken (n = 6). Plain samples refer to pure

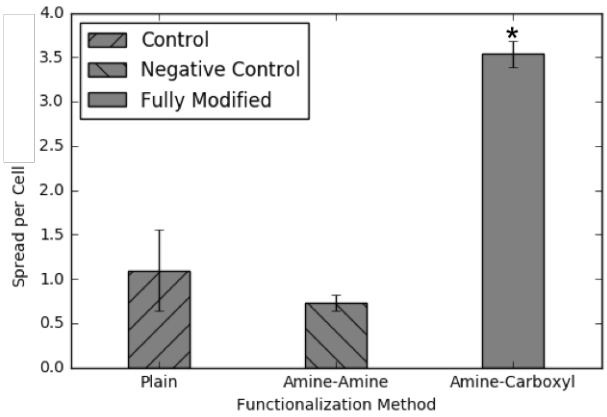

Figure 3.4: Cell spreading, or the actin surface area covered per cell, for B16 cancer cells seeded on: 1) plain nonmodified PLLA films; 2) films modified to express n-cadherin using amine-amine coupling; and 3) films modified to express n-cadhering using amine-carboxyl binding. Cell spreading is an indicator of the extent of cellular adhesion strength. Values are given as the mean $\pm$ standard error of the mean (n = 3). Statistical significance compared to controls is indicated by $*$ ($p < 0.01$).

PLLA scaffolds. Negative control refers to the amine-amine reaction scheme discussed previously. This scheme produced reduced cell adhesion, despite being expected to express the n-cadherin moeity, due to the orientation of n-cadherin which blocks the binding sites the cells utilize. The amine-carboxyl scheme exhibited significatly improved cell adhesion, well over two times compared to non-functionalized scaffolds.

3.3.3 Seeding Efficiency

Figure 3.5 compares the seeding efficiency of cells seeded on non-modified and carboxyl modified scaffolds. Also listed as a comparison are the seeding efficiences for MSCs. It is clear that cancer cells have a highly reduced attachement rate to unmodified PLLA scaffolds, ranging from 5-12%. With this in mind, it is a positive finding that B16 cells seeded on modified scaffolds

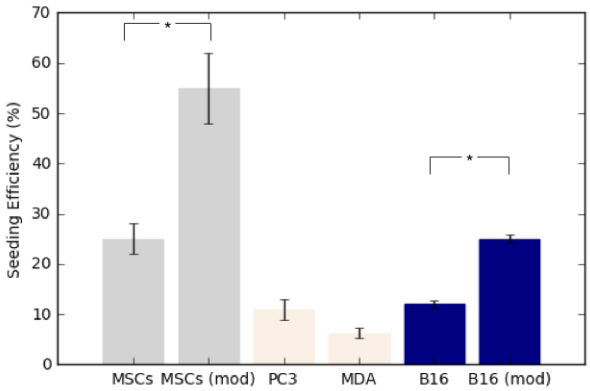

Figure 3.5: Seeding efficiency of various cell types on PLLA scaffolds. (Mod) indicates cells were seeded on scaffolds that have been modified to express RGD using amine-amine coupling (MSCs) or n-cadherin using amine-carboxyl binding (B16). Values are given as the mean ± standard error of the mean (n = 3). Significance is indicated by $*$ ($p < 0.01$), and was calculated via ANOVA with Tukey HSD Post-hoc analysis.

have a seeding efficiency comparable to MSCs on nonmodified scaffolds.

3.4 Discussion

The goal of this study was to compare the seeding efficiency of cancer cells on normal PLLA polymer scaffolds and n-cadherin expressing PLLA scaffolds. Initially, a variety of cells, both MSCs and cancer, were seeded on unmodified and modified 2D PLLA films. The goal of this was to gain a measure of the cell density and cell spreading on the different surfaces. After seeding, cells were fixed, stained, and imaged by fluorescent microscopy. Figure 3.3 shows a pronounced difference in B16 cell density on unmodified and modified films. Modified films show a large amount of cells adhered to the surface of the film and elevated actin stretching, while there are a minimal amount of cells adhered to the unmodified films and minimal actin stretching.

Figure 3.4 quantifies the difference in cellular adhesion on unmodified and modified surfaces. After generating the fluorescent images, surfaces were evaluated for the actin surface area per cell. This value gives a look into the strength of cell binding to the surface, as stronger adhesion will manifest from actin stretching out to attach to a larger surface area. As seen in the graph, cell spreading on the films modified using the amine-carboxyl modification scheme, producing stretching three times the amount of the plain and amine-amine scheme. Additionally, the amine-amine scheme functions as a negative control, as that modification process blocks binding site, preventing cells from adhering. The error present in the plain films highlights the variability exhbited when seeding cancer cells on polymer scaffolds.

Finally, the seeding efficiency for MSCs and cancer cells on both unmodified and modified 3D scaffolds. MSCs were seeded on RGD expressing scaffolds, which we investigated in a previous study. As seen in Figure 3.5, MSCs have a 30% higher adhesion rate to RGD modified scaffolds ($\sim$55%) than plain scaffolds ($\sim$25%). When comparing that result to the adhesion rates of cancer cells, it is evident that there is a large disagreement between the two. Initial seeding efficiencies on plain PLLA scaffolds for PC3s, MDAs, and B16s are about 15% lower than MSCs. MDAs exhibit the lowest adhesion rates, with less than 10% of the intial cells seeded on the scaffolds remaining after incubation. Not only is this a significant detriment in terms of the time required to culture dense tumor *in vitro*, but it also means that an overwhelming majority of cancer cells used for 3D *in vitro* culture will be wasted. Importantly, when seeded on n-cadherin expressing scaffolds, the abysmal seeding effiency of B16s is increased to a comparable rate of MSCs on non-modified scaffolds,

over twice the intial rate. Clearly, the modification scheme presented in this manuscript provides the means to gain workable cancer cell adhesion rates on PLLA scaffolds.

3.5 Conclusion

In this study we sought to leverage our surface modification platform for *in vitro* tumor engineering. In particular, we aimed at increasing cancer cell adhesion rates to poylmer scaffolds. We improved upon past work by modifying scaffolds with n-cadherin, peptide that has been show to mediate cell-to-cell adhesion in metastatic tumors. Following modification, we seeded scaffolds with a variety of cell lines, such as PC3 prostate cancer, MDA breast cancer, and B16 melanoma. Through fluorescent imaging and biochemical assays, we able to validate our hypothesis. Imaging highlighted the disparity in cell adhesion on modified and unmodified scaffolds, with B16s showing elevated cell density in the n-cadherin expressing surfaces. This result was quantified by measuring the cellular spreading on those same groups. Again cells seeded on n-cadherin expressing surfaces displayed elevated levels of adhesion. Lastly, we measured the seeding efficiency of cancer cells on the two groups and compared the results with those from MSCs. By modifying the scaffolds, we were able to increase B16 seeding to rates comparable to MSCs on non modified scaffolds. These findings support the use of our modification scheme to increase the viability of *in vitro* tumor engineered constructs.

3.6 Acknowledgements

I acknowledge the following collaborators: Montana Minnis and Patrick McKernan. I acknowledge support from the Oklahoma Center for the Advancement of Science and Technology (HR13-214), and the Stehpenson Cancer Center. I gratefully acknowledge fellowship funding from the Oklahoma Louis Stokes Alliance for Minority Participation (OK-LSAMP) Bridge to the Doctorate, Cohort 6 (EHR/HRD #1249206). Any opinions, findings and conclusions or recommendations expressed in this material are those of the authors and do not necessarily reflect the views of the National Science Foundation.

References

[1] J. F. Alvarez-Barreto, S. M. Linehan, R. L. Shambaugh, and V. I. Sikavitsas. Flow Perfusion Improves Seeding of Tissue Engineering Scaffolds with Different Architectures. *Annals of Biomedical Engineering*, 35(3):429–442, Feb. 2007.

[2] J. F. Alvarez-Barreto and V. I. Sikavitsas. Improved Mesenchymal Stem Cell Seeding on RGD-Modified Poly(L-lactic acid) Scaffolds using Flow Perfusion. *Macromolecular Bioscience*, 7(5):579–588, May 2007.

[3] Antonios G. Mikos. Preparation and characterization of poly(L-lactic acid) foams.pdf. *Polymer*, 1994.

[4] G. N. Bancroft, V. I. Sikavitsas, J. Van Den Dolder, T. L. Sheffield, C. G. Ambrose, J. A. Jansen, and A. G. Mikos. Fluid flow increases mineralized matrix deposition in 3d perfusion culture of marrow stromal osteoblasts in a dose-dependent manner. *Proceedings of the National Academy of Sciences*, 99(20):12600–12605, 2002.

[5] L. J. Bray and C. Werner. Evaluation of Three-Dimensional *in Vitro* Models to Study Tumor Angiogenesis. *ACS Biomaterials Science & Engineering*, May 2017.

[6] B. Delalat, F. Harding, B. Gundsambuu, E. M. De-Juan-Pardo, F. M. Wunner, M.-L. Wille, M. Jasieniak, K. A. Malatesta, H. J. Griesser, A. Simula, D. W. Hutmacher, N. H. Voelcker, and S. C. Barry. 3d printed

lattices as an activation and expansion platform for T cell therapy. *Biomaterials*, 140:58–68, Sept. 2017.

[7] C. Hirt, A. Papadimitropoulos, M. G. Muraro, V. Mele, E. Panopoulos, E. Cremonesi, R. Ivanek, E. Schultz-Thater, R. A. Droeser, C. Mengus, M. Heberer, D. Oertli, G. Iezzi, P. Zajac, S. Eppenberger-Castori, L. Tornillo, L. Terracciano, I. Martin, and G. C. Spagnoli. Bioreactor-engineered cancer tissue-like structures mimic phenotypes, gene expression profiles and drug resistance patterns observed in vivo. *Biomaterials*, 62:138–146, Sept. 2015.

[8] J. B. Kim. Three-dimensional tissue culture models in cancer biology. *Seminars in Cancer Biology*, 15(5):365–377, Oct. 2005.

[9] A. Malandrino, R. D. Kamm, and E. Moeendarbary. In Vitro Modeling of Mechanics in Cancer Metastasis. *ACS Biomaterials Science & Engineering*, June 2017.

[10] Mikos. Flow perfusion culture of mesenchymal stem cells for bone tissue engineering. *StemBook*, 2008.

[11] A. Nyga, U. Cheema, and M. Loizidou. 3d tumour models: novel in vitro approaches to cancer studies. *Journal of Cell Communication and Signaling*, 5(3):239–248, Aug. 2011.

[12] J. W. Park and S. S. Im. Miscibility and morphology in blends of poly(l-lactic acid) and poly(vinyl acetate-co-vinyl alcohol). *Polymer*, 44(15):4341–4354, July 2003.

[13] N. Peela, D. Truong, H. Saini, H. Chu, S. Mashaghi, S. L. Ham, S. Singh, H. Tavana, B. Mosadegh, and M. Nikkhah. Advanced biomaterials and microengineering technologies to recapitulate the stepwise process of cancer metastasis. *Biomaterials*, 133:176–207, July 2017.

[14] A. M. Sitarski, H. Fairfield, C. Falank, and M. R. Reagan. 3d Tissue Engineered in Vitro Models of Cancer in Bone. *ACS Biomaterials Science & Engineering*, July 2017.

[15] S. B. VanGordon. Three-dimensional bone tissue engineering strategies using polymeric scaffolds. *The University of Oklahoma. Dissertation*, 2012.

[16] S. B. VanGordon, R. S. Voronov, T. B. Blue, R. L. Shambaugh, D. V. Papavassiliou, and V. I. Sikavitsas. Effects of Scaffold Architecture on Preosteoblastic Cultures under Continuous Fluid Shear. *Industrial & Engineering Chemistry Research*, 50(2):620–629, Jan. 2011.

Chapter 4

On the Effects of 3D Printed Scaffold Architectures on Flow-Induced Shear Stress Distributions

Abstract

As 3D printing gains more exposure as the future of scaffold fabrication for tissue engineering, the ability to preemptively model the constructs microenvironment becomes of vital importance. Particularly when using perfusion based bioreactor systems for bone tissue engineering applications, the most important properties to obtain are the fluid flow and wall shear fields that potential cells will experience during and after seeding. Traditionally, 3D printing has given users the impression that the scaffold obtained after printing will exhibit

the same, or closely similar, architecture as the designed model. While this may be the case in terms of the macrostructure, we hypothesized that the local fluid dynamic environment would differ greatly. The intention of this study was to 3D print scaffolds of various pore size gradients, image these constructs utilizing micro-computed tomography, and perform computational fluid dynamic simulations on the resulting reconstructions and the initial designs in order to compare the average shear on the fibers, where the cells would be adhered. As a determining factor, the probability density function (p.d.f.) of each was compared to not only highlight the major differences, but also to show the reproducibility of the printing process. The results presented in this manuscript give users the knowledge of how the 3D printing process may alter the intended fluid environment they designed, and how to, in spite of that fact, produce repeatable results.

4.1 Introduction

Tissue engineering seeks to repair tissue damage associated with acute trauma or surgery [14]. Bone tissue engineering in particular aims to alleviate the problems of low graft supply and donor site morbidity, commonly attributed to autologous bone transplants from one region of the body to another. A simple approach consists of harvesting patient stem cells, seeding them on three dimensional scaffolds, and culturing them in a bioreactor. Once properly developed, the tissue matrix is reinserted at the location requiring tissue

This study was completed thanks to the collaborations listed in the acknowledgments. Listed here are the author contributions: CW performed image analysis; performed reconstructions and flow simulations; performed data analysis; and wrote the manuscript. GM performed microcomputed tomography imaging. JET and MS performed scaffold characterization. CMP fabricated scaffolds.

repair, providing both material to provide support and cells optimized to mend the damaged tissue. By developing *in vitro* tissue culture techniques, tissue engineered bone will one day be able to be used during graft surgeries. For this proposed therapy to work, however, it is of utmost importance to produce consistent grafts during every culture.

For engineered bone, both the choice of scaffold used to support cells in culture and the bioreactor used to provide mechanical stimulation play significant roles in cell viability and *ex vivo* tissue development. Scaffold properties, such as pore size and porosity, must be manipulated to match desirable tissue properties. In order to bring up repeatable scaffolding conditions in every culture, 3D printing has emerged as the premier fabrication method for tissue engineering [7, 18, 6, 19]. It allows for the reproducible manufacturing of scaffolds with near limitless geometries. Additionally, a wide range of materials may be used during production, such as synthetic polymers like poly(l-lactic acid) and poly(propylene fumarate) or natural materials such as collagen or silk. Poly(propylene fumarate) (PPF) is a widely used material for bone tissue engineering due to its compatibility with the osteoblastic cells [8, 1, 5, 7, 10, 11, 12], mechanical properties [13, 23], and its compatibility with extrusion-based 3D printing [9]. In addition to providing a suitable material for bone tissue engineering, the combination of this polymer with extrusion-based printing has enabled the fabrication of scaffolds with controlled pore sizes. The ability to regulate the pore size within each layer of a scaffold will allow researchers to tailor scaffold geometries to give the most beneficial flow environment [9, 18].

Previous studies combining flow perfusion experiments with computational

fluid dynamic simulations have shown that shear stresses below 15 dynes/cm^2 are conducive to increased matrix production and osteoblastic differentiation. Additionally, elevated shear stresses may cause increased cell detachment. Due to this, it is important to properly model and evaluate the flow profile inside cell-seeded scaffolds. Ideally, the localized shear rates would be anticipated in order to give proper fluid control. To this end, 3D printing has been investigated as a method to fabricate reproducible architectures, and, in turn, reproducible flow fields.

In this study, we have utilized extrusion based 3D printing to fabricate scaffolds that exhibit varying pore sizes and/or varying pore size gradients. These varying conditions were chosen in an attempt to control the shear environments experienced by cells under flow perfusion. The resulting constructs were imaged utilizing μCT, segmented, and reconstructed following previously published techniques [21, 22, 16]. This flowpath allows for subsequent computational fluid dynamic (CFD) simulations on the printed scaffolds that may then be compared to the initial designs.

In this manuscript, we hypothesized that the levels of fluid shear present at the walls of a 3D printed scaffold will vary greatly from the anticipated shear on the designed computer aided design (CAD) file (in the STL file format). In particular, it is not a valid assumption that 1) the shear field predicted in the CAD design will directly translate to the printed scaffold and 2) that the probability density functions (p.d.f.) will be fully described by the same relationships. The intention of this study is to use CFD simulations to expose the aforementioned differences and bring to light relationships between CAD designs and the resulting reconstructions, which would give researchers

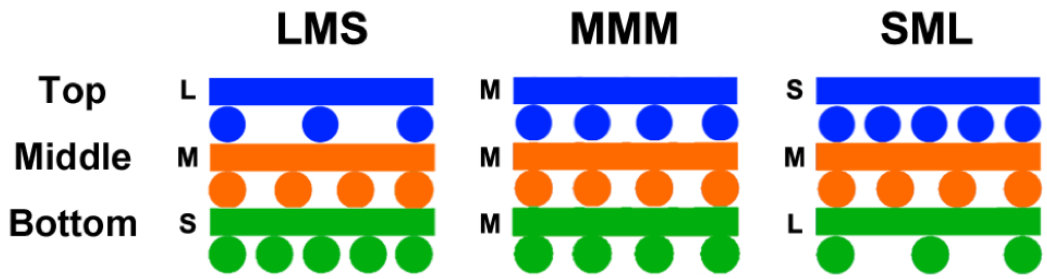

Figure 4.1: Cross-sectional view of gradient scaffold orientations with the following pore sizes: large (L) = 1 mm, medium (M) = 0.6 mm, small (S) = 0.2 mm. Image taken from previous publication [19].

the ability to anticipate the flow environment within a construct before the printing process.

4.2 Materials & Methods

4.2.1 Scaffold Design

PPF (Mn, 2280 ± 23 Da; PDI, 1.72 ± 0.02) scaffolds were fabricated by stacking individual 3D printed layers of large (L), medium (M), or small (S) pore sizes, Figure 4.1, using a step-growth polymerization reaction [5, 8, 1]. The PPF printing solution was prepared using protocols described in a previous study [18]. Briefly, PPF was mixed with diethyl fumarate (DEF, Sigma, St. Louis, MO) in an 85:15 wt% ratio. First, a photoinitiator, phenylbis(2,4,6-trimethylbenzoyl)-phosphine oxide (BAPO, BASF, Florham Park, NJ), was dissolved in DEF (with 1 wt% BAPO) by vortexing and was mixed with warm PPF (∼70 ^{o}C) to permit UV crosslinking.

Layers of dimensions 10x10x0.54mm were drawn (SolidWorks, Waltham, MA), sliced (Bioplotter RP, EnvisionTEC, Gladbeck, Germany), and printed

at the following conditions: extruder temperature (55 ^{o}C), platform temperature (5 ^{o}C), print head speed (5 mm/s), needle offset (0.25 mm), and syringe tip diameter (0.34 mm). Pore sizes ranged from 0.2 mm (small, S), 0.6 mm (medium, M), and 1 mm (large, L). Following printing, printed layers underwent UV crosslinking (single projection, 10s exposure, 70 mm height) following established methods [18]. Fiber diameter and pore sizes were validated following stereomicrscopy imaging (MZ6, Leica Microsystems, Wetzlar, Germany) (n = 12 scaffolds per group, 5 measurements per image) (ImageJ, NIH).

4.2.2 Porosity Measurements

Porosity was quantified (n = 12 per group) using gravimetric analysis following previous methods [[17, 3, 20]. Briefly, sample dimensions (length, L; width, W; thickness, T) and weight w_*material* were measured and used to calculate the porosity according to Equation 1, where $\rho_{scaffold}$ is the scaffold density and $\rho_{material}$ is the density of the material. The respective densities of PPF (1.267 g/mL) [16], DEF (1.052 g/mL) (Sigma), and BAPO (1.19 g/mL) (BASF) were used to estimate $\rho_{material}$.

$$\epsilon = 1 - \frac{\rho_{scaffold}}{\rho_{material}} = 1 - \frac{w_{scaffold}}{LWT\rho_{material}} \tag{4.1}$$

4.2.3 Cell Expansion, Seeding, and Culture

The human Ewing sarcoma (ES) TC71 cells (MD Anderson Medical Center) were cultured in Roswell Park Memorial Institute (RPMI) medium 1640 (Mediatech) supplemented with 10% FBS (Gemini) and antibiotics/antimycotic (100 IU/mL penicillin and 100 μg/mL streptomycin; Gibco) until reaching 85% con-

fluency. RPMI medium 1640 was supplemented with 10% FBS (Gemini Bio-products) and antibiotics (100 IU/mL penicillin and 100 μg/mL streptomycin; Gibco). After reaching confluency, cells were lifted with 0.05% trypsin-EDTA (Gibco), and counted with a hemocytometer.

3D printed scaffolds were sterilized in a 24 hour ethylene oxide cycle (Anderson Sterilizers) and allowed to de-gas for 12 hours prior to cell culture. Scaffolds were pre-wet in 75% ethanol using the methods described in previous publications[2]. In an attempt to increase cell attachment, pre-wet scaffolds were incubated on a rotating shaker overnight in 1 mL complete medium. Each scaffold was seeded with 200,000 cells/mL RPMI and allowed to adhere, overnight, on a rotating table in an incubator. Constructs were cultured for up to 16 days at a flowrate of 0.1 mL/min.

4.2.4 Imaging and Reconstruction

The scaffolds were scanned non-destructively with micro-computed tomography (μCT) using a commercial system to obtain 2D image slices (Quantum FX, Perkin Elmer, Waltham, MA; L10101, Hamamatsu Photonics, Japan; PaxScan 1313, Varian Medical Systems, Palo Alto, CA). The images were then filtered, thresholded, and stacked using the open-source visualization software 3D Slicer (slicer.org) to form the 3D reconstructions. Before concluding each reconstruction, the porosity was measured and matched to that of the printed scaffold in order to assure a proper segmentation. This method has proven successful for previous studies [21, 22, 16] For each scaffold, slices were cut off from the edges of the reconstruction to avoid end effects in the computational fluid dynamic (CFD) simulations. The exact size of the resulting digital

scaffold was different for each case; however, the typical size for each reconstruction was approximately 10 x 10 x 1.2 mm (length x width x height). For this study, we investigated a total of 12 different sets of reconstructions.

4.2.5 Computational Simulations

Simulations were performed using Fluent 16.2 (ANSYS, Inc.), which has been extensively utilized for computed surface shear stresses on μCT reconstructions [21, 22, 16, 15]. A simulation domain was implemented that cooresponded to the bioreactor cassette of the length and width specified in the previous section. Fluid flow conducted with flat velocity profiles at the inlets based on a flow rate of 0.1 mL/min, no-slip boundary conditions imposed at the walls of the domain, and also an outlet with constant static pressure [16]. The culture medium was modeled as an incompressible Newtonian fluid with a dynamic viscosity of 1 cP, according to previous studies [21, 16]. In order to avoid any unwanted entrance effects and allow for fully developed laminar flow, we added a 4.8 mm long inlet channel in front of the scaffolds, which satisfies the conditions for laminar flow in a non-circular pipe [4]. Hydraulic radius (Dh), cross-sectional area (A), perimeter of the channel (m^2), Reynolds number (Re), average velocity (v), medium density (ρ), medium viscosity (μ), and entrance length (EL) and are defined in Equation 2-Equation 4:

$$D_h = \frac{4A}{P} = 10mm \tag{4.2}$$

$$Re = \frac{2D_h\langle v\rangle\rho}{\mu} << 1 \tag{4.3}$$

$$EL = 0.035ReD_h << 4.8mm \tag{4.4}$$

Scaffolds were meshed using approximately 950,000 grid cells with a size of 7 μm. Polyhedral element geometries were used for the scaffolds themselves, while tetrahedrals were used on the domain walls and the exit side of the scaffold to minimize computational time. The goal of this study is to evaluate the shear at the fluid-scaffold wall interface, therefore only wall shear values at these surface nodes were included in calculations. Additionally, shear distributions were plotted using 1,000 equally sized bins. It must be noted that wall shear stress as indicated in this chapter includes both the shear and normal stress on the walls of the scaffold.

4.2.6 Probability Density Functions

In a previous study [22], it was found that the normalized flow induced shear stresses in highly porous nonwoven fiber mesh scaffolds (85% and above) follow a three-point gamma distribution, Γ(2.91, -1.43, 0.45), defined in Equation 5-6:

$$f(\tau_w^*) = \frac{(\tau_w^* - \gamma)^{\alpha-1}}{\beta^\alpha \Gamma(\alpha)} exp\left\{\frac{-(\tau_w^* - \gamma)}{\beta}\right\} \tag{4.5}$$

$$\tau_w^* = \frac{\tau_w - \bar{\tau}_w}{\sigma} \tag{4.6}$$

where α = shape, β = scale, and γ = location. Additionally, the work was expanded to describe other scaffold types when only τ is known by using a standard gamma distribution ($\gamma = 0$) with parameters $\alpha = 2.91$ and $\beta = 0.315\tau_w$ [15]. Furthermore, this study was followed by another manuscript

which validated this distribution for structured scaffolds. All p.d.f.s where fit and plotted using a custom python code utilizing the open source Numpy, matplotlib, and SciPy libraries.

4.2.7 Statistical Analysis

A one-way analysis of variance (ANOVA) was used to compare mean ± standard deviation of pore and fiber measurements, in which Tukeys Honestly Significant Difference (HSD) test was performed to identify significant differences (p-value < 0.05). One-way ANOVA and Tukeys HSD were used to 1) compare top, middle, and bottom layers within each gradient orientation (LMS, MMM, SML) and 2) compare all top (middle, and bottom) layers across gradient orientations. In order to compare results within specific scaffold layers across culture conditions (eg. LMS = top layer under static vs flow perfusion), pairwise comparisons were made using Students t-test ($p < 0.05$). All statistical analysis was performed using a custom python code utilizing the open source Numpy, matplotlib, and SciPy libraries.

4.3 Results

4.3.1 Shear Stress Distributions per Scaffold Layer

We compared the magnitude of the wall shear stress in each layer of the 3D printed PPF scaffolds (Figure 4.2) for both the stereolithography (STL) CAD models of the scaffolds (generated to communicate the scaffold pattern to the 3D printer) and the 3D printed scaffolds, which were analyzed via μCT to generate a 3D reconstruction. For a flow rate of 0.6 mL/min, we observed

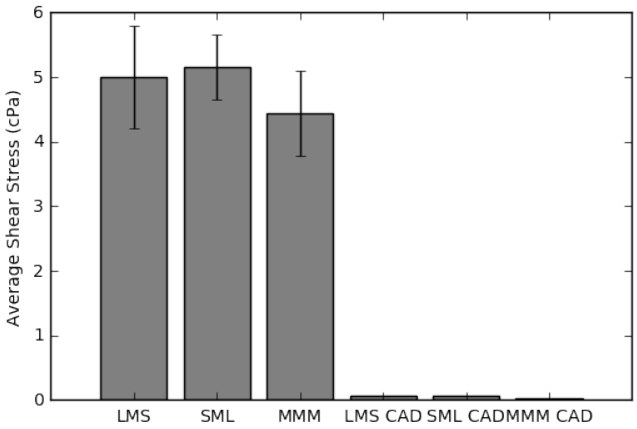

Figure 4.2: Summary of average shear stress for 0.1 mL/min flow rate, comparing computer aided design (CAD) model to scaffold (μCT reconstruction). FLUENT simulations were run either on the reconstructed scaffold or the original CAD model used to print said scaffolds. Values are given as the mean $\pm$ standard error of the mean (n = 4).

a dramatic difference in magnitude between the STL files and the μCT reconstructions (an increase by a factor of 10-100 for all groups). The shear stress magnitude in the gradient configurations (SML, LMS) appeared to be greater than in the uniform scaffold configuration (MMM). Supplemental Figures 4.10 - 4.12 represent computational models of average wall shear stress within the STL file layers and scaffold layers for respective SML, MMM, and LMS configurations.

4.3.2 Shear Stress Distributions per Construct

Additionally, we compared the average overall shear stress in each of the scaffold types, MMM, SML, and LMS for both STL models and the reconstructions. As shown in Figure 4.3, it is clear that there is a pronounced difference between the shear values seen in the models versus the printed scaffolds. This result is supported in Figure 4.4, which shows the wall shear distributions per

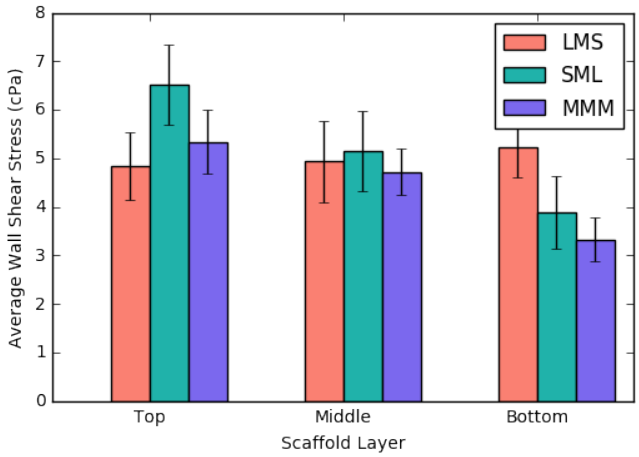

Figure 4.3: Summary of average shear stress per layer for 0.1 mL/min flow rate, comparing LMS, SML, and MMM scaffold architecture (μCT reconstructions). Pore sizes ranged from 0.2 mm (small, S), 0.6 mm (medium, M), and 1 mm (large, L). Values are given as the mean $\pm$ standard error of the mean (n = 4).

construct on reconstructed scaffolds and CAD designs. For a given number of node points on the walls of the scaffolds, these graphs give the number of times (frequency) a certain shear stress value is expressed. In terms of the reconstructions, scaffolds that contain the same porosity seem to experience the same average shear stress, which is consistent with previous findings. Figure 4.5 shows the distributions in the top layer for each gradient orientation.

4.3.3 Effects of Printing Defects on Shear Stress Levels

Figures 4.6 and 4.7 show lateral sections of reconstructed scaffold, with wall shear stress overlaid on top. It is evident that there are high levels of shear stress are located around defects created during the 3D printing process, as indicated by the black arrow. Additionally, Figure 4.8 shows an SEM micrograpgh of cells seeded on the same construct. These cells are present in the

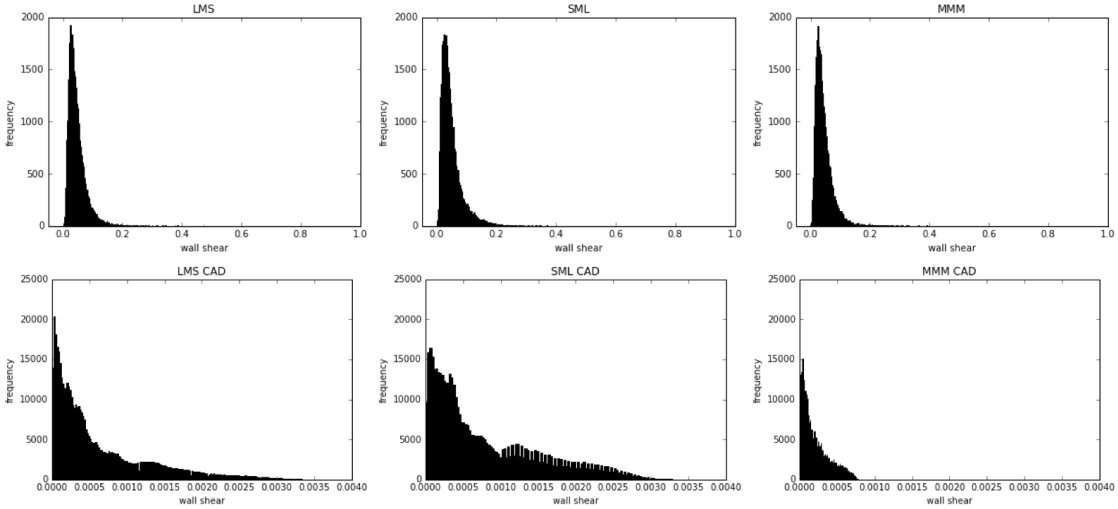

Figure 4.4: Wall shear stress distributions [cPa] based on gradient orientation (LMS, MMM, and SML) and scaffold type (reconstruction or CAD). Pore sizes ranged from 0.2 mm (small, S), 0.6 mm (medium, M), and 1 mm (large, L). FLUENT simulations were run either on the reconstructed scaffold or the original CAD model used to print said scaffolds.

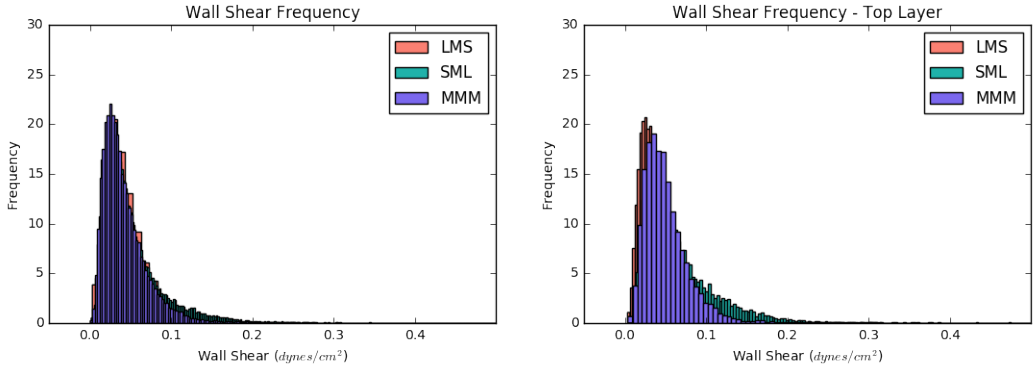

Figure 4.5: Wall shear stress distributions [cPa] based on gradient orientation (LMS, MMM, and SML) for reconstructions. The left image compares the distributions for the entire scaffolds, whereas the right image compares the disributions in the top layers.

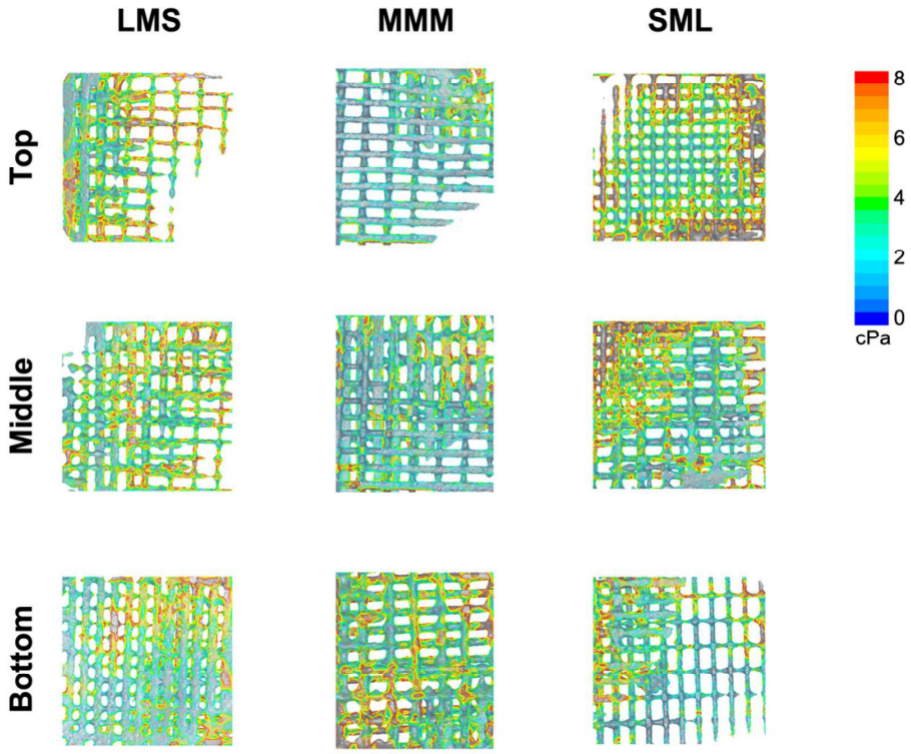

Figure 4.6: Top view of 3D printed scaffold layers. Average wall shear stress per layer (top, middle, and bottom) for all gradient orientations (LMS, MMM, and SML). Wall shear stress is mapped as a color distribution (heat map) on the top surface of each layer.

interior of the scaffold, cooresponding to the areas of low shear in the previous figure.

4.3.4 Probability Density Function

Figure 4.9 also displays the probability density functions for the various scaffold subsets along with the standard gamma distribution fit. Indeed, the reconstructions all display close agreement to the fit, within statistically acceptable bounds.

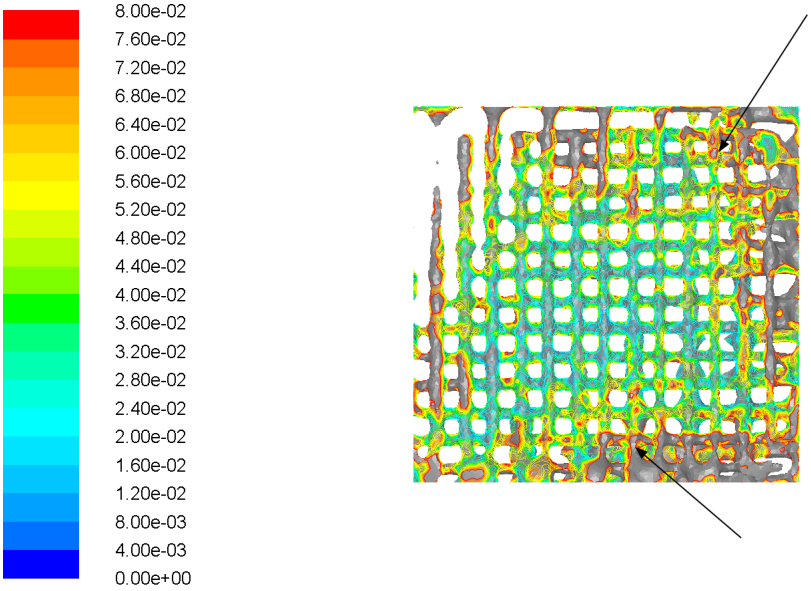

Figure 4.7: Top view of scaffold layer. Wall shear stress is mapped as a color distribution (heat map) on the top surface of each layer. Heat map indicates distribution of high (red, 8 cPa) to low (blue, 0 cPa) shear stresses. Heat map legend applies to all layers. Black arrows are indicating defects. Defects can manifest as uneven printed layers, fibers that have joined together, or clogged/misshapen pores.

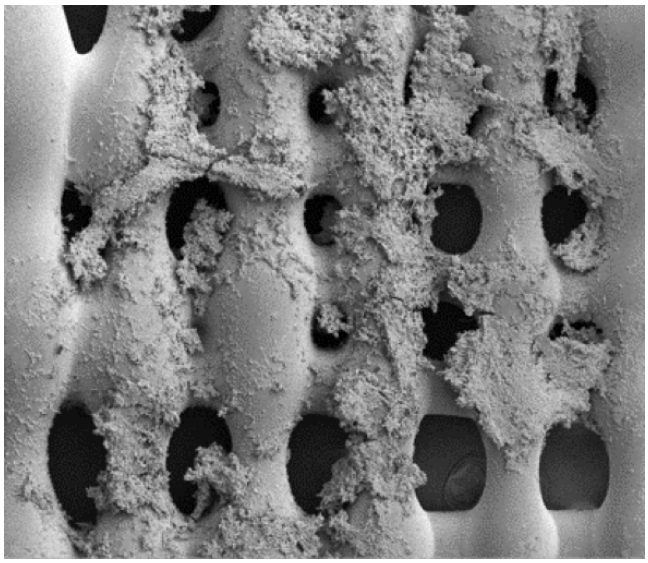

Figure 4.8: Top view of SEM micrograph of scaffold layer. Cells are aggregated in the interior of the scaffold consistent with area of low fluid shear stress indicated in Figure 4.7.

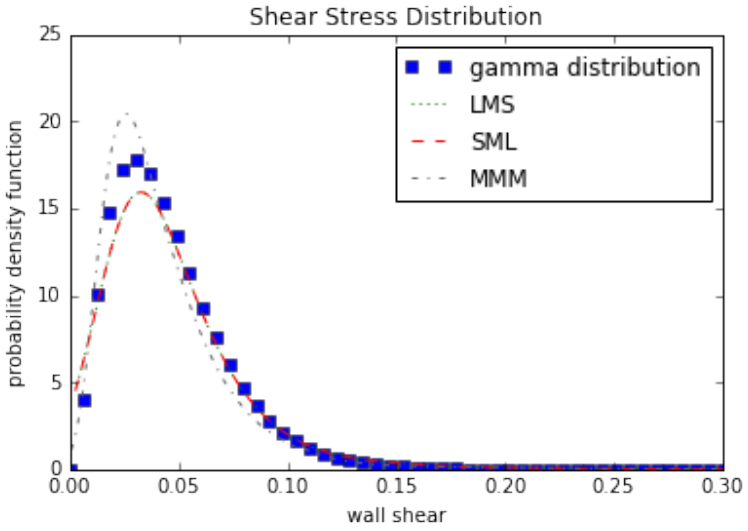

Figure 4.9: Probability density functions for each gradient scaffold (LMS, SML, and MMM) and the standard gamma distribution. P.D.F. for the LMS gradient scaffold is shown; however, very closely matched by that of the SML gradient scaffold.

4.4 Discussion

After generating shear stress profiles under several flow rates (up to 6 mL/min tested), the flow rate was adjusted to 0.6 mL/min to achieve physiologically relevant shear stresses within scaffold layers based on previous work [7]. We compared the average wall shear stress in each layer of the 3D printed PPF scaffolds (Figure 4.2), which were scanned via μCT to generate a 3D reconstruction. Computational modeling indicated that the average shear stress was higher in the top layer compared to the middle and bottom layers for both the SML and MMM orientations, while no statistical significance was found among layers in the LMS configuration. This study was also performed on the CAD designs of the scaffolds. Once again, the highest shear stress levels were found at the top layer of the scaffolds towards the flow inlet. We believe this difference is due to the smaller sized pores at the top of the MMM and

SML scaffolds, whereas the LMS scaffolds have large pore diameters at the top, offering less resistance to inlet flow.

When comparing the results between the reconstructions and CAD designs, it is evident that there is a large disagreement between the two. Not only is significant difference in the overall average shear stress found in the two types, but there are also differences in the radial directions. Particularly, the shear fields found in the CAD designs are consistent from the interior of a layer out to the periphery, whereas the shear fields found in the reconstructions to not express this same characteristic. This is compounded by the high shear stress values found localized around defects in the printed scaffolds, as shown in Figure 4.7. Clearly, these defects have a significant part in altering the flow environment within the constructs resulting in flow being preferential distributed to areas of low resistance. Furthermore, we believe the differences observed may also be due to the surface roughness of the printed scaffolds due to the fact that a CAD design has a smoothness that cannot be replicated in a printed scaffold without significant post-processing. Additionally, previous studies have shown that a smooth surface on a scaffold is not preferable for cellular adhesion; therefore, in terms of scaffolds for cell and tissue growth, there will always be this disparity. Also of note, cells were imaged in loocations that coorespond to areas of low fluid shear, approximately below 3 dynes/cm^2.

On a per construct basis, the average wall shear stresses were compared. Consistent with previous findings for randomly oriented scaffolds, we found that constructs having the same porosities will display not only the same average shear values, but will also have the same distribution of shear induced stress on the construct as a whole. This phenomenon holds true for both the

CAD designs and the reconstructions, as LMS and SML orientations presented statistically identical shear distributions.

Finally, the probability density functions were compared for all groups. A standard gamma distribution fit, $\Gamma(2.91,0,0.315)$, was found that describes the results for all of the reconstructions and is within statistically acceptable bounds [22, 15]. As we hypothesized, this distribution is not statistically acceptable for describing the CAD designs. In other words, the differences found between the reconstructions and the idealized designs are not simply three orders of magnitude apart, but exhibit wildly different fluid environments that cannot be easily dismissed or predicted. This means it is necessary to run fluid dynamic simulations on the actual printed scaffolds in order to obtain any insight into both the viability of a design and the environment the cells will experience.

4.5 Conclusion

In the presented manuscript, we hypothesized that the levels of fluid shear present at the walls of a 3D printed scaffold will vary greatly from the anticipated shear on the designed CAD file. In order to accomplish this, 3D printing was used to fabricate scaffolds that exhibited varying pore sizes and/or pore size gradients. These constructs were then imaged using μCT and reconstructed to allow for CFD simulations to be performed. Average shear stress values, both per layer and per construct, were compared, and confirmed major differences between the idealized model and reconstructions.

An important finding was that when the orientation consists of large pores at the inlet leading to the pores, the average shear stress is consitent through-

out the scaffold due to the fluid being funneled into the next layer. The opposite is found with the small to large orientations, where the fluid experiences the largest magnitude at the inlet. In a few instances, localized regions of higher shear stress were observed near the edges (eg. SML top layer) and near defects within the 3D printed scaffolds (eg. MMM middle layer). To accompany these findings, p.d.f.s of the wall shear stress for the resulting reconstructions and the initial designs were compared, highlighting confirming the disparities between the two. Finally, we proved that a previously identified standard gamma distribution describes the p.d.f. of flow induced stresses in the reconstructions. Statistically, however, this distribution does not describe those of the CAD designs within acceptable limits. In conclusion, researchers should never rely on intuition alone, due to the complexity of the fluid-scaffold interactions, and computational modeling should be utilized whenever possible.

4.6 Acknowledgements

I acknowledge the following collaborators: Ghani Muhammad, Jordan E. Trachtenberg, Marco Santoro, Charlotte M. Piard, John P. Fisher, Antonios G. Mikos, and Hong Liu. JET and MS acknowledge support from support from the National Institutes of Health for work in the areas of bone and cartilage tissue engineering (R01 CA180279 and R01 AR068073), as well as from the Armed Forces Institute of Regenerative Medicine (W81XWH-14-2-0004) (to A.G.M). J.P.F. also acknowledges the NIH (R01 AR061460) for funding the Bioplotter printing system. J.E.T. acknowledges funding from the National Science Foundation and the Howard Hughes Medical Institute Graduate Re-

search Fellowships. I gratefully acknowledge fellowship funding from the Oklahoma Louis Stokes Alliance for Minority Participation (OK-LSAMP) Bridge to the Doctorate, Cohort 6 (EHR/HRD #1249206). Any opinions, findings and conclusions or recommendations expressed in this material are those of the authors and do not necessarily reflect the views of the National Science Foundation.

Supplemental Figures

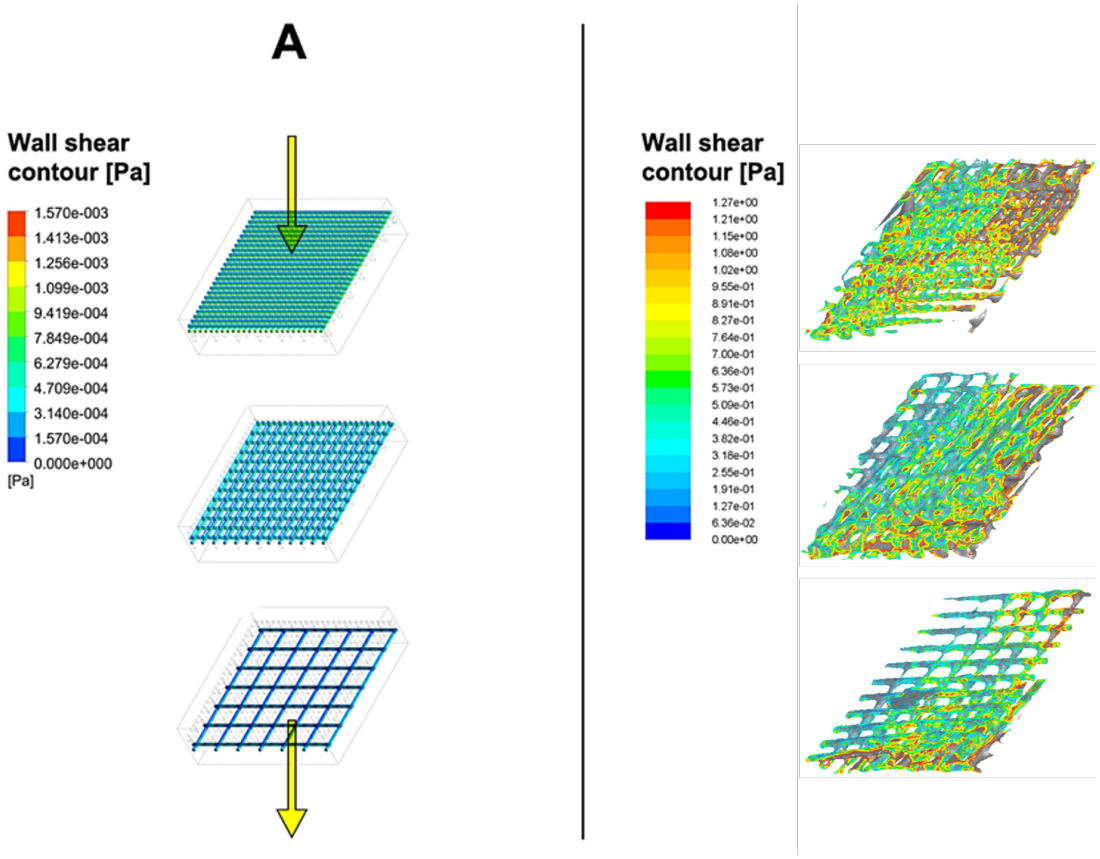

Figure 4.10: Wall shear stress (Pa) for SML a) STL files and b) μCT reconstructions at low flow rate (0.1 mL/min). Yellow arrows indicate the direction of flow. Simulations were conducted using FLUENT run either on the reconstructed scaffold or the original CAD model used to print said scaffolds.

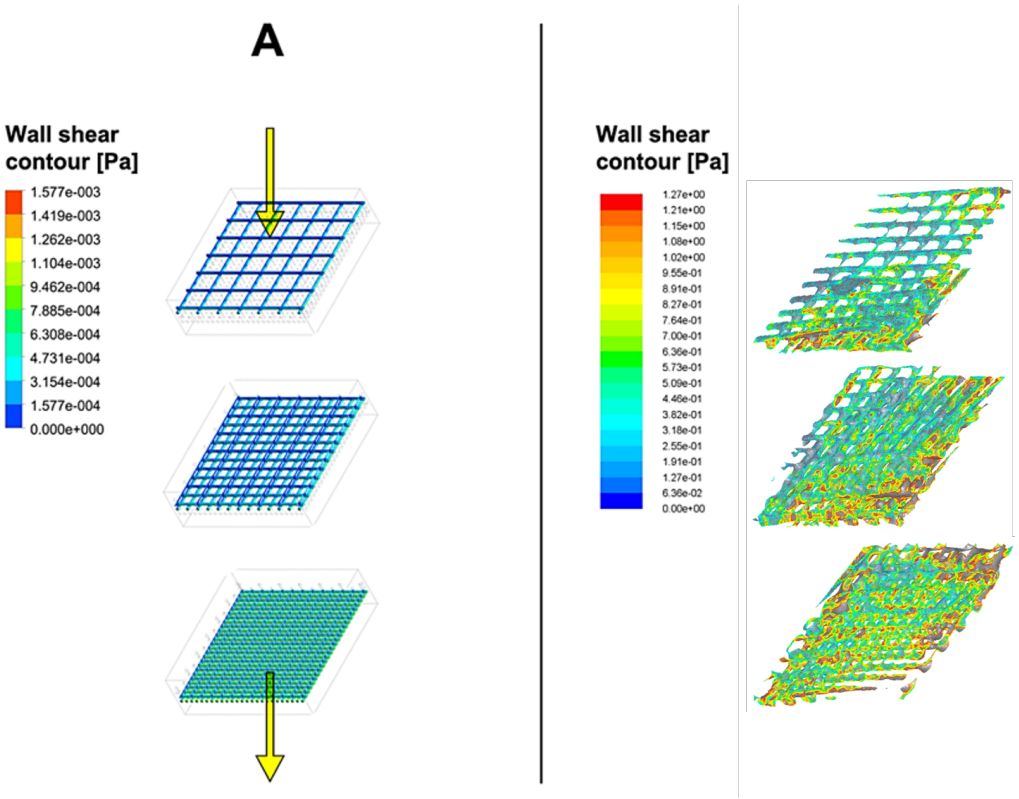

Figure 4.11: Wall shear stress (Pa) for LMS a) STL files and b) μCT reconstructions at low flow rate (0.1 mL/min). Yellow arrows indicate the direction of flow. Simulations were conducted using FLUENT run either on the reconstructed scaffold or the original CAD model used to print said scaffolds.

References

[1] D. L. Alge, J. Bennett, T. Treasure, S. Voytik-Harbin, W. S. Goebel, and T.-M. G. Chu. Poly(propylene fumarate) reinforced dicalcium phosphate dihydrate cement composites for bone tissue engineering. *Journal of Biomedical Materials Research Part A*, 100A(7):1792–1802, July 2012.

[2] J. F. Alvarez-Barreto, S. M. Linehan, R. L. Shambaugh, and V. I. Sikavitsas. Flow Perfusion Improves Seeding of Tissue Engineering Scaffolds with Different Architectures. *Annals of Biomedical Engineering*, 35(3):429–442, Feb. 2007.

[3] Antonios G. Mikos. Preparation and characterization of poly(L-lactic acid) foams.pdf. *Polymer*, 1994.

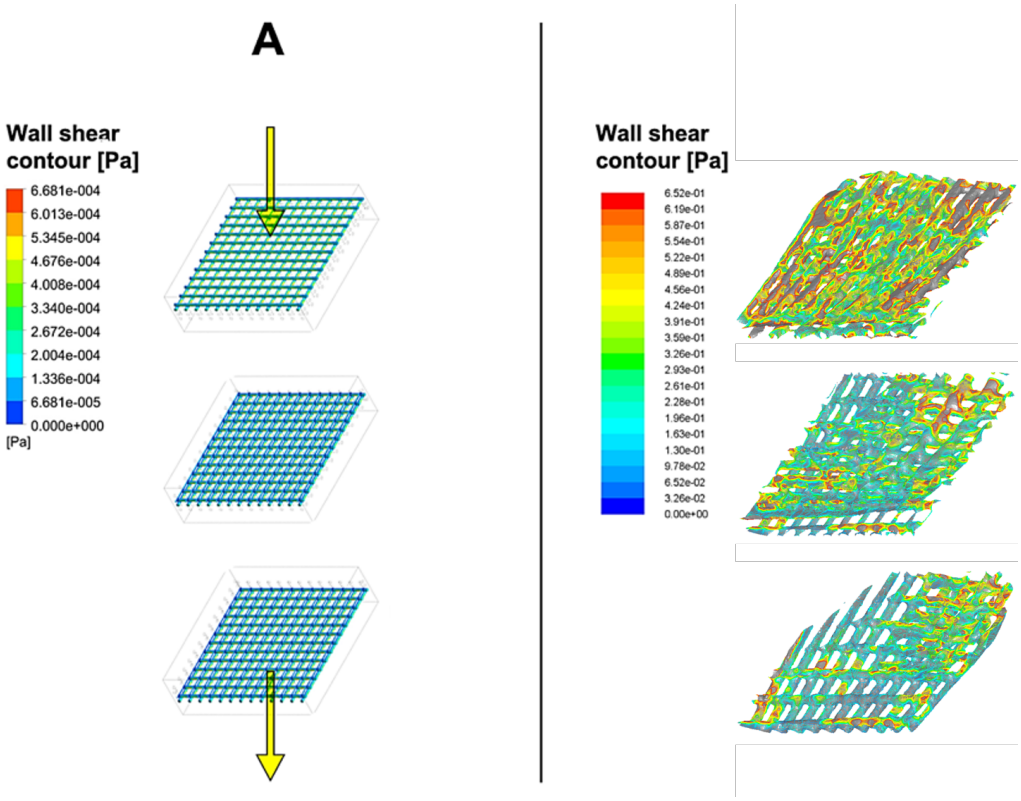

Figure 4.12: Wall shear stress (Pa) for MMM a) STL files and b) μCT reconstructions at low flow rate (0.1 mL/min). Yellow arrows indicate the direction of flow. Simulations were conducted using FLUENT run either on the reconstructed scaffold or the original CAD model used to print said scaffolds.

[4] R. B. Bird, W. E. Stewart, and E. N. Lightfoot. *Transport Phenomena*. J. Wiley, New York, 2nd, wiley international ed edition, 2002.

[5] C.-H. Chang, T.-C. Liao, Y.-M. Hsu, H.-W. Fang, C.-C. Chen, and F.-H. Lin. A poly(propylene fumarate) Calcium phosphate based angiogenic injectable bone cement for femoral head osteonecrosis. *Biomaterials*, 31(14):4048–4055, May 2010.

[6] H. N. Chia and B. M. Wu. Recent advances in 3d printing of biomaterials. *Journal of Biological Engineering*, 9(1):4, Dec. 2015.

[7] E. P. Childers, M. O. Wang, M. L. Becker, J. P. Fisher, and D. Dean. 3d printing of resorbable poly(propylene fumarate) tissue engineering scaffolds. *MRS Bulletin*, 40(02):119–126, Feb. 2015.

[8] J. P. Fisher, J. W. M. Vehof, D. Dean, J. P. C. M. van der Waerden, T. A. Holland, A. G. Mikos, and J. A. Jansen. Soft and hard tissue response to photocrosslinked poly(propylene fumarate) scaffolds in a rabbit model. *Journal of Biomedical Materials Research*, 59(3):547–556, Mar. 2002.

[9] E. L. S. Fong, B. M. Watson, F. K. Kasper, and A. G. Mikos. Building Bridges: Leveraging Interdisciplinary Collaborations in the Development of Biomaterials to Meet Clinical Needs. *Advanced Materials*, 24(36):4995–5013, Sept. 2012.

[10] E. L. Hedberg, H. C. Kroese-Deutman, C. K. Shih, R. S. Crowther, D. H. Carney, A. G. Mikos, and J. A. Jansen. In vivo degradation of porous poly(propylene fumarate)/poly(DL-lactic-co-glycolic acid) composite scaffolds. *Biomaterials*, 26(22):4616–4623, Aug. 2005.

[11] A. Henslee, P. Spicer, D. Yoon, M. Nair, V. Meretoja, K. Witherel, J. Jansen, A. Mikos, and F. Kasper. Biodegradable composite scaffolds incorporating an intramedullary rod and delivering bone morphogenetic protein-2 for stabilization and bone regeneration in segmental long bone defects. *Acta Biomaterialia*, 7(10):3627–3637, Oct. 2011.

[12] A. M. Henslee, D. M. Yoon, B. Y. Lu, J. Yu, A. A. Arango, L. P. Marruffo, L. Seng, T. D. Anver, H. Ather, M. B. Nair, S. O. Piper, N. Demian, M. E. K. Wong, F. K. Kasper, and A. G. Mikos. Characterization of an injectable, degradable polymer for mechanical stabilization of mandibular fractures: USE OF INJECTABLE PPF FORMULATIONS. *Journal of Biomedical Materials Research Part B: Applied Biomaterials*, 103(3):529–538, Apr. 2015.

[13] K. Kim, D. Dean, J. Wallace, R. Breithaupt, A. G. Mikos, and J. P. Fisher. The influence of stereolithographic scaffold architecture and composition on osteogenic signal expression with rat bone marrow stromal cells. *Biomaterials*, 32(15):3750–3763, May 2011.

[14] Langer and Vacanti. Tissue Engineering. *Science*.

[15] N. H. Pham, R. S. Voronov, S. B. VanGordon, V. I. Sikavitsas, and D. V. Papavassiliou. Predicting the stress distribution within scaffolds with ordered architecture. *Biorheology*, 49(4):235–247, 2012.

[16] B. Porter, R. Zauel, H. Stockman, R. Guldberg, and D. Fyhrie. 3-D computational modeling of media flow through scaffolds in a perfusion bioreactor. *Journal of Biomechanics*, 38(3):543–549, Mar. 2005.

[17] J. E. Trachtenberg, P. M. Mountziaris, J. S. Miller, M. Wettergreen, F. K. Kasper, and A. G. Mikos. Open-source three-dimensional printing of biodegradable polymer scaffolds for tissue engineering: Open-source 3dp of biodegradable polymer scaffolds. *Journal of Biomedical Materials Research Part A*, pages 4326–4335, Feb. 2014.

[18] J. E. Trachtenberg, J. K. Placone, B. T. Smith, C. M. Piard, M. Santoro, D. W. Scott, J. P. Fisher, and A. G. Mikos. Extrusion-Based 3d Printing of Poly(propylene fumarate) in a Full-Factorial Design. *ACS Biomaterials Science & Engineering*, 2(10):1771–1780, Oct. 2016.

[19] J. E. Trachtenberg, M. Santoro, C. Williams, C. M. Piard, B. T. Smith, J. K. Placone, B. A. Menegaz, E. R. Molina, S.-E. Lamhamedi-Cherradi, J. A. Ludwig, V. I. Sikavitsas, J. P. Fisher, and A. G. Mikos. Effects of Shear Stress Gradients on Ewing Sarcoma Cells Using 3d Printed Scaffolds and Flow Perfusion. *ACS Biomaterials Science & Engineering*, Feb. 2017.

[20] S. B. VanGordon. Three-dimensional bone tissue engineering strategies using polymeric scaffolds. *The University of Oklahoma. Dissertation*, 2012.

[21] R. Voronov, S. VanGordon, V. I. Sikavitsas, and D. V. Papavassiliou. Computational modeling of flow-induced shear stresses within 3d salt-leached porous scaffolds imaged via micro-CT. *Journal of Biomechanics*, 43(7):1279–1286, May 2010.

[22] R. S. Voronov, S. B. VanGordon, V. I. Sikavitsas, and D. V. Papavassiliou. Distribution of flow-induced stresses in highly porous media. *Applied Physics Letters*, 97(2):024101, 2010.

[23] E. R. Wagner, J. Parry, M. Dadsetan, D. Bravo, S. M. Riester, A. J. van Wijnen, M. J. Yaszemski, and S. Kakar. Chondrocyte Attachment, Proliferation, and Differentiation on Three-Dimensional Polycaprolactone Fumarate Scaffolds. *Tissue Engineering Part A*, Mar. 2017.

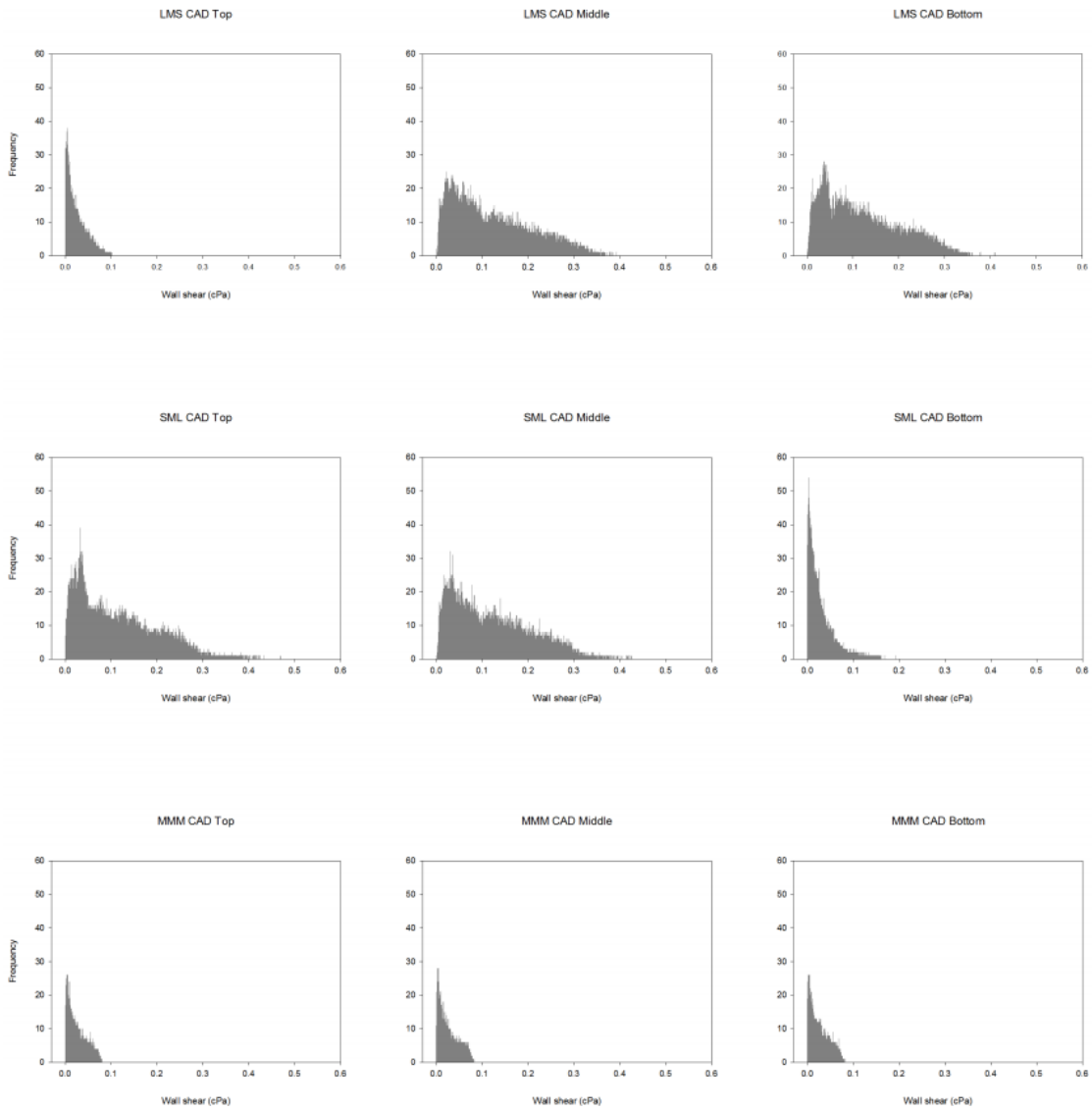

Figure 4.13: Wall shear stress distributions [cPa] based on gradient orientation (LMS, MMM, and SML) and scaffold type (CAD). Simulations were conducted using FLUENT run either on the reconstructed scaffold or the original CAD model used to print said scaffolds

Chapter 5

Time-Dependent Shear Stress Distributions during Extended Flow Perfusion Culture of Bone Tissue Engineering Constructs

Abstract

Flow perfusion bioreactors have been extensively investigated as a promising culture method for bone tissue engineering, due to improved nutrient delivery and shear force mediated osteoblastic differentiation. However, a major drawback impeding the transition to clinical relevant tissue regeneration is the inability to non-destructively monitor constructs during culture. To alleviate this shortcoming, we investigated the distribution of fluid shear forces in scaffolds cultured in flow perfusion bioreactors using computational fluid

dynamic techniques, analyzed the effects of scaffold architecture and surface chemistry on the shear forces, and monitored tissue mineralization throughout the culture period using micro-computed tomography. For this study, we dynamically seeded one million adult rat mesenchymal stem cells (MSCs) on 85% porous poly(L-lactic acid) (PLLA) polymeric spunbonded scaffolds. After taking intermittent sammples over 16 days, the constructs were imaged and reconstructed using micro-computed tomography. Fluid dynamic simulations were performed using FLUENT and a custom in-house lattice Boltzmann program. By taking samples at different time points during culture, we are able to monitor the mineralization and resulting changes in flow-induced shear distributions in the porous scaffolds as the constructs mature into bone tissue engineered constructs, and subsequently predict a constructs future growth.

5.1 Introduction

Every year in the United States, there are more than 500,000 bone graft surgeries [11]. In most cases, bone will regenerate after fracture with minimal complications; however, when there is a critical-sized defect or fracture healing is impaired, bone grafts must be used in order to regain proper bone function. Furthermore, bone diseases such as osteoporosis, infection, skeletal defects, and bone cancer may also cause a need for bone grafts. Bone tissue engineering is a possible solution to the problems plaguing the current bone graft therapies. Because tissue engineered bone would be made using the patients

This study was completed thanks to the collaborations listed in the acknowledgments. Listed here are the author contributions: CW performed cell culture; bioreactor experiments; image analysis; performed reconstructions and FLUENT flow simulations; performed data analysis. OEK performed LBM simulations; developed Figure 5.7 and 5.8b. GM performed microcomputed tomography imaging.

own cells, immune rejection would be eliminated. For this to work, four components are needed for tissue growth: cells that can be differentiated into bone cells, osteoconductive scaffolds for acting as a matrix while the tissue grows, growth factors and other chemical stimulation, and mechanical stimulation to encourage osteogenic differentiation. Mechanical stimulation, in particular, is implemented through the use of bioreactors.

Previous studies have given the indication that the shear stress cells experience inside the body are between 8-30 dynes/cm^2 [13]. *In vitro* culture studies combined with computational fluid dynamic simulation results have shown that shear stresses below 15 dynes/cm^2 are conducive to increased matrix production and osteoblastic differentiation. However, if the shear rates are too high, detachment or cell death can occur. Due to this, it is important to properly model and evaluate the flow profile inside cell-seeded scaffolds. Ideally, the localized shear rates would be anticipated in order to give proper fluid control. However, the largest barrier to this goal is the continual deposition of mineralized tissue during the culture period. After the stem cells differentiate into mature osteoblasts, both soft and hard extracellular matrix grow into the pores of the construct. This effectively alters the flow field, due to the porosity of the scaffold decreasing, and renders simulations performed on empty scaffolds invalid after the start of culture.

To combat this issue, we aimed to evaluate the localized fluid shear distributions throughout the culture period. Using spunbonded poly(l-lactic acid) scaffolds and a custom flow perfusion bioreactor, we cultured rat mesenchymal stem cells for 16 days under shear induced differentiation flow ranges. The resulting constructs were imaged utilizing μCT, segmented, and reconstructed

Figure 5.1: Common sythentic polymeric scaffolds used for tissue engineering. Scaffolds manufactured using spunbonding and imaged using SEM.

following previously published techniques [13, 8]. This flowpath allows for subsequent computational fluid dynamic (CFD) simulations on the cultured constructs.

In this manuscript, we hypothesized that the levels of fluid shear present at the walls of a scaffold, where the cells are located, will increase as a function of culture time. Previous studies have assumed that 1) the shear field predicted using a non-cultured scaffold is representative for cultured constructs and 2) that the average wall shear experienced by the cells is constant throughout a culture period [9, 5]. The intention of this study is to use CFD simulations in conjunction with microcomputed tomography of mature constructs and biochemical assays to bring to light the relationship between the localized shear field and culture time, which would give researchers the ability to predict the time dependant shear distribution in conjuction with the growing extracellular matrix within three dimensional scaffolds exposed to flow perfusion.

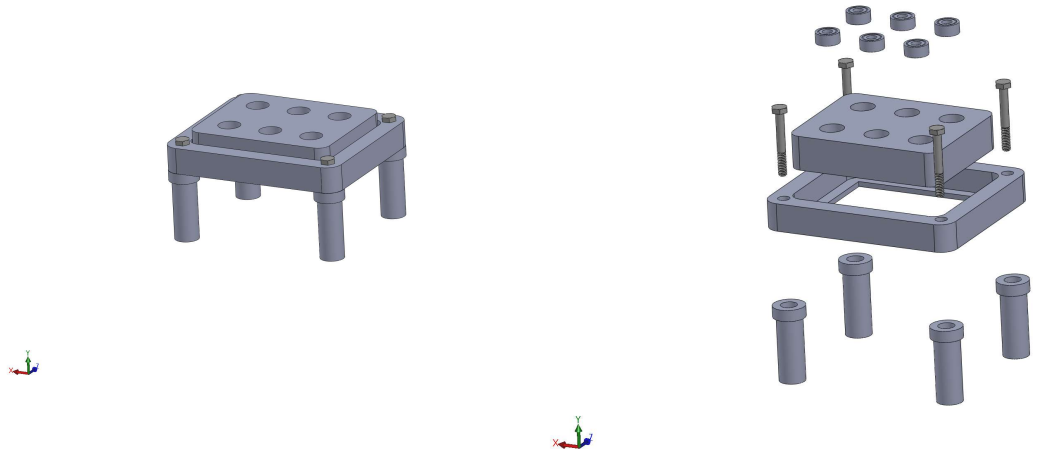

Figure 5.2: Schematic of custom in-house perfusion bioreactor system. The right image shows the combination of bioreactor body, scaffold cassettes, and stand.

5.2 Materials & Methods

5.2.1 Scaffold Manufacturing

Poly(L-lactic acid) (PLLA; grade 6251D; 1.4% D enantiomer; 108,500 MW; 1.87 PDI; NatureWorks LLC) nonwoven fiber mesh scaffolds were produced via spunbonding, as previously indicated from previous studies [12]. Scaffolds were cut from an 8mm thick PLLA mat, resulting in scaffolds of 88% porosity. A Nikon HFX-II microscope was used to evaluate fiber diameter, found to be 24.5 μm, and was confirmed by scanning electron microscopy, shown in Figure 5.1.

5.2.2 Cell Expansion, Seeding, and Culture

Adult mesenchymal stem cells were extracted from the tibias and femurs of male Wistar rats (Harlan Laboratories) using methods identified in previous publications [11, 1]). Cells were cultured at 37 ^{o}C, and 5% CO_2 in standard α-MEM (Invitrogen) supplemented with 10% fetal bovine serum (Atlanta Biologicals) and 1% antibiotic-antimycotic (Invitrogen). Passage 2 cells were used for this study at a density of 2 million cells/mL for scaffold seeding.

We prepped the scaffolds for cell seeding using an established pre-wetting technique [2]. Vacuum air removal of scaffolds was conducted in 75% ethanol. Pre-wet scaffolds were placed in cassettes within a flow perfusion bioreactor for a one hour in α-MEM to remove any remaining ethanol [6, 3]. Schematics of the perfusion system used for this study may be found in Figure 5.2. Following the flush, 2 million MSCs/150 μL of osteogenic α-MEM were pipetted in each each scaffold chamber. The seeding mixture was dynamically perfused at 0.15 mL/min, forwards and backwards, in five minute intervals for two hours. Osteogenic media consists of standard α-mem supplemented with dexamethasone, beta-glycerophosphate, and ascorbic acid, which have been shown to induce osteogenic differentiation [10]. After oscillatory seeding, the bioreactor was allowed to rest for two hours, without flow, to facilitate cell attachment. Finally, osteogenic α-MEM was continuously perfused at a rate of 0.5 mL/min/scaffold for the remainder of the culture period of 1, 4, 8, 11, and 16 days.

5.2.3 Construct Cellularity

The number of cells present in each construct was evaluated using fluorescent PicoGreen dsDNA assay (Invitrogen). At each sacrificial time point, the construct was removed from the cassette and dunked in PBS to remove any cells not adhered to the scaffold. Subsequently, the scaffolds were chopped into eight pieces, placed in 1 mL of DI H_2O, and stored at -20^{o}C. Each construct underwent three freeze/thaw cycles to lyse the cells. After following supplier protocols, solutions were run on a Synergy HT Multi-Mode Microplate Reader (Bio-Tek) at an excitation wavelength of 480 nm and an emission wavelength of 520 nm. All samples and standards were run in triplicate. Resulting values were then divided by the previously determined dsDNA content per cell of rMSCs which follows the equation below:

$$m_{\frac{dsDNA}{cell}}(pg) = 4.5 - 0.0102 * t^2 \tag{5.1}$$

,where t = culture time, which quantifies the loss of dsDNA content per cell as MSCs differentiate towards osteoblastic maturity.

5.2.4 Construct Calcium Deposition

Calcium deposition was measured utilizing the cellular lysate aquired following the freeze/thaw cycles of the previous section. The solution was measured with a calcium colorimetric assay using the manufacturer protocol (Sigma, Cat. # MAK022). Samples were again read on a Synergy HT Multi-Mode Microplate Reader (Bio-Tek) at an absorbance of 575 nm. All samples and standards were run in triplicate.

5.2.5 Imaging and Reconstruction

Micro-computed tomography was used to non-destructively scan the scaffolds (Quantum FX, Perkin Elmer, Waltham, MA; L10101, Hamamatsu Photonics, Japan; PaxScan 1313, Varian Medical Systems, Palo Alto, CA). The resulting 2D image slices were filtered, thresholded, and stacked using the open-source visualization software 3D Slicer (slicer.org). Following reconstruction, the porosity of the digital scaffold was measured and compared to the actual spunbonded scaffolds in order to assure a proper segmentation. This method has proven successful for previous studies [14]. For this study, we investigated a total of 4 different scaffolds for each day of construct sacrifice.

5.2.6 CFD Simulations

Simulations were performed via multiple methods to ensure the accuracy of the results - Finite Volume method implemented in Fluent 16.2 (ANSYS, Inc.) and Lattice-Boltzmann method implemented using a custom in-house Lattice-Boltzmann code, both of which have been extensively utilized for computing surface shear stresses on μCT reconstructions [13, 14, 8, 7]. Lattice Boltzmann simulations were conducted by our collaborators.

Fluent Simulations

Fluent simulations were conducted similarly to the previous chapter, with flat velocity profiles at the inlets based on a flow rate of 0.1 mL/min, no-slip boundary conditions imposed at the walls of the domain, and also an outlet with constant static pressure [8]. The domain for this study was a circular pipe with a diameter of about 5.5 mm. This cooresponds to the size of the

cassettes used in the bioreactors during culture. The culture medium was modeled as an incompressible Newtonian fluid with a dynamic viscosity of 1 cP, according to previous studies [13, 8]. In order to avoid any unwanted entrance effects and allow for fully developed laminar flow, we added a 4.8 mm long inlet channel in front of the scaffolds, which satisfies the conditions for laminar flow in a pipe [4]. Hydraulic radius (Dh), cross-sectional area (A), perimeter of the channel (m^2), Reynolds number (Re), average velocity (v), medium density (ρ), medium viscosity (μ), and entrance length (EL) and are defined in Equation 2-Equation 4:

$$D_h = \frac{4A}{P} = 10mm \tag{5.2}$$

$$Re = \frac{2D_h\langle v\rangle\rho}{\mu} << 1 \tag{5.3}$$

$$EL = 0.035ReD_h << 4.8mm \tag{5.4}$$

Scaffolds were meshed using approximately 5,520,000 grid cells with a size of 2 μm. Polyhedral element geometries were used for the scaffolds themselves, while tetrahedrals were used on the domain walls and the exit side of the scaffold to minimize computational time. The goal of this study is to evaluate the shear at the fluid-scaffold wall interface, therefore only wall shear values at these surface nodes were included in calculations. Additionally, shear distributions were plotted using 1,000 equally sized bins. It must be noted that wall shear stress as indicated in this chapter includes both the shear and normal stress on the walls of the scaffold.

5.2.7 Statistical Analysis

A one-way analysis of variance (ANOVA) was used to compare mean ± standard deviation of pore and fiber measurements, in which Tukeys Honestly Significant Difference (HSD) test was performed to identify significant differences (p-value < 0.05). One-way ANOVA and Tukeys HSD were used to the rest of the results. All statistical analysis was performed using a custom python code utilizing the open source Numpy, matplotlib, and SciPy libraries.

5.3 Results

5.3.1 Construct Cellularity

In order to validate the presence of cells in the constructs, we conducted a destructive dsDNA quantification assay. As shown in Figure 5.3, there is a slight decrease in scaffold cellularity between Day 1 and Day 4, and a statistically steady cellularity through the end of culture. The vertical dotted line between these Day 1 and Day 4 indicates the switch in flow rate from 0.15 mL/min to 0.5 mL/min. Hence the decrease between these two days represents a loss of cells due to an increase in shear stress experienced by the cells leading to detachment. This loss is a common occurence, as MSCs display a low rate of adherence during the seeding process. The horizontal dashed line represents the amount of cells initially seeded on the constructs. The ratio between this line and Day 1 is known as the seeding efficiency, which in this case is 40%.

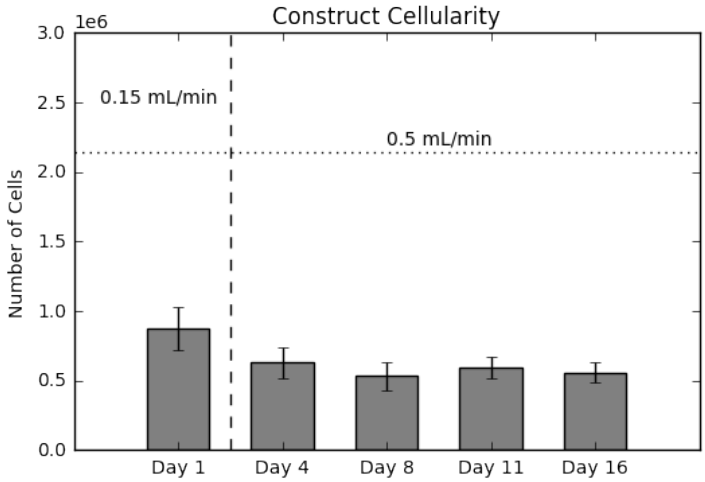

Figure 5.3: Construct cellularity for each construct over the culture period. Horizontal dashed line indicates the initial amount of cells seeded. Vertical dotted line indicates the switch in flow rates, from 0.15 mL/min during seeding to 0.5 mL/min for culture. Values are given as the mean ± standard error of the mean (n = 4).

5.3.2 Calcium Deposition

We followed this by descructively measuring the calcium deposited in each construct using a calcium assay, with results shown in Figure 5.4. As seen in the graph, there is a spike in calcium deposition around Day 8, due to osteoblasts depositing mineralized matrix. In conjuction to the calcium assay, we reconstructed the constructs, Figure 5.5, that were imaged using μCT. A similar spike in mineralized tissue can be seen around Day 11. Finally, Figure 5.6 is of a reconstructed scaffold and shows the location of mineralized tissue/ECM (red), soft tissue/ECM (yellow), and cells (green).

5.3.3 Shear Stress Distributions over Time

Additionally, we compared the localized fluid shear stress distributions for the reconstructions at each intermittent time point. Figure 5.7 shows the

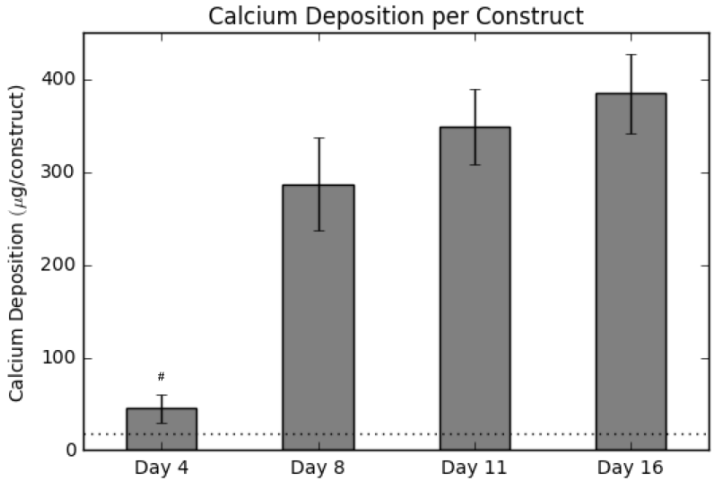

Figure 5.4: Calcium levels present within each construct over the culture period. The horizontal dotted line represents the background signal for an empty construct. Values are given as the mean ± standard error of the mean (n = 4). The # signifies the significantly lowest value.

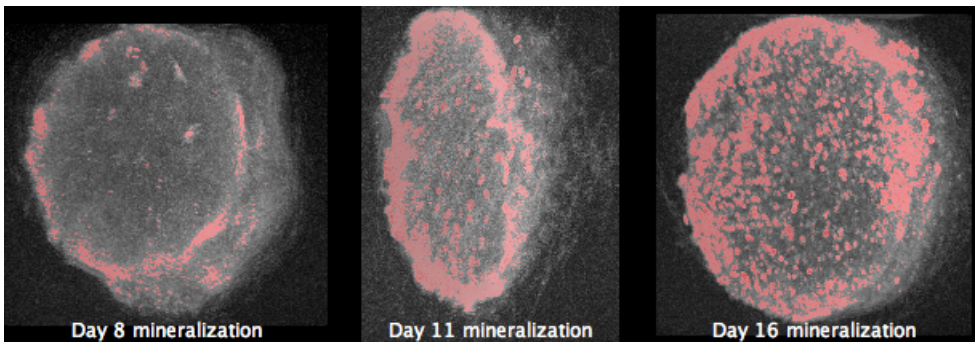

Figure 5.5: Summary of mineralized tissue (hard ECM) deposited in cultured constructs reconstructed following μCT of Days 8, 11, and 16, respectively. Calcium is indicated in red.

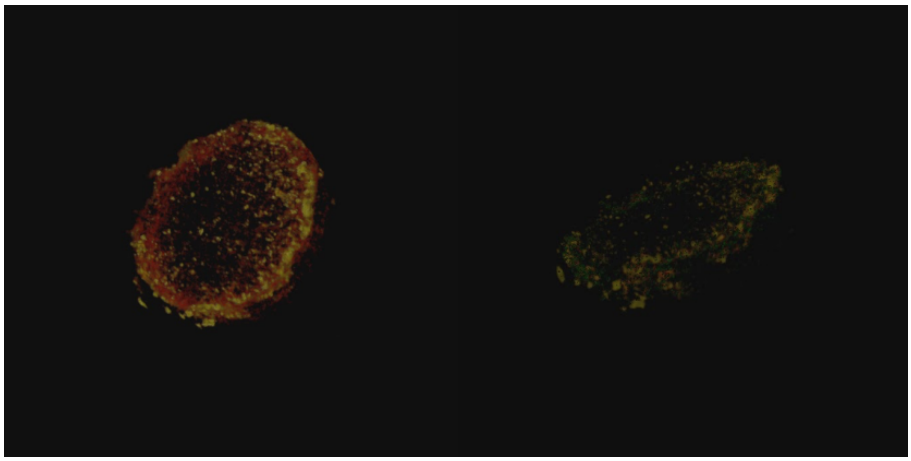

Figure 5.6: Summary of mineralized tissue (hard ECM) deposited in Day 16 cultured constructs reconstructed following μCT. Mineralized tissue = Red, PLLA fibers = Gray, Cells outside of ECM = Green, Soft tissue = Yellow

frequency of flow induced stresses. The data presented show a pronounced increase shear stress levels with an increase in culture time.

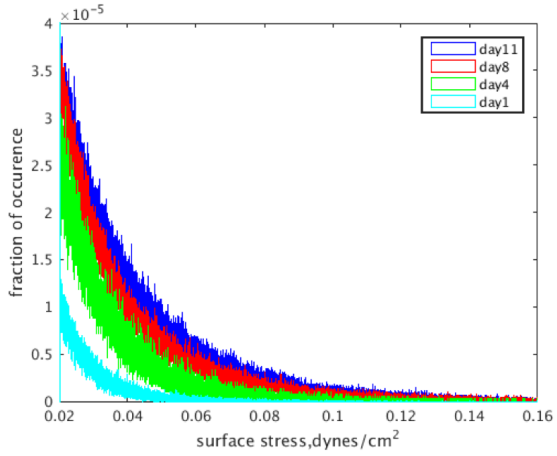

Figure 5.7: Wall shear stress distributions based on the day a construct was removed from culture and imaged.

5.3.4 Effects of Calcium Deposition on Localized Shear Fields

Figure 5.8 shows iso sections of reconstructed scaffolds, with wall shear stress heat maps overlaid on top. It is evident that there are higher levels of shear stress present during the later time points, which is supported distributions shown in Figure 5.7.

5.3.5 Average Wall Shear Stress

Figure 5.9 displays the average wall shear stress calculated from simulations following construct culture, resection, imaging, and reconstruction. Indeed, the results do indeed show a continuous increase in shear as a culture time increases, which is consistent with the previous sections.

5.4 Discussion

Following destructive analysis of the constructs, we evaluated the average wall shear stress per construct as a function of culture time. As seen in Figure 5.9, the average shear stress remains statisctically the same throughout the first 4 days of culture; however, after Day 8, there is a continual increase in the value to the end of the culture period. This finding confirms our hypothesis about bone tissue engineered cultures; that the shear stress experienced by the cells will increase during culture. We attribute this to calcium deposition resulting in a clogging of the construct pores. By holding the flow rate constant and simaltaneusly decreasing the pore sizes, we effectively are increasing the fluid velocity within the construct interior, and, along with it, the wall shear stress.

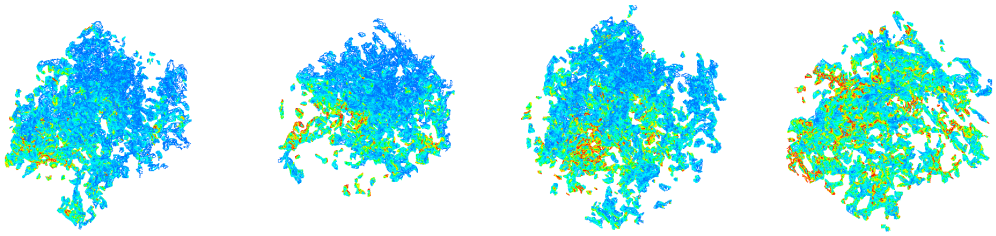

(a) Wall shear heat map for Day 1 (far left) to Day 11 (far right)

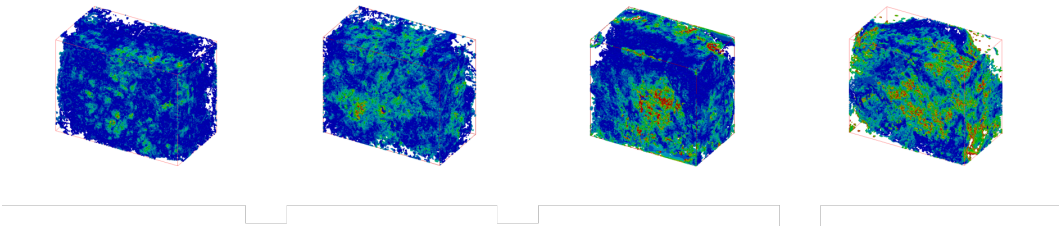

(b) Wall shear heat map for Day 1 (far left) to Day 11 (far right)

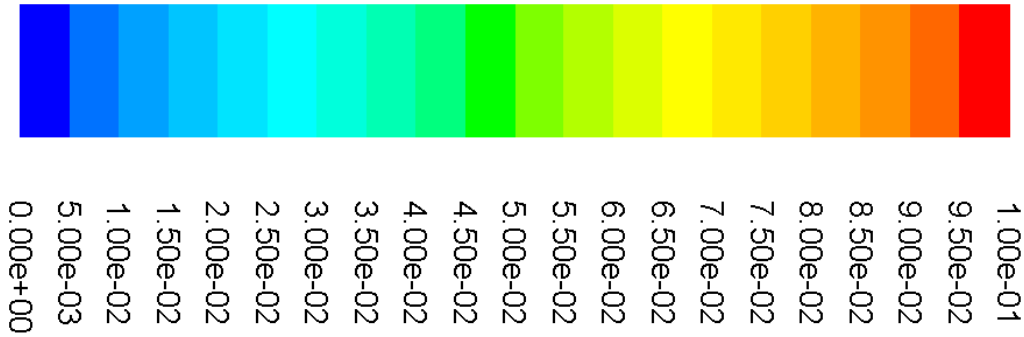

(c) Scale bar: Values given in Pa

Figure 5.8: Summary of wall shear stress heat maps for constructs cultured under osteoinducive conditions. Simulations for (a) were conducted using FLUENT, and simulations for (b) were conducted using a custom LBM code.

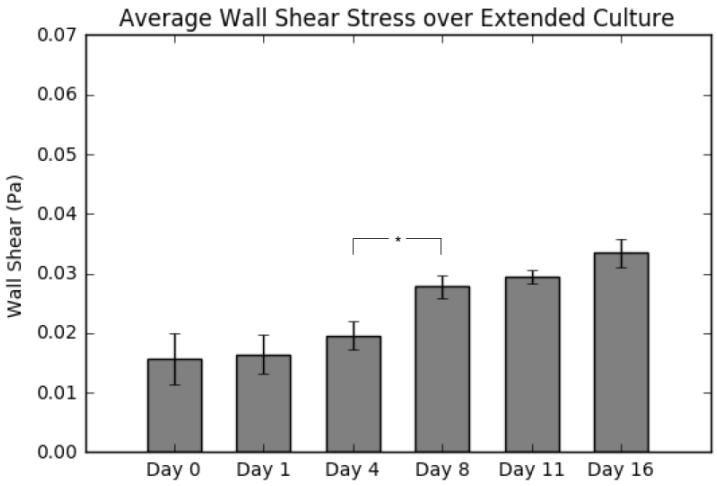

Figure 5.9: Summary of average shear stress per layer on the walls of the scaffold for 0.1 mL/min flow rate. Values are given as the mean ± standard error of the mean (n = 4). Significance calculated via ANOVA with Tukey HSD Post-hoc analysis.

After evaluating the construct reconstructions, we can see a clear coorelation to the amount of mineralized tissue and an overall increase in the magnitude of wall shear experienced within the pores of the construct. Indeed this relationship is obvious in both Figure 5.7, showing the frequency distributions, and Figure 5.8, which shows the wall shear heat maps. For the former, the distributions show an increased frequency of elevated shear stress as culture time increases, supporting the aforementioned increase in average wall shear stress.

This finding is consistent when evaluating the heat maps. As culture time increases, there is a higher density of elevated shear seen within the constructs. This increase is most pronounced after day 11, which, according to the reconstructions, is when large amounts of mineralized tissue is seen. An additional positive finding is that the results are consistent when comparing the results obtained utilizing FLUENT simulations and those from the in-house Lattice

Boltzmann code, validating those methods.

Additionally, we evaluated the scaffold cellularity and the levels of mineralized tissue deposited. As seen in Figure 5.3, we achieved a seeding efficiency of 40%, higher than most perfusion based seeding methods, and can be directly attributed to the oscillatory seeding protocol we established in previous studies. Following the initial loss of cells during the seeding process, the amount of cells per construct levels off after Day 4, consistent with previous results, where an increase is not commonly seen as mature osteoblasts have both a slower growth rate and become hidden by deposited calcium. We believe the decrease in cellularity seen between Day 1 and Day 4 is due to increasing the flow rate to a more osteoinducive level following the seeding protocol, and thusly causing more cells to detach from the scaffold.

In Figures 5.4, 5.5, and 5.6, quantitative and qualitative measures of tissue mineralization per construct are compared. In the former, a spike in calcium production is seen between Day 4 and Day 8. This is consistent with our previous studies. In comparison, Figure 5.5 shows an increase in mineralized tissue found utilizing μCT between Day 8 and Day 11. We believe this lag time is due to the cells beginning to deposit calcium that is not dense enough to be picked up during imaging segmentation around Day 8. Along with this, Figure 5.6 shows a Day 16 reconstruction with mineralized tissue, soft tissue, and cells. This image illustrates the state of the consstruct at the end of culture, and gives insight into the density of mineralization that would occur if culture continued. It is to be expected that the soft tissue visualized in the image will eventually transition into fully mineralized tissue. Also of importance, the cells (green) are not indicative of the total construct cellularity. Osteoblasts

are commonly trapped inside deposited hydroxapatite in the body, and are henceforth known as osteocytes. *in vitro*, it is difficult to quantify these cells without destructively breaking down the mineral deposits to expose the cells.

5.5 Conclusion

In the presented manuscript, we hypothesized that the distribution of fluid shear present at the walls of a construct cultered under osteoinducive conditions will exhibit higher magnitudes as culture increases. In order to accomplish this, rat mesenchymal stem cells were dynamically seeded on 85% porous spunbonded poly(l-lactic acid), and cultured with osteogenic media for up to 16 days under an osteoinducive flow rate. Following culture, these constructs were either destructively evaluated with assays for cell viability and calcium deposition, or imaged using μCT and reconstructed to allow for CFD simulations to be performed. Average shear stress values and shear stress frequency distributions obtained from simulations were compared with the assays, and confirmed our original hypothesis. In terms of the calcium quantification assay, a spike is seen around Day 8. This finding is supported by the reconstructions, where imaging identified an increase in mineralized tissue around Day 11. Additionally, the shear distribution heat maps show elevated magnitudes of shear stress after Day 11. Finally, we proved that both the shear stress distributions and the average shear stress per construct consistently increase as a function of culture time. This is due to mineralization occuring within the pores of the scaffold, decreasing pore diameter, and affectively increasing velocity withing the pores. In future studies, a correlation or algorithm will be identified that will give users the ability to predict the fluid shear distribution in a bone tissue

engineered culture by only running fluid dynamic simulations on the empty scaffolds.

5.6 Acknowledgements

I acknowledge collaborators Olufemi Emmanuel Kadri and Roman S. Voronov located at Otto H. York Department of Chemical, Biological, and Pharmaceutical Engineering, New Jersey Institute of Technology, NJ. I acknowledge support from Ghani Muhammed and Hong Liu for imaging assistance. This work was funded in part by the Gustavus and Louise Pfeiffer Research Foundation, and the Oklahoma Center for the Advancement of Science and Technology (HR13-214). I gratefully acknowledge fellowship funding from the Oklahoma Louis Stokes Alliance for Minority Participation (OK-LSAMP) Bridge to the Doctorate, Cohort 6 (EHR/HRD #1249206). Any opinions, findings and conclusions or recommendations expressed in this material are those of the authors and do not necessarily reflect the views of the National Science Foundation.

References

[1] J. F. Alvarez-Barreto, S. M. Linehan, R. L. Shambaugh, and V. I. Sikavitsas. Flow Perfusion Improves Seeding of Tissue Engineering Scaffolds with Different Architectures. *Annals of Biomedical Engineering*, 35(3):429–442, Feb. 2007.

[2] J. F. Alvarez-Barreto and V. I. Sikavitsas. Improved Mesenchymal Stem Cell Seeding on RGD-Modified Poly(L-lactic acid) Scaffolds using Flow Perfusion. *Macromolecular Bioscience*, 7(5):579–588, May 2007.

[3] G. N. Bancroft, V. I. Sikavitsas, J. Van Den Dolder, T. L. Sheffield, C. G. Ambrose, J. A. Jansen, and A. G. Mikos. Fluid flow increases mineralized matrix deposition in 3d perfusion culture of marrow stromal osteoblasts in a dose-dependent manner. *Proceedings of the National Academy of Sciences*, 99(20):12600–12605, 2002.

[4] R. B. Bird, W. E. Stewart, and E. N. Lightfoot. *Transport Phenomena*. J. Wiley, New York, 2nd, wiley international ed edition, 2002.

[5] E. P. Childers, M. O. Wang, M. L. Becker, J. P. Fisher, and D. Dean. 3d printing of resorbable poly(propylene fumarate) tissue engineering scaffolds. *MRS Bulletin*, 40(02):119–126, Feb. 2015.

[6] Mikos. Flow perfusion culture of mesenchymal stem cells for bone tissue engineering. *StemBook*, 2008.

[7] N. H. Pham, R. S. Voronov, S. B. VanGordon, V. I. Sikavitsas, and D. V. Papavassiliou. Predicting the stress distribution within scaffolds with ordered architecture. *Biorheology*, 49(4):235–247, 2012.

[8] B. Porter, R. Zauel, H. Stockman, R. Guldberg, and D. Fyhrie. 3-D computational modeling of media flow through scaffolds in a perfusion bioreactor. *Journal of Biomechanics*, 38(3):543–549, Mar. 2005.

[9] B. Porter, R. Zauel, H. Stockman, R. Guldberg, and D. Fyhrie. 3-D computational modeling of media flow through scaffolds in a perfusion bioreactor. *Journal of Biomechanics*, 38(3):543–549, Mar. 2005.

[10] J. R. Porter, T. T. Ruckh, and K. C. Popat. Bone tissue engineering: A review in bone biomimetics and drug delivery strategies. *Biotechnology Progress*, pages NA–NA, 2009.

[11] S. B. VanGordon. Three-dimensional bone tissue engineering strategies using polymeric scaffolds. *The University of Oklahoma. Dissertation*, 2012.

[12] S. B. VanGordon, R. S. Voronov, T. B. Blue, R. L. Shambaugh, D. V. Papavassiliou, and V. I. Sikavitsas. Effects of Scaffold Architecture on Preosteoblastic Cultures under Continuous Fluid Shear. *Industrial & Engineering Chemistry Research*, 50(2):620–629, Jan. 2011.

[13] R. Voronov, S. VanGordon, V. I. Sikavitsas, and D. V. Papavassiliou. Computational modeling of flow-induced shear stresses within 3d salt-leached porous scaffolds imaged via micro-CT. *Journal of Biomechanics*, 43(7):1279–1286, May 2010.

[14] R. S. Voronov, S. B. VanGordon, V. I. Sikavitsas, and D. V. Papavassiliou. Distribution of flow-induced stresses in highly porous media. *Applied Physics Letters*, 97(2):024101, 2010.

Chapter 6

Future Directions

The research projects presented herein answer vital problems plaguing the bone tissue and tumor engineering fields. In particular, the studies answered three main questions: 1) How can we improve both mesenchymal stem cell and cancer cell adherence to the scaffolds? 2) In terms of flow-induced stresses, what is the viability of 3D printing for manufacturing repeatable scaffold architectures? 3) Do the shear stresses within a bone tissue engineered construct change over the culture period? In summary, we accomplished the following: 1) developed a functionally flexible surface modification technique and increase MSC seeding efficiency by 50%; 2) applied that modification scheme to increase cancer cell adhesion by 25%; 3) brought to light the differences in shear stress distributions between CAD models and the actual printed scaffolds; 4) both validated the repeatability of 3D printing and provided a probibility density function that describes the shear stress distributions therein; and 5) proved the existence of increasing shear stresses withing bone cultures over time due to calcium deposition.

An expansion of Chapters 2 and 3 would be the development of best prac-

tices for growing both a wider range of cells and a wider range of base materials [7, 3, 2, 4]. As mentioned previously, RGD-mediated attachment of MSCs was used as a proof of concept, whereas the n-cadherin mediated attachment was a possible application of said method. For the former, work is needed to leverage the modifciation scheme for moiteies that can direct cellular recruitment and differentiation states, in an attempt to circumvent the aforementioned restrictions imposed by the FDA [10, 14, 6, 15, 5]. In regards to the latter, the next step for the development of an *in vitro* tumor model is to monitor the effectiveness of chemotherapeutic treatment on the modified constructs in comparison to *in vivo* tumors [12]. Following the development and seeding of the n-cadherin modified scaffold with tumor cells, chemotherapeutic agents will be perfused in order to compare expressed genes, tissue organization, and cell death. The overall goal of this study would be to compare the cellular response to antitumor drugs in the tumor engineered environment to that of a mouse model. A positive result would be to see no statistical difference in the aforementioned tests, proving that the modification scheme presented in this manuscript would allow for the development of clinically relevant samples for *in vitro* diagnostic testing. Additionally, the development of a coculture containing both bone and cancer cells of a metastatic lineage would lead to models that can help researchers more effectively develop prospective drug therapies [9].

There are three future goals for the advancement of the work presented in Chapter 4: 1) expansion of the work to different materials; 2) fabrication of the investigated scaffold orientations using different 3D printers; 3) prediction of wall shear fields from only the CAD models. It has been well established

that the polymers commonly used in tissue engineering, PLLA, PLGA, PPF, etc., behave differently during FDM printing. Similarly, the various printers on the market have different capabilities, such as resolution, that could affect the resulting scaffold [13]. Furthermore, there are other factors that can skew results (printer location, humidity, vibration, slicer software, build plate adhesive, and post processing) that need to be investigated. Due to these reasons, it is important to explore the validity of the study when taking into account the aforementioned variabilities.

The third future goal, which is the development of a suite of predictive tools that can anticipate the fluid flow field within constructs, is also applicable to Chapter 5 as well. Predictive tools are not new to the field of tissue engineering, and have helped researchers predict a wide range of responses from patient responses to chemotherapeutics to material properties during culture [1, 8, 11]. As mentioned previously, the large discrepancy in wall shear magnitudes found in the reconstructions and the CAD models is due to differenecs in surface roughness and defects from the printing process. By utilizing machine learning algorithms, these differences can be anticipated and would allow researchers to tailor scaffold architectures for enhanced cell stimulation before running any experiments, saving valuable time and resources.

The research projects presented in this manuscript aim to alleviate many of the common problems facing the advancement of bone tissue and tumor engineering. This is accomplished by developing a functionally flexible biomimetic surface modification platform to increase cellular attachment for both mesenchymal-derived cells and tumor cells, investigating the effects of 3D printing on the resulting scaffold and flow-induced shear distributions, and characterizing the

changes in flow-induced shear distributions caused by osteoblastic calcium deposition. Indeed, issues still remain that impead a clinical transition; however, the work presented herein push the fields of bone tissue and tumor engineering ever closer to that goal.

References

[1] M. . Ariza-Gracia, S. Redondo, D. Piero Llorens, B. Calvo, and J. F. Rodriguez Matas. A predictive tool for determining patient-specific mechanical properties of human corneal tissue. *Computer Methods in Applied Mechanics and Engineering*, 317:226–247, Apr. 2017.

[2] A. Civantos, E. Martnez-Campos, V. Ramos, C. Elvira, A. Gallardo, and A. Abarrategi. Titanium Coatings and Surface Modifications: Toward Clinically Useful Bioactive Implants. *ACS Biomaterials Science & Engineering*, 3(7):1245–1261, July 2017.

[3] W. Jiang, Q. Tian, T. Vuong, M. Shashaty, C. Gopez, T. Sanders, and H. Liu. Comparison Study on Four Biodegradable Polymer Coatings for Controlling Magnesium Degradation and Human Endothelial Cell Adhesion and Spreading. *ACS Biomaterials Science & Engineering*, 3(6):936–950, June 2017.

[4] P. Kerativitayanan, M. Tatullo, M. Khariton, P. Joshi, B. Perniconi, and A. K. Gaharwar. Nanoengineered Osteoinductive and Elastomeric Scaffolds for Bone Tissue Engineering. *ACS Biomaterials Science & Engineering*, 3(4):590–600, Apr. 2017.

[5] J. K. Leach and J. Whitehead. Materials-Directed Differentiation of Mesenchymal Stem Cells for Tissue Engineering and Regeneration. *ACS Biomaterials Science & Engineering*, Mar. 2017.

[6] J. Lee, S. K. M. Perikamana, T. Ahmad, M. S. Lee, H. S. Yang, D.-G. Kim, K. Kim, B. Kwon, and H. Shin. Controlled Retention of BMP-2-Derived Peptide on Nanofibers Based on Mussel-Inspired Adhesion for Bone Formation. *Tissue Engineering Part A*, 23(7-8):323–334, Apr. 2017.

[7] S. Li, Y. Xu, J. Yu, and M. L. Becker. Enhanced osteogenic activity of poly(ester urea) scaffolds using facile post-3d printing peptide functionalization strategies. *Biomaterials*, 141:176–187, Oct. 2017.

[8] C.-M. Lo, U. Iqbal, and Y.-C. Li. Cancer quantification from data mining to artificial intelligence. *Computer Methods and Programs in Biomedicine*, 145:A1, July 2017.

[9] A. Malandrino, R. D. Kamm, and E. Moeendarbary. In Vitro Modeling of Mechanics in Cancer Metastasis. *ACS Biomaterials Science & Engineering*, June 2017.

[10] N. Peela, D. Truong, H. Saini, H. Chu, S. Mashaghi, S. L. Ham, S. Singh, H. Tavana, B. Mosadegh, and M. Nikkhah. Advanced biomaterials and microengineering technologies to recapitulate the stepwise process of cancer metastasis. *Biomaterials*, 133:176–207, July 2017.

[11] C. R. Shurer, M. J. Colville, V. K. Gupta, S. E. Head, F. Kai, J. N. Lakins, and M. J. Paszek. Genetically Encoded Toolbox for Glycocalyx Engineering: Tunable Control of Cell Adhesion, Survival, and Cancer Cell Behaviors. *ACS Biomaterials Science & Engineering*, Apr. 2017.

[12] A. M. Sitarski, H. Fairfield, C. Falank, and M. R. Reagan. 3d Tissue Engineered in Vitro Models of Cancer in Bone. *ACS Biomaterials Science & Engineering*, July 2017.

[13] J. E. Trachtenberg, M. Santoro, C. Williams, C. M. Piard, B. T. Smith, J. K. Placone, B. A. Menegaz, E. R. Molina, S.-E. Lamhamedi-Cherradi, J. A. Ludwig, V. I. Sikavitsas, J. P. Fisher, and A. G. Mikos. Effects of Shear Stress Gradients on Ewing Sarcoma Cells Using 3d Printed Scaffolds and Flow Perfusion. *ACS Biomaterials Science & Engineering*, Feb. 2017.

[14] E. R. Wagner, J. Parry, M. Dadsetan, D. Bravo, S. M. Riester, A. J. van Wijnen, M. J. Yaszemski, and S. Kakar. Chondrocyte Attachment, Proliferation, and Differentiation on Three-Dimensional Polycaprolactone Fumarate Scaffolds. *Tissue Engineering Part A*, Mar. 2017.

[15] T.-T. Yu, F.-Z. Cui, Q.-Y. Meng, J. Wang, D.-C. Wu, J. Zhang, X.-X. Kou, R.-L. Yang, Y. Liu, Y. S. Zhang, F. Yang, and Y.-H. Zhou. Influence of Surface Chemistry on Adhesion and Osteo/Odontogenic Differentiation of Dental Pulp Stem Cells. *ACS Biomaterials Science & Engineering*, 3(6):1119–1128, June 2017.

Appendix

Cell Spreading Calculations

Cell spreading is a measurement of the actin area covered by a cell. As such, it is an easily measurable value that can indicate the binding strength between a cell and a surface. In Chapters 2 and 3, it was used to quantify a functionalized scaffold's increased capacity for cellular attachment as a function of the extent of expressed RGD or n-cadherin. In order to find this value, the following steps were used: (1) scaffolds were first functionalized to express RGD or n-cadherin, (2) cells were seeded and allowed to adhere, (3) cell seeded scaffolds were fixed, stained, and imaged, and (4) resulting fluorescent images were examined using the calculations found below. Steps 1-3 are outlined in detail in Chapters 2 and 3.

For the sample calculation provided below, ImageJ was used for area quantification. To obtain this value, fluorescent images of either the cell nuclei or actin were opened in ImageJ. Following this, the image was thresholded to subtract any background and highlight the nuclei or actin, and the "analyze particles" tool was used to measure the pixel area of the highlighted image features, which was converted to μm using the microscopes calibration data.

The measurements of nuclei area to actin area were then normalized by diving the latter by the former, giving the ratio of cell actin area to cell nuclei area. This is necessary, because the actin per cell is not perfectly isolated from the actin of its neighbor when there is a high density of cells, resulting in overlap. An example calculation for values used in Figure 2.7 may be found below:

$$Total\,actin\,area\,from\,ImageJ = 36,690\mu^2 \tag{A.1}$$

$$Total\,nuclei\,area\,from\,ImageJ = 8,636.8\mu^2 \tag{A.2}$$

$$Cell\,spreading = \frac{actin\,surface\,area}{nucleus\,surface\,area} = \frac{36,690}{8,636.8} = 4.24 \tag{A.3}$$

Fluent Methodology

In order to conduct the FLUENT simulations, we used the ANSYS Workbench program, shown in Figure A1. Workbench contains a collection of various computational programs useful for CFD or biomechanic studies. The FLUENT (with meshing) program is one of the foremost CFD packages and is used for both commercial and academic investigations. Three main steps were conducted to generate the data presented in this manuscript: (1) scaffold meshing for both CAD designs and reconstructions; (2) simulation domain setup; (3) post-processing. A more detailed description for each stage is discussed below.

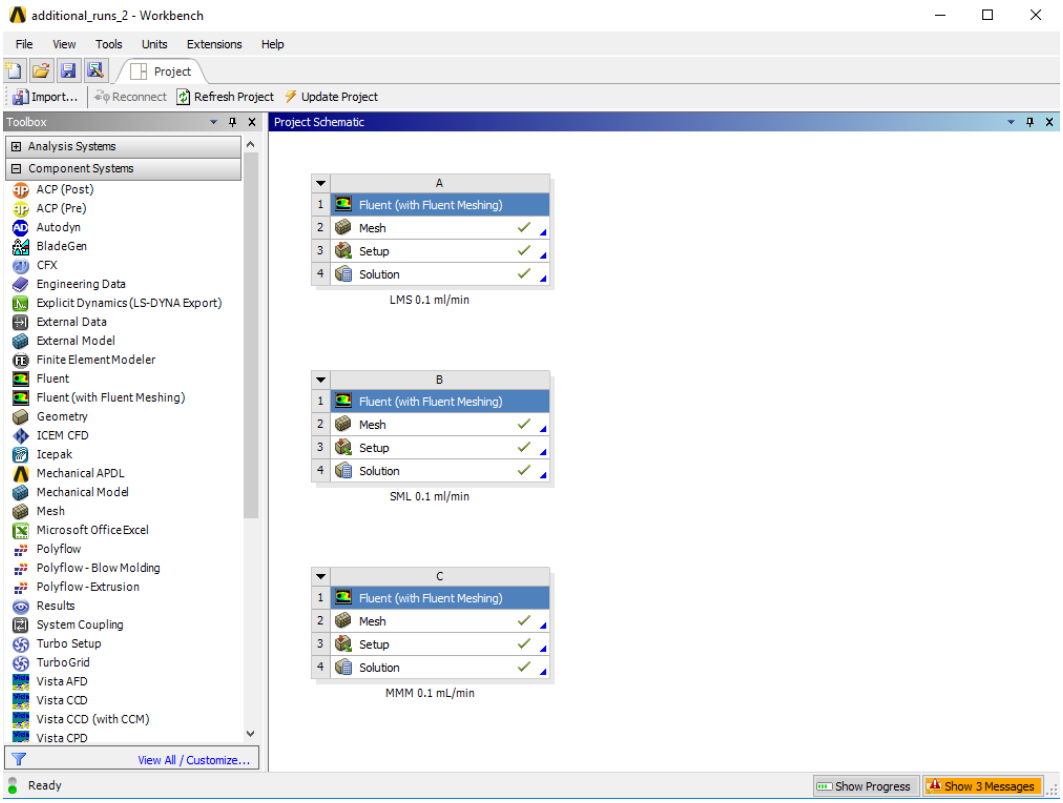

Figure A.1: The ANSYS Workbench main screen. Available systems are shown on the panels on the left. The area on the right may be used to organize a collection of component modules, or connect modules for crosstalk. This screenshot shows the different FLUENT instances used to conduct CFD simulations for scaffolds at a flow rate of 0.1 mL/min.

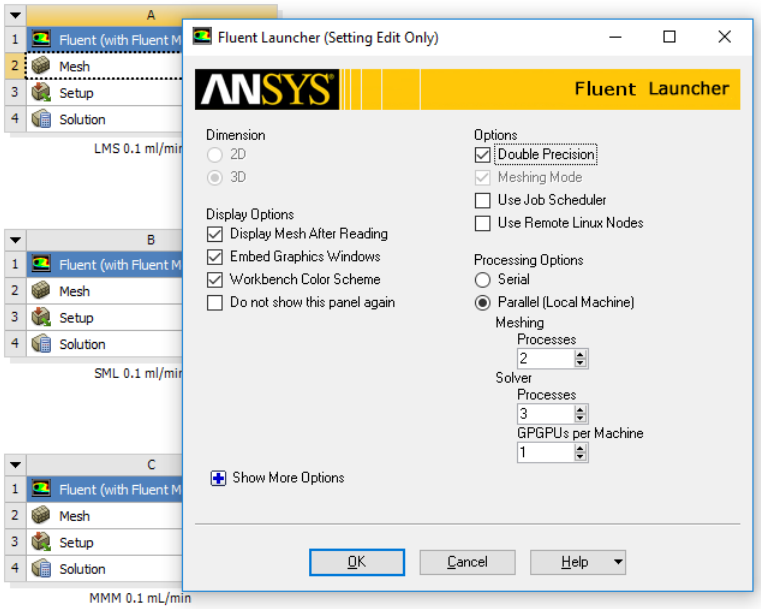

Figure A.2: The FLUENT meshing prelaunch setup. Here you will select the floating-point format and the processing type (serial, local parallel, distributed parallel).

Meshing

To set the computational domain and mesh the scaffolds, start by opening the Mesh option and setting the appropriate settings (Figure A2). Once the module opens, import the CAD design or reconstructed scaffold file making sure to select the correct unit system (Figure A3). Once complete, create the bioreactor cassette, or computational domain, for the simulations (Figure A4). It is important to alter the inlet side to create a larger flow inlet to allow for proper flow field development, as discussed in Chapters 4 and 5. Following this, convert both objects to mesh objects and set the sizing field and fluid domain. The last step is to wrap the cassette and scaffold together, mesh the system, and prepare the flow domain (Figures A5 and A6).

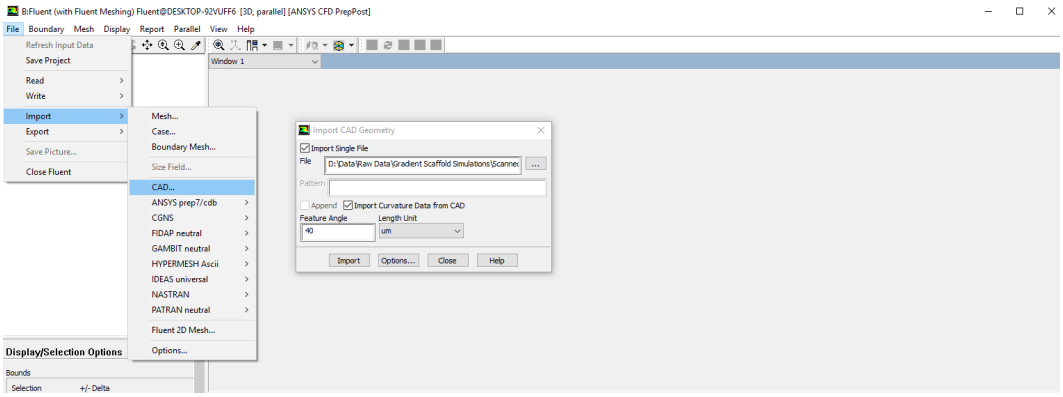

Figure A.3: CAD file importation in FLUENT. FLUENT supports a wide range of file formats, including .stl and .iges.

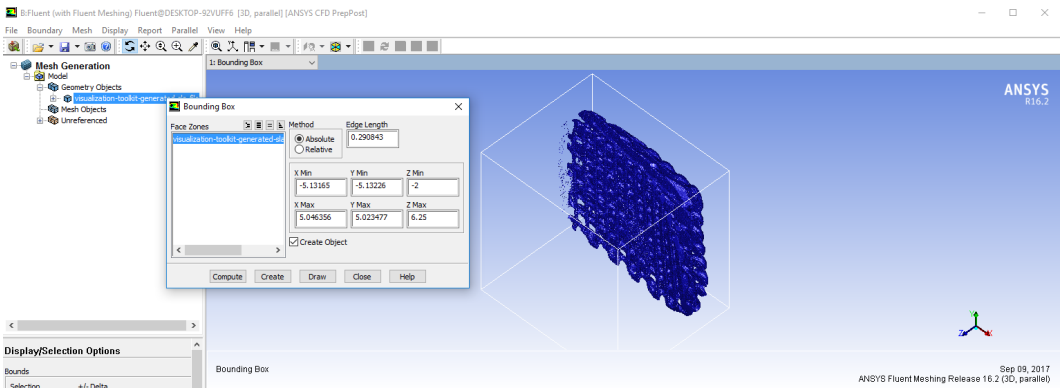

Figure A.4: Bounding box generation, which is equivalent to the cassette used for perfusion bioreactors. As such, it is important to use the same dimensions seen experimentally. The purpose of the box is to indicate the computational domain for the simulations.

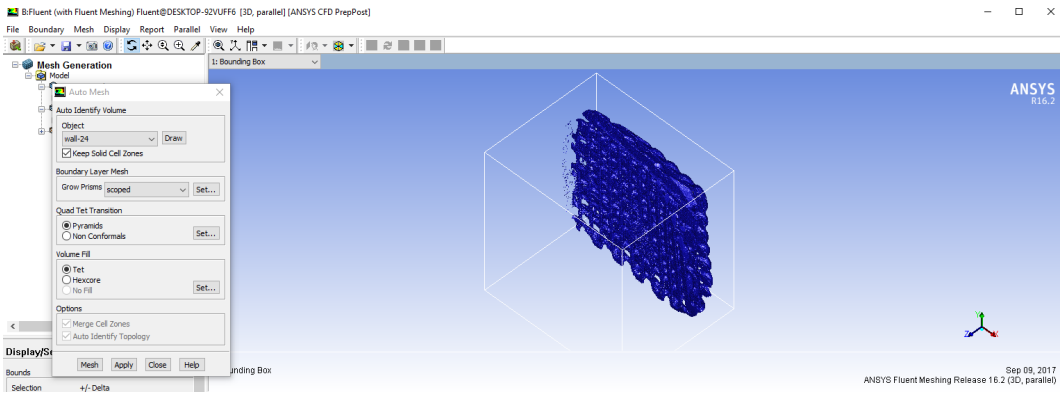

Figure A.5: Auto meshing tool in FLUENT. It is recommended to use pyramid meshing when possible to save computational time. The Set.. option may be used to indicate mesh size and fluid domain fill type.

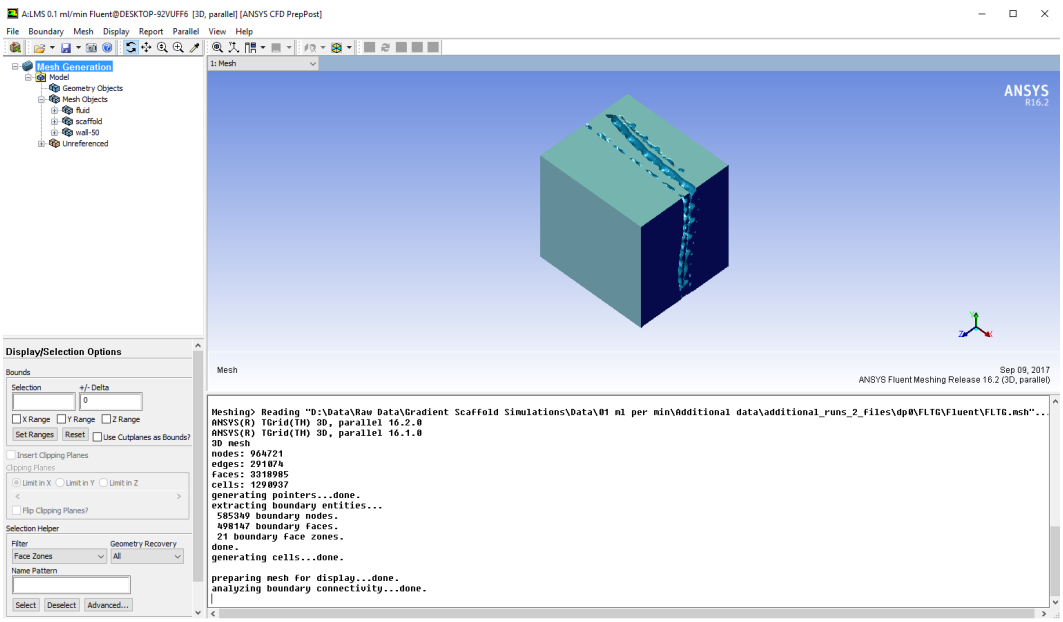

Figure A.6: Results from meshing in FLUENT. As shown in the screenshot, important information, such as number of mesh nodes, is given in the command prompt. Individual features may be highlighted in the left pane in order to examine the success of the mesh.

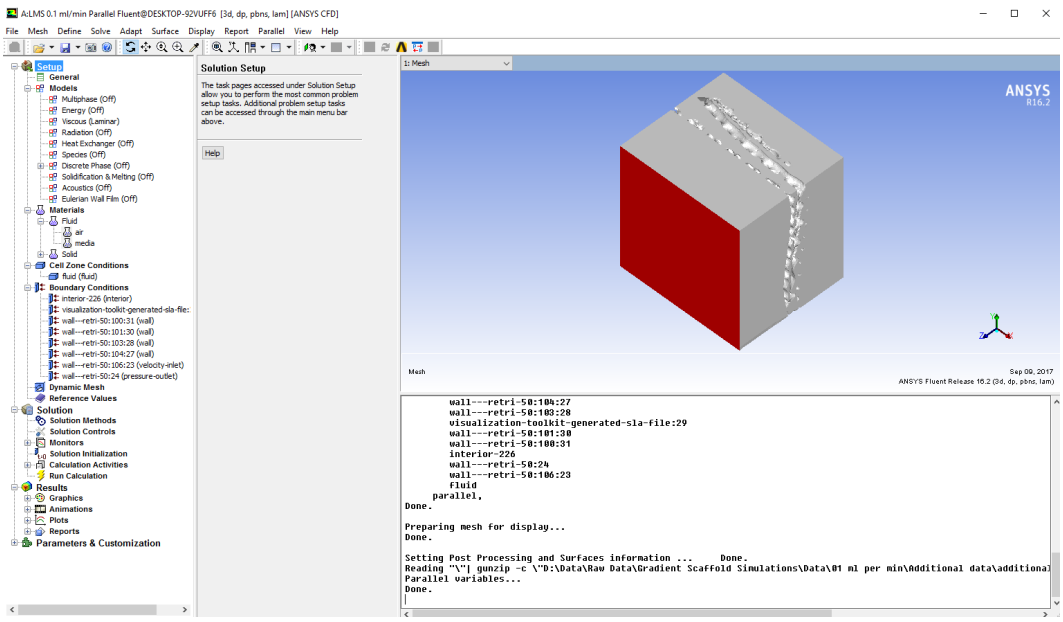

Figure A.7: The FLUENT computational Setup, Simulation, and Solution main screen. The left pane contains each of the individual settings that can be set. Available options for postprocessing are shown under the Results tab.

Simulation Setup and Post-Processing

Once meshing is complete, select the Setup module for the main page. Here, we will select the flow regime, fluid and scaffold characteristics, boundary conditions, simulation method, and computation settings (Figure A7). Settings and rationale for each of these may be found in Chapters 4 and 5. Once setup is complete, select to view normalized, unscaled residuals, set the hybrid initialization with preliminary values, and run the simulation.

Once convergence has been achieved, results may be either: (1) visualized using the Graphics tab in the Results section; or (2) exported for use in another program. In either case, make sure to select the desired variable AND the desired domain (bulk fluid, scaffold walls, or cassette walls).